Politecnico di Torino

Master's degree in:

Energy and Nuclear Engineering - Renewable Energy Systems

Graduation session: March 2023

Master Thesis

Experimental investigation of $La_{0.6}Sr_{0.4}Mn_{0.6}Cr_{0.4}O_3$ perovskite oxidation kinetics for thermochemical carbon dioxide splitting redox cycles

Supervisors:

Prof. Massimo Santarelli

Prof. Andrea Casalegno

Dr. Domenico Ferrero

Ing. Francesco Orsini

Candidate:

Giacomo Coslop

Abstract

An ever so intense effort aimed at a green transition to mitigate the effects of anthropic climate change is undergoing worldwide. The path is of course long and presents complex issues, one of them being the strong dependency on fossil fuels of various key sectors of the current society such as electricity and heat production, transport and industries. In this context, the production of renewable fuels, and more specifically solar fuels, is considered extremely promising by the scientific community. The most exploited way to obtain solar fuels as of now is to employ electrolysers to split H_2O and CO_2 molecules, reducing them to a mixture of H_2 and CO, which is called a syngas and can be used both as fuel and as platform for the synthesis of more complex hydrocarbons. Such process has strong efficiency limitations though and it is worth it to explore different options, amongst which a promising one is represented by thermochemical redox cycles.

In thermochemical cycles an oxygen carrier is reduced at high temperature, losing part of its oxygen content by generating some vacancies or rearranging its structure. The material then undergoes an oxidation step in which H_2O and/or CO_2 are supplied. In this step the oxygen carrier claims back the oxygen atoms that are missing in its lattice and therefore reduces the H_2O and CO_2 molecules to a syngas. The two described steps can then be repeated in a loop. The utilization of carbon dioxide as a valuable feedstock and the possibility to supply the high temperature heat through renewable technologies like solar concentrators make this process extremely interesting from the environmental point of view, while also presenting much higher potential efficiency with respect to electrolysis, since the transformation of solar energy in electrical energy is not required in this case. However, in order to make redox thermochemical cycles technologically and economically viable, suitable oxygen carriers as well as reactor layouts must be investigated.

This work studies an innovative perovskite with chemical composition $La_{0.6}Sr_{0.4}Mn_{0.6}Cr_{0.4}O_3$ in properly designed thermochemical cycles as oxygen carrier for carbon dioxide splitting. The tests are conducted in a machine for thermogravimetric analysis, in experimental conditions that have been optimized one by one. The perovskite's performances in terms of CO yield are assessed, with particular attention to the reaction kinetics of the oxidation step. Such an approach was chosen because there are not known kinetics studies on this specific material, which is relevant since knowing more about oxidation kinetics means to better understand the reaction mechanisms, as well as to be capable of more precisely tuning the features of a reactor in potential future developments.

Summary

1. Introduction 4
2. State of the art 11
2.1. Thermochemical cycles 11
2.2. Commonly used oxygen carriers 14
2.2.1. Ceria and doped ceria 14
2.2.2. Lanthanum manganese perovskites 16
2.3. Employed reactors 19
3. Experimental activity 24
3.1. Experimental setup 24
3.2. $La_{0.6}Sr_{0.4}Mn_{0.6}Cr_{0.4}O_3$ 26
3.3. Preliminary experiments 28
3.3.1. Experiment 0 29
3.3.2. CO_2 concentration range selection 31
3.3.3. Example of a definitive test 32
3.3.4. Potential carbonates formation 35
3.3.5. Temperature range selection 38
3.3.6. Sample mass and flow rate selection 41
3.4. Definitive experiments 44
4. Analysis of the oxidation kinetics 49
4.1. Theoretical framework 49
4.2. Kinetic study 52
4.2.1. Isoconversional method 53
4.2.2. Model fitting method 57
5. Conclusions 62

1. Introduction

Amongst the issues that involve the modern society on a world scale, the climate changes that are taking place as a result of the careless activities of the humankind should definitely be the major concern, especially for people working in the energy field. One of the most problematic effects in this context is global warming, which is in turn the driver of plenty of devastating effects, like extreme weather events, water scarcity, desertification, sea level rise and more. The main reason for this series of complex and worrying issues has been identified as the emission in the atmosphere of large amount of the so-called greenhouse gases (GHG), amongst which carbon dioxide is the most relevant one, for reasons that will be better detailed in the following. GHGs are capable of absorbing and emitting radiant energy, a crucial action in making the Earth the planet we all know. Without GHGs, in fact, the average surface temperature would be around -20°C, much lower than the one we experience today which is around 15°C. The correlation between the atmospheric GHG concentration and temperatures has been reported for many years already, one of the most clarifying examples being the study of the Anctartica's ice cores drilled in Vostok [1], which can be considered as a record of the atmospheric composition of thousands of years ago as shown in Fig.1. The diagrams show that a correlation is present, while they cannot conclusively state that high CO_2 concentration levels lead to temperature increase: the temperature signal appears in fact to lag with respect to the CO_2 signal. That being said, it is worthy to notice how the average CO_2 concentration in the atmosphere during the year 2021 has

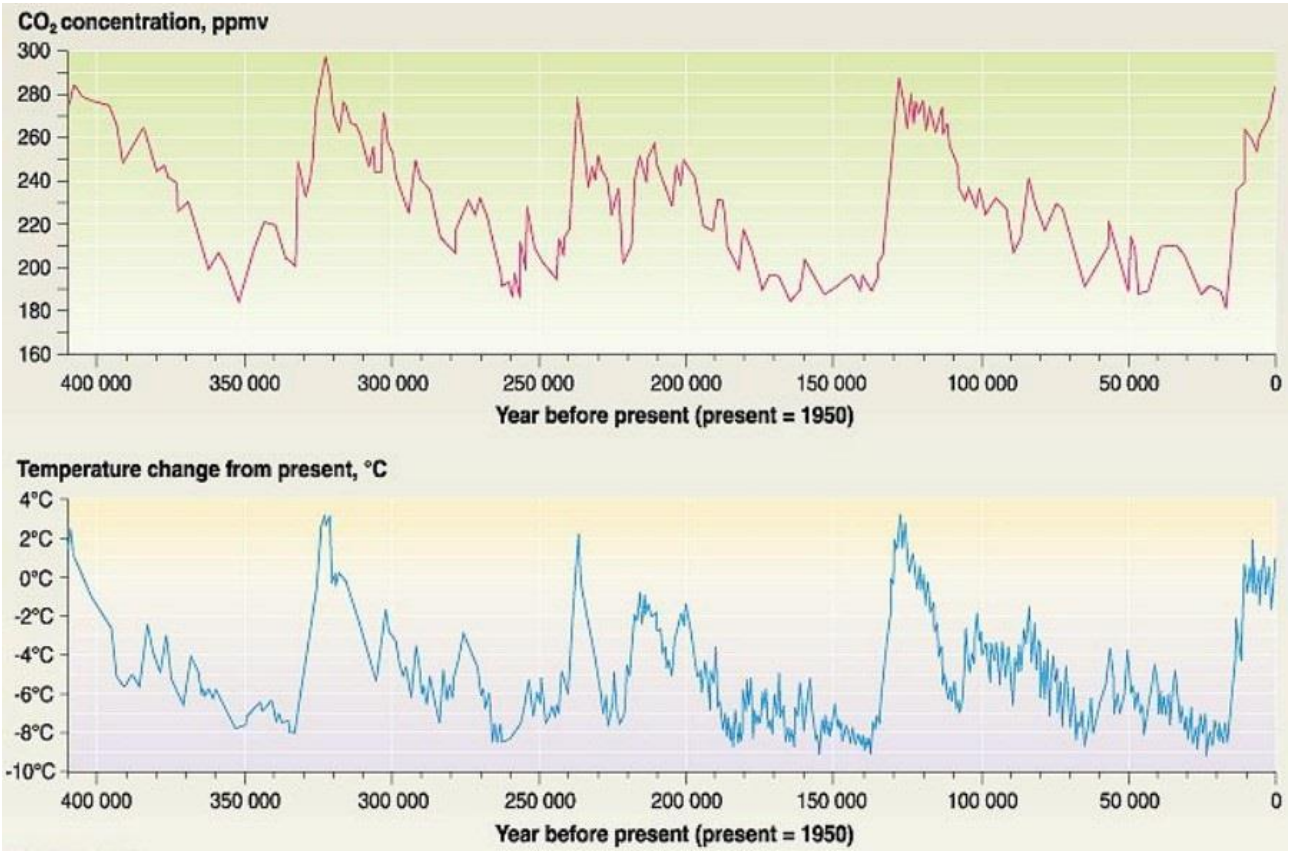

Fig.1 – Correlation between CO_2 emissions and average world temperature. [1]

been measured to be 414,7 ppm within an increasing trend [2], which is a completely out of scale value with respect to the ones reported in Fig.1. The GHGs emission increase as a consequence of human activities is a big concern, because it is not clear how badly the temperature trend will react to a similar CO_2 concentration increase. The current situation is critical and it is clear that proceeding with the current trend in terms of GHGs emissions is not a valid option.

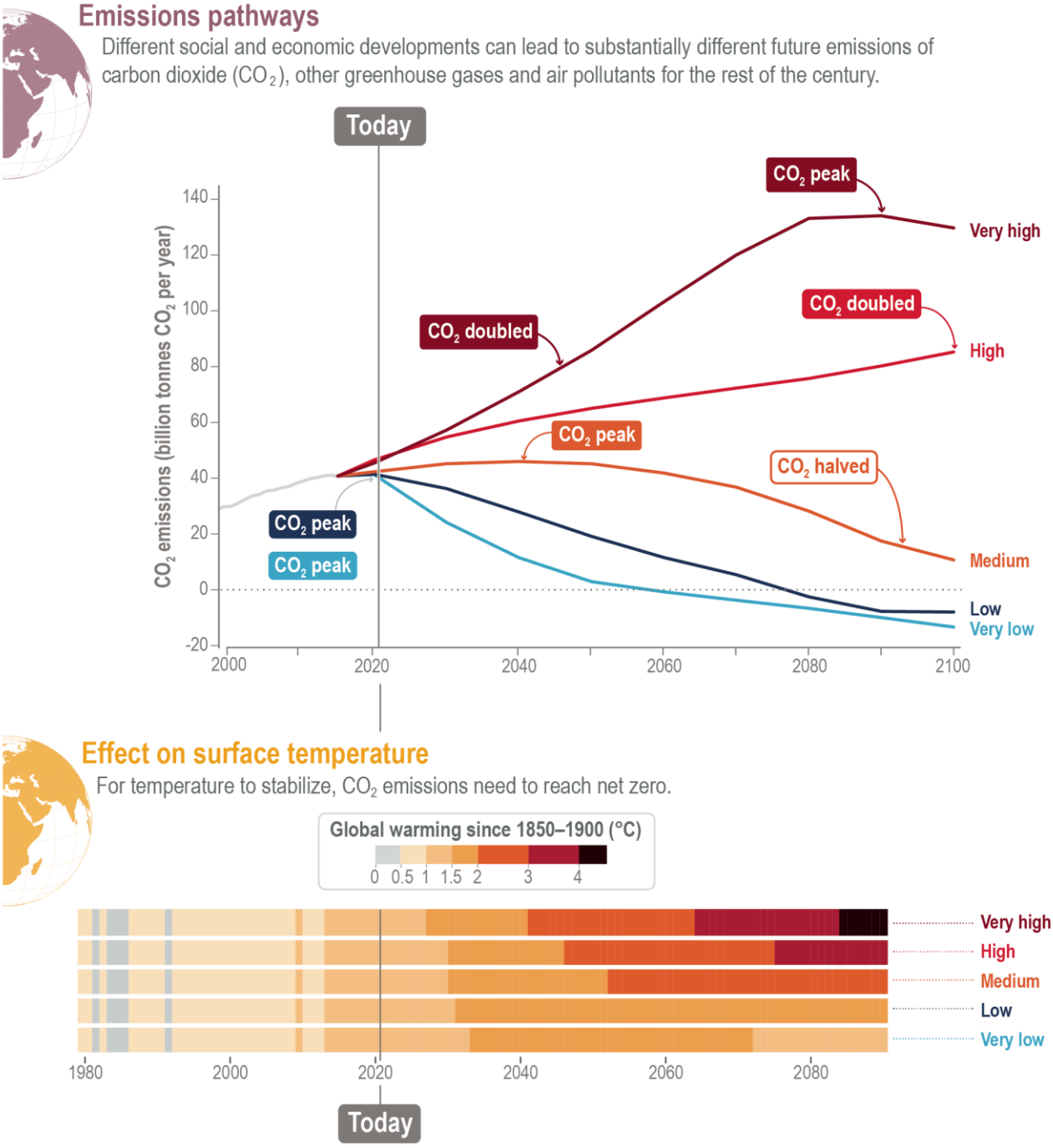

Fig.2 – Predicted future trends for CO_2 emissions and corresponding temperature increase. [3]

The latest conference of the Parties on climate change (COP27, held in 2022) has confirmed the willingness to keep the average temperature increase lower than 1,5°C with respect to pre-industrial levels (the reference here usually is the average temperature in the years 1850-1900,

since it is the earliest period with nearly global temperature observations). Such an ambitious goal seems to be quite unreasonable though, especially considering the current trends in terms of policies. In 2021-2022 the sixth edition of the IPCC (Intergovernmental Panel on Climate Change) assessment report has been released [3]. It contains multiple future scenarios concerning GHGs emissions, based on various foreseen "Shared Socioeconomic Pathways" (SSP) which are conceived to reflect different global policy orientations. It is relevant to notice how even the most optimistic scenario is not capable of complying with the 1,5°C threshold, exceeding it for some decades. Some of the most relevant indications given by the mentioned IPCC report are presented in Fig.2 and Fig.3.

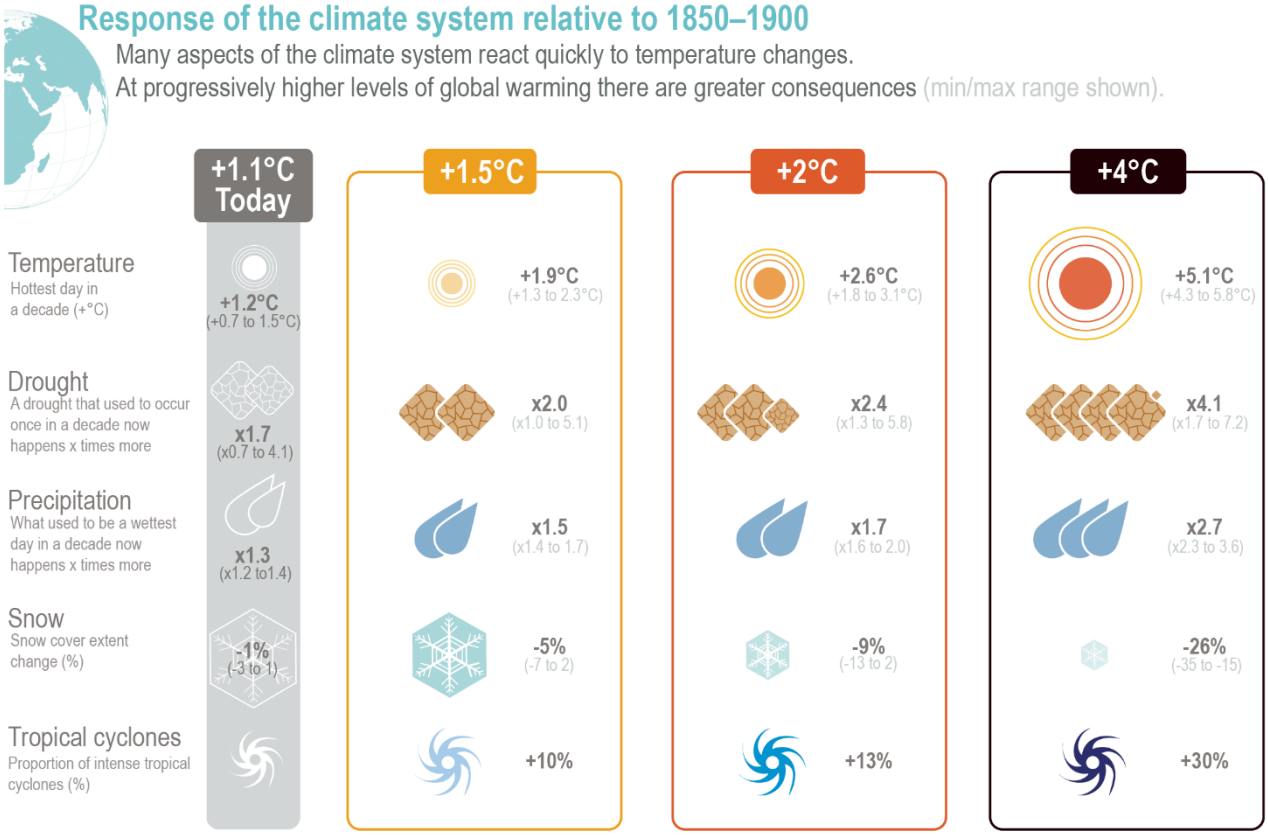

Fig.3 – Some of the foreseen environmental impacts depending on the future average temperature increase. [3]

On a more specific note, as already mentioned, amongst the various GHGs it is particularly relevant to focus on carbon dioxide (CO_2), even if this gas is not the one with the highest Global Warming Potential (GWP), which means that its capability of absorbing and re-emitting radiative energy is not as big as the one of other gases. The main issues when discussing CO_2 are firstly its relevant abundance in the atmosphere with respect to other GHGs (recent measurements provide values close to 420 ppm), as well as its persistency. Being a very stable molecule, in fact, makes it possible for CO_2 to survive in the atmosphere for centuries before reacting in some way. Because of that, carbon dioxide is predicted to be the most important contributor to the global warming in the upcoming years. In Fig.4 a comparison between the impacts of various GHGs emissions 10 years from now and 100 years from now is presented, and the persistency of CO_2 is particularly highlighted.

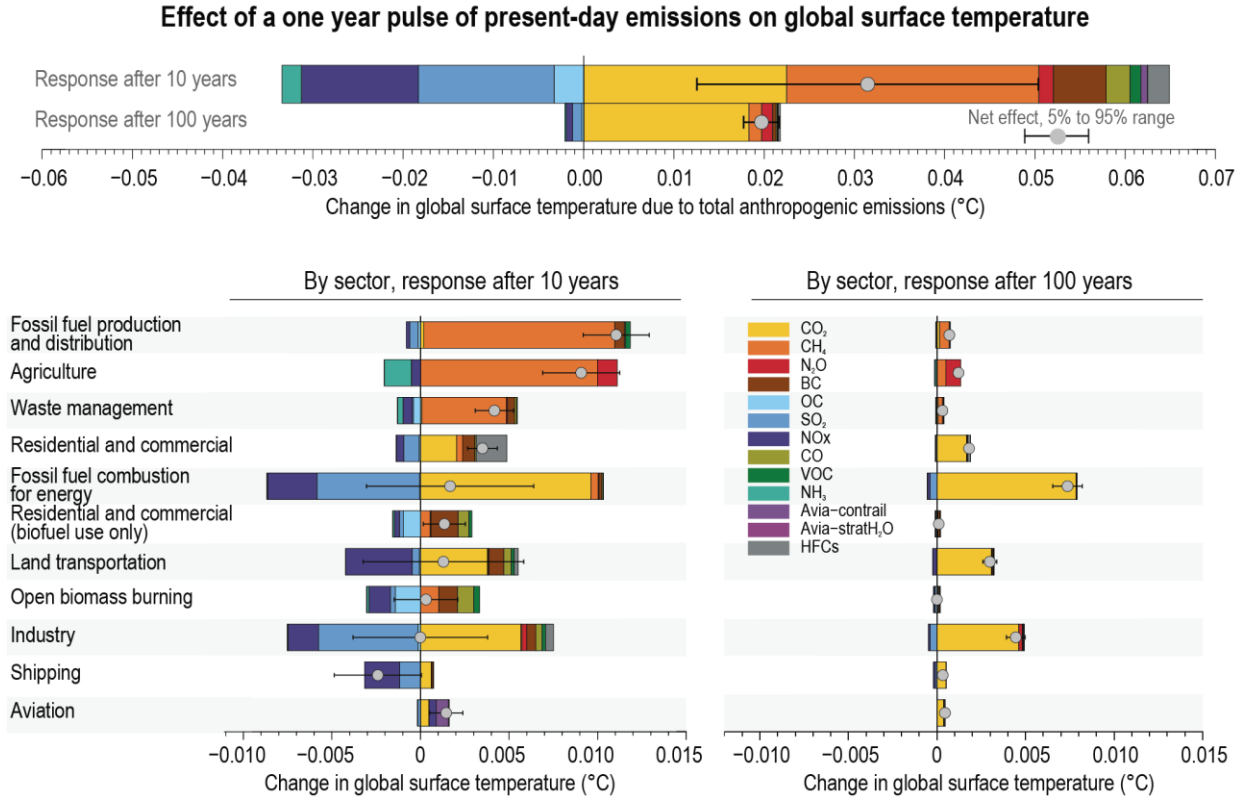

Fig.4 – Diagram highlighting the long-term persistency of CO_2 in the atmosphere. [3]

In such a framework, the idea of not only emitting less and less CO_2, but also trying to recover it from the atmosphere, has a lot of merit. This can be clearly observed in Fig.2, where for the two more virtuous scenarios the values of CO_2 emissions reach negative values in a mid to long term perspective. Such innovative approach goes under the general idea of Carbon Capture, Utilization and Storage (CCUS). For the moment the most common procedure in this field is to perform carbon capture on the flue gases of particularly emitting plants, e.g. fossil fuelled power plants or big industrial plants. Moving forward, with a more ambitious approach, different prototypes to collect CO_2 directly from the atmosphere are being tested nowadays. Most of the employed technologies rely on sorption-based cycles (both physical and chemical sorption is studied), but there are more creative concepts utilizing separation membranes or cryogenic processes too. [4] Most of the mentioned methodologies are still quite expensive though, therefore it is almost never economically advantageous for industries and plant owners to employ them. For this reason, specifically designed “carbon taxes” have been introduced lately, strongly incentivizing companies to choose CCUS solutions. As an example, the EU commission implemented a directive within this scope in 2003. [5]

CCUS technologies are extremely important especially if the global scenario is considered. A whole lot of sectors strongly rely on the combustion of fossil fuels, thus leading to climate change issues. Amongst the most relevant ones there are of course the energy sector (for the production of both electricity and heat), the transport sector and the industrial sector. Despite the existing efforts in changing the current status, demonstrated for example by the strict goals related to the

EU Green Deal (55% reduction in emissions by 2030, carbon neutrality of the EU by 2050 and more [6]), it is clear that such key aspects of our society will not radically change in a couple of years. The process will inevitably be slow and extremely complex, especially when considering the entire planet instead of the EU alone, so it will be necessary to deal with GHGs emission for a long time while the green transition is ongoing. There are anyway various options to reduce the usage of fossil resources (especially the most polluting ones, namely oil and coal) while still taking advantage of the many convenient characteristics of fuels.

One of them is represented by biofuels, which are a vast category of liquid or gaseous fuels (the most common ones are bioethanol, biodiesel, straight vegetable oil and biogas) produced with digestion or fermentation processes by specifically selected microorganisms. The idea behind this kind of fuels is that, even though their combustion leads to CO_2 emissions, the carbon cycle they are part of is sustainable. In other words, unlike fossil fuels which release in the atmosphere carbon that was segregated underground millions of years ago, biofuels are produced via selected crops (or sometimes from agriculture and forestry related waste, as well as the organic fraction of municipal waste) which produced oxygen by absorbing CO_2 during their lifetime. [7] Therefore, if the various steps of the crops' lifetime are properly controlled, the overall carbon balance can be close to zero, not to mention the fact that the combustion of biofuels can of course be coupled with CCUS solutions, reducing the greenhouse impact even more. In addition, employing large amounts of biofuels could strongly reduce the dependency from petroleum of countries without any access to conventional fossil reserves, which is of paramount importance. There are of course social issues related to this option, first of all the vast land spaces that intensive production of biofuels demands, and then the necessity to comply to the so-called cascade use of biomass: the crops' primary usage should in fact be for food, then for feeding animals, then as construction material and only as a last resource as feedstock for the energy sector.

Another interesting pathway to produce more sustainable fuels is to follow power-to-fuel protocols, obtaining e-fuels. Such an approach generally involves chemical reactions with hydrogen and carbon dioxide as reactants (sometimes carbon monoxide as well), like for instance the methanation reaction by hydrogenation, which can be carried out in two ways, depending on the compound that gets hydrogenated:

$$4\,H_2 + CO_2 \rightarrow CH_4 + 2\,H_2O$$

$$3\,H_2 + CO \rightarrow CH_4 + H_2O$$

Other fuels can be produced in such a way, for instance methanol, which can later on be transformed into dimethyl ether (DME, a fuel that can substitute Diesel with minor changes to a conventional motor's structure) with a de-hydration process, and then of course more complex Fischer-Tropsch procedures can be applied to convert a syngas of renewable origin in more complex fuels. [8] It goes without saying that similar processes are highly recommended especially if some CO_2 from CCUS technologies is available, and they can be considered sustainable only if the involved hydrogen (as well as the involved CO, when needed) comes from a green path.

Hydrogen in particular is an extremely versatile molecule that could also be utilized as a fuel by itself with great results in terms of GHGs emissions decrease, since its combustion only generates water steam. The main issue with this approach though involves the currently in use infrastructure: neither the natural gas pipelines nor the household's appliances are suitable to burn pure hydrogen at the moment, because of its different characteristics with respect to natural gas. Aside from that, most of the current hydrogen production relies indeed on fossil fuels, more specifically on the steam methane reforming process (SMR), a reaction that needs to be run at high temperatures:

$$CH_4 + H_2O \rightarrow 3\,H_2 + CO$$

This initial step is often followed by a water-gas shift reaction to get rid of the carbon monoxide while producing more useful hydrogen in the meantime:

$$CO + H_2O \rightarrow H_2 + CO_2$$

The final product of this process is often classified as "grey hydrogen", or "blue hydrogen" in case the procedure is coupled with CCUS technologies. Another less common but still employed process is to produce hydrogen from coal gasification, a very inefficient path which is however based on a cheaper feedstock, a major drawback being the fact that the supply chain of coal is highly polluting (this is the case of "brown hydrogen"). The only option when it comes to synthetizing sustainable fuels is to employ the so-called "green hydrogen", which is typically produced via electrolysis by only using electrical power from renewable sources. Here the simple reactions describing not just water electrolysis, rather co-electrolysis of water and carbon dioxide are presented:

$$H_2O \rightarrow H_2 + \frac{1}{2}\,O_2$$

$$CO_2 \rightarrow CO + \frac{1}{2}\,O_2$$

Notice that involving water and carbon dioxide as reactants leads to a final mixture that contains both hydrogen and carbon monoxide (a syngas) which can be used in some cases as a fuel, in others as a starting platform for the synthesis of more complex molecules, as already briefly discussed. Another aspect that must not be overlooked when producing these basic chemicals by electrolysis is the capability of storing solar energy in a form that is different to electricity. While storing electricity in batteries is expensive and impactful on the planet's resources, storing hydrogen and carbon monoxide can simply be achieved with suitable tanks and a compressor. Moreover, the stored chemicals can be readily retransformed to electrical energy whenever necessary by employing fuel cells, granting in this way some much needed flexibility to the electricity grid, which will be forced in the upcoming years to accept more and more energy peaks caused by the fluctuating production of photovoltaic (PV) plants and wind turbines.

There are more options that are under investigation at different levels, even if not commercially nor technically ready for large scale production of green hydrogen yet. A couple of them are photocatalytic processes involving photovoltaic effect [9], and thermochemical cycles (sometimes

also called chemical looping processes). In the following sections of this work, this latter opportunity will be explored, studying the performances of an innovative material as an oxygen carrier in properly designed thermochemical cycles. Here the oxidizing agent will be CO_2 instead of water, thus the obtained compound will be CO instead of hydrogen, but the overall approach remains the same.

2. State of the art

2.1. Thermochemical cycles

The green and sustainable production of simple chemicals like hydrogen, or even of syngas, is usually a process that requires plenty of electrical power to be carried out. The power producing step can be performed with several renewable sources, but in any case it is not particularly efficient since the very best wind turbines can reach maximum efficiencies around 50%, while for PV technologies the values remain much lower, around 20%. In this perspective it makes sense to explore different opportunities, like for instance utilizing thermally driven processes for the synthesis of the mentioned compounds. The reference here is of course not at heat delivered by combustion, since the focus still remains on sustainable options, rather to the high temperature heat that can be obtained with extremely high efficiencies by concentrated solar power plants (CSP). A thermochemical cycle is indeed a multi-step process which in many cases only requires heat and the involved reactants in order to carry out a series of chemical reactions. The most common situation in this field is to employ a two-step cycle based on a peculiar class of materials, capable of losing some of their own oxygen atoms at first and then recombining with them, which are therefore called oxygen carriers (OC). Potentially suitable materials are oxides of transition metals e.g. iron oxides, oxides of rare earths, perovskites and double perovskites. What is being described here can be summarized as a redox reaction, but with a huge advantage: subdividing it in two sub-reactions permits the independent optimization of the thermodynamic properties of the two steps, leading to much higher potential efficiencies.

In the two-step redox thermochemical cycle the first step is the reduction of the OC material. This is the endothermic step, where the high temperature heat is required, while the second step will be exothermic and the overall cycle can be both endothermic or exothermic when considered in its entirety. Here the generic chemical formulas are reported, for a generic metal oxide losing part of its oxygen:

$$MO_X \rightarrow MO_{x-\delta} + \frac{\delta}{2} O_2$$

The quantity δ is usually called “oxygen nonstoichiometry” and it represents the amount of oxygen that can be exchanged by the OC during the reduction phase leaving some vacancies in the material’s lattice. The following step is of course the oxidation, which is normally run at lower temperatures and involves some oxidizing molecules to be fed into the reaction chamber. The reduced OC strips such molecules (typically H_2O or CO_2) of some of their oxygen atoms in order to go back to its initial stable state, leaving as a result the chemicals that were the target of the overall process:

$$MO_{X-\delta} + \delta\, H_2O \rightarrow MO_X + \delta\, H_2$$

$$MO_{X-\delta} + \delta\, CO_2 \rightarrow MO_X + \delta\, CO$$

The cycle can then restart, since the OC has reached its initial composition again. In general, it can happen that the two steps are performed at very different temperatures, depending on the nature of the evolving reactions. This is positive for the efficiency of the single steps, but detrimental from the point of view of the entire cycle, since it means that a lot of time, as well as heating and/or cooling processes, have to be employed while switching from one condition to the other. In order to partially overcome this problem, a reducing agent can be added to the reduction step, so that it can be run at lower temperature. Using hydrogen here would in principle be a good idea, but it does not make much sense since it is the desired product, therefore methane is rather utilized. This combined process (Fig.5) not only allows to perform the cycle with a lower temperature swing, in addition the methane does also reduce, thus leading to the formation of CO and H_2 syngas in the reduction phase too. [10] Clearly, such an approach can be considered green and environmentally sustainable only if fossil feedstocks are not the starting point in the methane production, for instance biomethane represents a valid option.

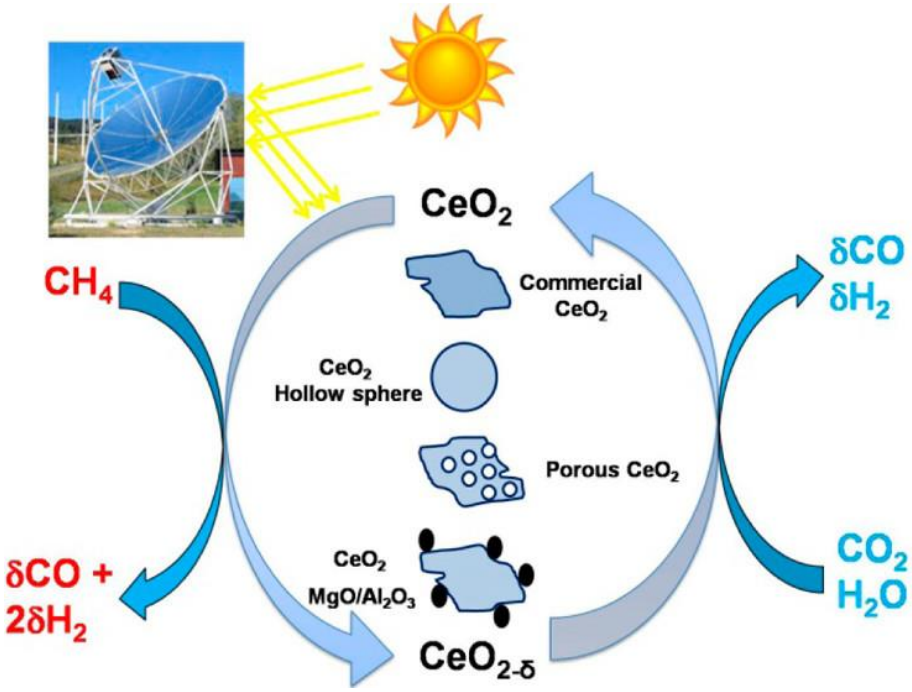

Fig.5 – Simplified description of simultaneous carbon dioxide and water splitting, with methane employed as a reducing agent. [10]

The employed materials are often referred to as oxygen carriers since their main role is exactly to lose and gain some oxygen cyclically. There are two main classifications which in turn are used to distinguish between three main categories of OCs:

- The OC can either be volatile or non-volatile. Volatile materials change their physical state during the reduction step, moving from solid to gases, e.g. zinc oxide (ZnO) which transforms into gaseous zinc. This means that during the process the vaporization heat is involved too, improving the entropic gain without increasing the temperature, but that is not much of an advantage since the required temperatures in these cases are typically very high already (even more than 2000°C). In addition, the phase change makes it difficult to design proper reactors, since it is much harder of course to keep a hot gas in place

with respect to a solid. Another issue with the phase change, especially when dealing with long run cycling, is represented by the solid to gas quenching phase, which if not conducted under extremely precise conditions might cause sintering and subsequent degradation of the material. [11] Non-volatile materials remain instead solid for the entirety of the thermochemical cycle and are generally preferred for their less complex operational aspects.

- The OC can also be stoichiometric or non-stoichiometric. Materials that react stoichiometrically undergo a full chemical reaction, changing their structure and chemical formula with the loss of some oxygen atoms. These usually require quite high temperatures, like for instance the already mentioned zinc oxide. On the other side, non-stoichiometric ones do not undergo such a drastic change in their chemical formula: they lose less oxygen and therefore only some oxygen vacancies are created, nevertheless their structure is still rearranged. The typical example of this category are all the possible perovskites. This implies that their overall yield of the produced chemical will be lower, since less oxygen will be exchanged, but on the other side the required temperatures for non-stoichiometric OCs are usually less challenging (even lower than 1000°C in some cases).

The basic features of two-step redox thermochemical cycles for the production of hydrogen or CO have been discussed, and in the following pages of this work when thermochemical cycles will be mentioned it will be to refer to this limited category of reactions. It is nevertheless important to be aware of the fact that the expression "thermochemical cycle" can in general be used for a multitude of different chemical processes. Remaining in the field of chemical looping, for instance, it is interesting to study elements like sulfur or iron which present many possible oxidation states that can be exploited to design cycles with more than two steps. As a notable example, the possibility to decarbonize a fuel (methane for instance, but more complex mixtures can be treated as well) obtaining hydrogen as clean fuel in the end has been studied. This idea takes advantage of three of the oxidation states of iron in a three reactors layout, but an even more thorough option exploiting four reactors has been conceived [12]. The simpler of the two processes

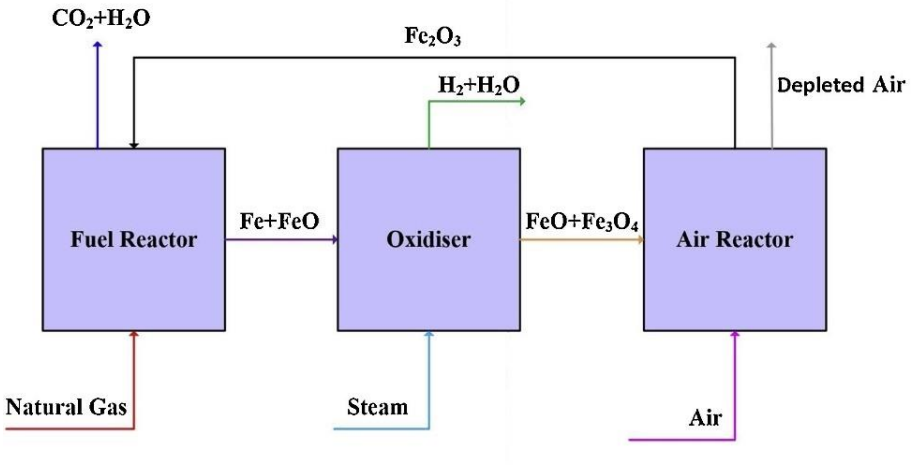

Fig.6 – Condensed schematics of a three-step chemical looping process involving iron oxides with the aim of decarbonizing a natural gas stream. [12]

is displayed in Fig.6 and begins with Fe_2O_3 as the starting OC. The iron oxide gets reduced inside the first reactor while the stream of carbonaceous fuel (in this case CH_4) is injected, resulting in solid FeO and in a stream of CO_2 and H_2O that could theoretically be sent to a properly coupled CCUS facility. The now reduced OC is then oxidized in the second reactor by means of a water stream, obtaining Fe_3O_4 and a stream of hydrogen, which represents the decarbonized fuel, i.e. the desired outcome of the entire process. In the final reactor a stream of air simply oxidizes the OC for a second time, making it return to its initial composition, while the depleted air (whose only difference from the beginning is a slightly lower oxygen content) can be discarded in the atmosphere.

2.2. Commonly used oxygen carriers

The idea of exploiting two step redox cycles for an alternative to electrolysis when it comes to water decomposition has been present for decades already: the first publications on the topic date back to the sixties, and back then already the main concern was found to be the identification of proper specifications for the compounds to be used [13]. Nowadays the research for the optimal OC material depending on the available operating conditions is still ongoing, with the design of innovative materials being investigated in depth, and even hypothetical materials being tested and assessed through proper modelling and computational tools [14]. For the moment, cerium oxides have emerged as the reference material in the past few years, while a second category of materials that have been extensively tested as OCs is represented by lanthanum manganese perovskites. A more in-depth analysis will be carried out on these two classes of materials, on the former because it is considered the state of the art in chemical looping processes and on the latter because the material that will be characterized later on in this work falls into the lanthanum manganese perovskites category. It is still relevant to mention the fact that OCs for thermochemical cycles applications are not limited to the mentioned materials, a vast literature is for example present discussing other typologies of perovskites, [15] which in some cases (while still at laboratory scale experiments) present extremely promising results in terms of productivity. [16] Other viable options, which were briefly recalled in the previous section, are volatile materials like the ZrO – Zr couple or the SnO_2 – SnO couple, or other nonvolatile metal oxides like ferrites. A multitude of studies have been carried out about them as well. [17]

2.2.1. Ceria and doped ceria

From a broad perspective, three are the most relevant aspects to be considered when choosing a material as oxygen carrier in a thermochemical cycle: thermodynamics, reaction kinetics and stability. [18] From the thermodynamic point of view it is important that the reduction reaction is favourable (being thermodynamically favourable can be summed up with $\Delta G° < 0$) at not too high temperatures, and vice versa that the oxidation reaction is favourable at not too low temperatures. Fast reaction kinetics and stable, predictable performances over a long number of

cycles, as well as resistance to sintering, are instead more practical features that a material should provide. Cerium oxides (and more specifically ceria, CeO_2) indeed satisfies most of these desirable characteristics, owning a fast oxidation kinetics, excellent thermochemical stability and a relatively low reduction temperature (as low as 1400°C). Some issues concerning the thermodynamic favourability of the reduction reaction are present, but they can be minimized as it will be clearer in a few paragraphs.

Concerning ceria and its properties, it is important to state that despite its capability to be cycled many times, the relatively low oxygen nonstoichiometry that can be reached implies some relevant problems from a productivity standpoint. In fact, despite having the best recorded solar-to-fuel conversion efficiency amongst all the studied materials at above 5% [19], undoped ceria still presents a limited fuel yield (if not at extremely high temperatures) as a consequence of suboptimal reduction extent. On a more positive note, its fluorite-like structure (Fig.7) is responsible of a high oxygen diffusion rate, with the vacancies that can be left empty or filled again with ease by oxygen atoms. Moreover, ceria's high melting temperature grants good structural resistance in many possible designs, from extremely simple powder samples to more complex porous structures. Also, the already existing vast literature on cerium oxide (which can also be exploited for more applications other than e-fuels production [20]) represents in itself a relevant advantage with respect to other OCs, since its behaviour and properties have already been extensively studied and therefore it can be used as replicable reference, for example in comparative studies.

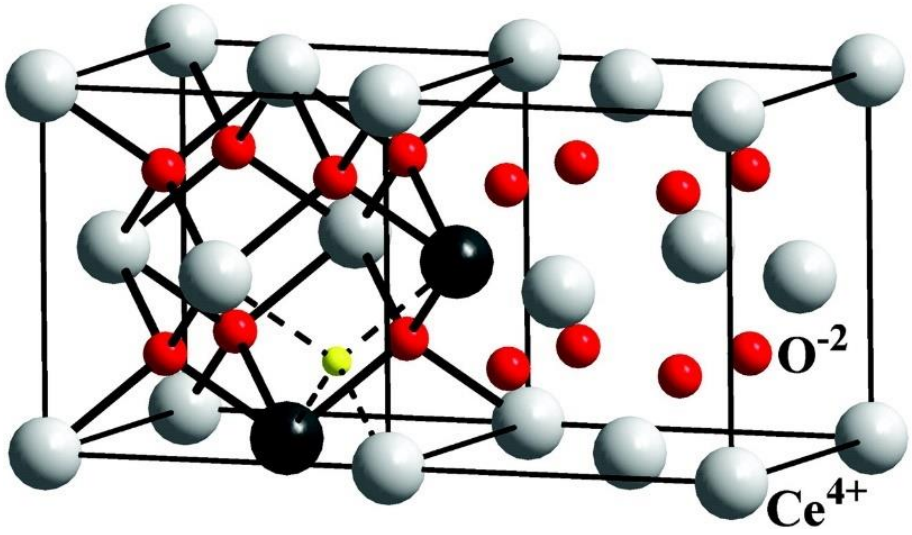

Fig.7 – On the right the crystalline structure of undoped ceria. On the left two trivalent ions (black) replacing two of the cerium atoms (white) and creating an oxygen vacancy (yellow). [21]

Undoped ceria's ability to perform both water splitting and CO_2 splitting under a variety of different conditions has been proven [11], but one of the main reasons for ceria's great success as an OC in thermochemical cycles dwells in its capability of being doped with some elements that are paramount in enhancing its properties. The most common one is zirconium doping, leading to a largely improved reduction extent while presenting worse performances in the oxidation phase, which is by the way perfectly acceptable, since the oxidation reaction already is extremely fast. The actually relevant drawback with zirconium doping is represented by the worsened

thermodynamic favorability, thus by the larger temperature swing between the two reaction steps, but on the other hand fast reduction leads to improved fuel yield [22]. The usage of dopants in ceria is especially interesting if the goal is to work at lower temperatures: going in this direction ceria doped with trivalent lanthanum, gadolinium, yttrium or samarium (Fig.7) has shown better reduction extents with respect to undoped ceria when the temperature is below 1400°C. [23] To give an idea of the variety of possible options, other elements that have been investigated as dopants for ceria are Li, Sr, Ca, Mg, Sc, Cr, Dy, Pr, Hf. Concluding, it is always complex to provide productivity yields for a single material, since different experiments are carried out under different conditions, that being said as a reference value measurements on zirconium doped ceria (specifically $Ce_{0.85}Zr_{0.15}O_2$) provided 144 μmol/g of carbon monoxide per cycle [24].

Of course, the presented considerations have been discussed referring to nonstoichiometric ceria. It is however peculiar to note how, when it was firstly studied as an OC for redox cycles in the context of hydrogen production, the considered reaction was stoichiometric [25]. The oxidation states Ce^{3+} and Ce^{4+} were in particular involved, as presented in the following formulas:

$$2\,CeO_2 \rightarrow Ce_2O_3 + \frac{1}{2}\,O_2$$

$$Ce_2O_3 + H_2O \rightarrow 2\,CeO_2 + H_2$$

The thermochemical cycle that involves the common state CeO_2 and the reduced state Ce_2O_3 though, is characterized by extremely demanding thermodynamic conditions, in particular the reduction temperature must be around 2000°C if not higher. This is not practical not only from the point of view of a continuously working reactor, but even from the point of view of the material itself, being the melting temperature of the reduced state not much higher, at 2200°C. In other words, stoichiometric ceria operation in thermochemical cycles risks to be a volatile redox cycle. For these reasons the non-stoichiometric option is by far the most common.

2.2.2. Lanthanum manganese perovskites

Different studies suggest that perovskites might prove to be performing and versatile materials for their application in thermochemical cycles, to such an extent that they might surpass ceria as the reference. In general a perovskite is a specific typology of oxide with formula ABO_3 (oxygen can rarely be replaced by other anions, but this will not be the case in the perovskites that will be relevant for this study) whereas A and B are two different cations, with the first one being larger in size. The ideal structure is cubic as it can be seen in Fig.8, even though the extensive potential for doping at both A and B site, as well as the impurities, makes it very rare for a perovskite to actually be characterized by a cubic structure. The presence of plenty of doping opportunities [26], indeed, is ultimately the main reason for which perovskites are definitely interesting for the studied two step redox thermochemical cycles. Due to this peculiarity, in fact, their thermodynamic properties can be quite easily tuned in order to comply with the needs of the reactions that have to be run case by case.

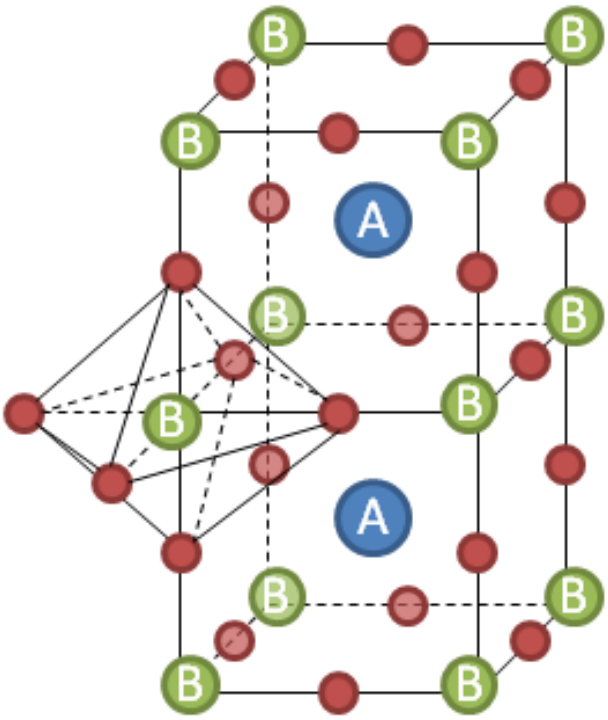

Fig.8 – Ideal cubic structure of a perovskite, the larger A cation is 12-fold coordinated with oxygen, B cation is 6-fold coordinated with oxygen. [17]

Some general indications about perovskites can be provided, for example they display better oxygen nonstoichiometry, thus higher productivity with respect to ceria, while holding the capability of being cycled at much lower temperatures. On the other side, oxygen diffusivity, structural stability and oxidation kinetics are instead worse, but can be improved with some targeted doping. Discussing the performances of different typologies of perovskites is however not trivial: there are so many of them (not only plenty of elements are employed for doping, but doping itself can have different extents, in turn leading to structurally different perovskites) and the results that can be found in literature often provided for a plethora of experimental conditions. In many studies on multiple perovskites though, the prominent spot is taken by lanthanum manganese perovskites. [27] Their general formula, including some potential A-site as well as B-site doping is the following (where clearly it has to be verified that $0 \leq X,Y < 1$):

$$La_{1-X}A_XMn_{1-Y}B_YO_3$$

Simple $LaMnO_3$ is characterized by a particularly low reduction extent (it reaches low values of oxygen nonstoichiometry when reduced), and given how easy it is to tackle this issue with proper doping there are very few studies that focus on the undoped material. [28] Including strontium as a dopant in the A site provides exactly the needed results: strontium has a lower charge with respect to lanthanum (Sr^{2+} vs La^{3+}), therefore it leads to an increased oxidation state of magnesium, part of which shifts from Mn^{3+} to Mn^{4+}, and in turn this overall structure modification increases the presence of oxygen vacancies, making it possible for the perovskite to reach higher values of oxygen nonstoichiometry. A similar effect is obtained by doping the A-site with calcium (Ca^{2+}). Such doping action presents a drawback though: the reaction rate of the oxidation step is

greatly reduced, while the production rate of the reduction reaction is also negatively impacted. This detrimental effect on the material's kinetics though is outweighed by the improved reduction extent, in other words, the reactions are slower, but the obtained nonstoichiometry is largely improved, therefore the overall fuel productivity increases [29]. Another divalent dopant that has been investigated in this sense is barium, but the results have not been this positive, proving the fact that a thorough doping design is necessary in order to obtain the desired improvements, it's not that every divalent cation can be employed regardless. In addition to the presented ones, A-site doping was attempted with yttrium, neodymium, samarium, gadolinium and dysprosium, but the most relevant results have been achieved with the mentioned strontium and calcium doping. For this reason, again as reference value as it was done in the subchapter that dealt with ceria, some productivity yields are presented in Fig.9 for these two classes of lanthanum manganese perovskites.

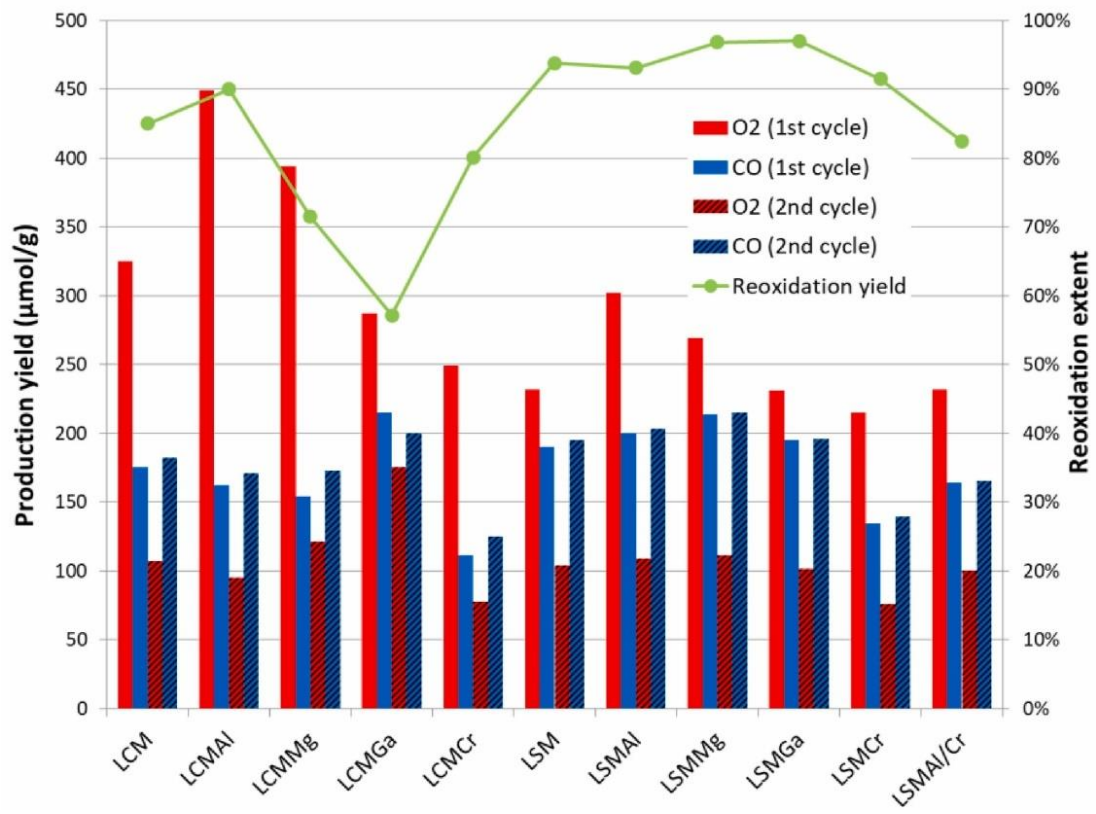

Fig.9 – Experimental yields for CO_2 splitting. [24]

Moving on to B-site doping, the most common idea is to employ aluminum in order to improve the poor reoxidation performances that are typical of most perovskites, with a slightly beneficial effect on the reduction phase too. In addition, aluminum is smaller in terms of size with respect to manganese, thus the overall stability of the perovskite's structure is improved by this doping approach. The reoxidation phase is indeed largely improved by the utilization of aluminum, which translates into better productivity for both the oxidation and the reduction step in the long run [30], as it can be easily confirmed by looking at Fig.9. The contribution of aluminum is even more impressive considering that this dopant agent is redox-inert, so the overall redox capability of the perovskite must be lower after doping (manganese ions are instead redox active). Gallium

and scandium have also been considered as B-site doping with the same purposes, and indeed the resulting performances are in some cases even better with respect to the aluminum doping, but some difficulties and limitations are introduced by their low solubility. Their extremely promising results in terms of fuel productivity though could incentivize further research on these two dopant options. [31] A whole other story is the B-site doping with magnesium: in this case the reaction's performances remain basically unvaried, but the addition of this element leads to improved stability (similarly to aluminum, due to its relatively small size, but also to the strong bonds that are generated with oxygen atoms, e.g. magnesium oxides present extremely high melting temperatures, around 2800°C) and more importantly increased sintering resistance, making magnesium-doped perovskites suitable candidates for long run thermochemical cycles. More options as dopants in the B site are iron, nickel, cobalt and chromium: the latter in particular will be more deeply characterized in subsection 3.2. when discussing the actual perovskite that has been studied experimentally.

2.3. Employed reactors

The development of suitable reactors to efficiently perform thermochemical cycles is equally important to the utilization of the proper materials as OCs. It is difficult to present a comprehensive perspective on this matter, generally speaking one common feature of every possible thermodynamical cycle is the necessity for high temperature heat in order to drive the reduction reaction. If the goal, as it should be, is to provide such heat through sustainable and green sources, the natural choice is to rely on CSP technologies. The field of concentrated solar power is vast and diversified, and it is not relevant in this context to deeply explore it, in case more information on the topic is needed there are plenty of sources in the literature. [32] In order to provide some hints, it can be useful to state that CSP is basically about collecting the solar radiation that reaches the ground and concentrating it on a very small area (the receiver) with properly shaped mirrors. Two approaches are possible: one single curved mirror like in dish and parabolic trough layouts, or multiple flat mirrors, properly oriented towards the focus point, like in linear Fresnel and solar tower layouts. As already mentioned, the direct conversion from radiative solar energy to heat by concentration is a way more efficient methodology than to go through the conversion to electrical energy, performing electrolysis and splitting H_2O or CO_2 that way. This does not mean that 100% of the solar energy is transmitted to the OC material though, there are of course some losses which can be caused by different events. Some of them are the reflectivity of the mirrors, shading, the presence of dirt on the surfaces, the wind moving the mirrors, errors in the tracking system that aligns the mirrors towards the Sun, the presence of a glass layer between the mirror and the OC, maintenance requirements and so on. [33]

That being said, whatever the CSP layout might be, the most relevant subject when dealing with the study of potential reactors is the design of the receiver, and more in general of the reaction chamber. Before starting with the description of some available options in terms of reactors, it is important to be aware of the fact that achieving a global description of the topic is not realistic due to the extreme variety of implemented solutions and required operating conditions. As an

example, even an almost irrelevant aspect as the methodology for the undesired oxygen removal during the reduction reaction can be performed in at least four different ways [34]. Trying to proceed with order in such a complex topic, it is possible to subdivide the reactors in two macrocategories: reactors with a single reaction chamber in which both reduction and oxidation take place, leading to the necessity of cooling down the chamber while the oxidation step is progressing, and decoupled reactors where the different steps of the cycle occur in different places. It will not be further detailed in the following, but a third option is promising as well: employing a heat transfer fluid (liquid metals, nanofluids or molten salts are the potentially suitable options) to carry the heat from the receiver to the actual reactor. In this way the area of the receiver can be fully decoupled from the area of the OC material, therefore allowing for better overall optimization of the involved heat fluxes [35].

Starting with the mono-chamber approach, the most straightforward idea is to employ a monolithic reactor, consisting of a solid structure that can be either made of the OC material, or of some resistant ceramic coated with a thin film of the OC material. Such structures need of course to be porous, in order to increase the surface reaction between the solid itself and the gaseous stream of oxidizing agent (H_2O or CO_2). The state of the art structure for this kind of applications is represented by monolithic blocks with dual-scale porosity (Fig.10), i.e. materials that present pores with characteristic dimensions of two well separated orders of magnitude. Such a complex geometry has a double advantage: the “macroporosity” allows the concentrated sunrays to penetrate deeply into the material (a property that is sometimes referred to as low optical thickness), heating it up in a more homogeneous way with respect to a material which is only enlightened on its outer surface, while the “microporosity” guarantees the desired large specific surface area, so that the interface where solid and gas are in contact is improved. An example of monolithic reactor can be seen in Fig.11, the operation in this case is quite simple: the cerium oxide is thermally activated by the incoming solar radiation, once suitable temperatures are reached the reduction reaction takes place in a pure Argon atmosphere, and in the following step a shutter is closed while feeding a controlled CO_2 flow rate, so that the oxidation step can be eventually performed [36]. Such procedure can then be repeated several times.

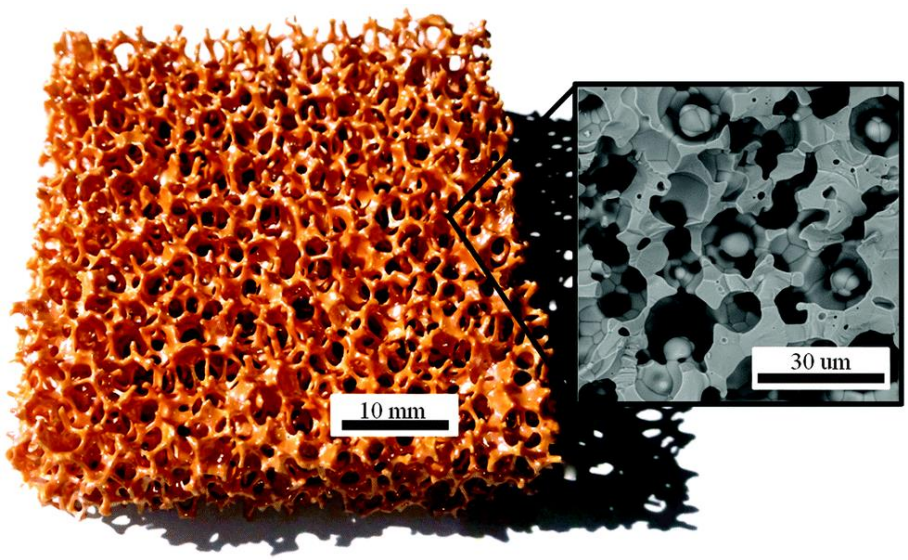

Fig.10 – Monolithic dual-porosity ceria receiver. [37]

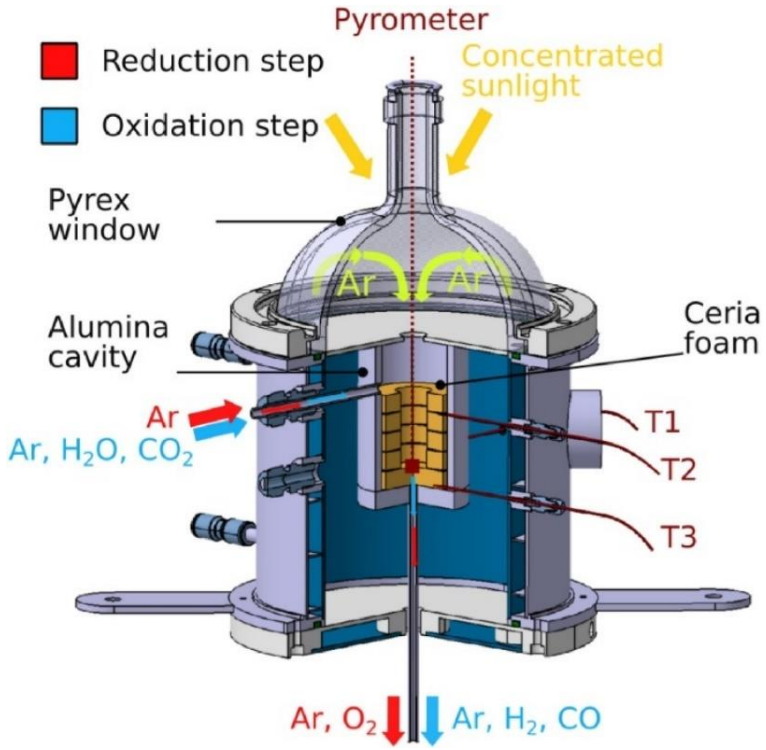

Fig. 11 – Single chamber, monolithic cavity-type reactor for the application in thermochemical cycles. [36]

A further option for single-chamber reactors is to take advantage of a pulverized OC, with its particles embedded in some fluid carrier by developing circulating fluidized bed reactors. In such layouts the gas flow must be directed in a way so that it can be a driver of the particle's motion, because typically the solar radiation is delivered through the upper part of the reactor, so convective motions are not originated (particles are required to move from the top part of the fluidized bed to the bottom and vice versa for temperature homogenization reasons). Once the needed temperature is reached and the reduction reaction is over the solar radiation is stopped for a while and the oxidation reaction can take place, while the inert gas flow is switched to the desired mixture of inert and oxidizing agent. Such concept has been investigated for a mixture of nickel-iron oxide and zirconia (respectively $NiFe_2O_4$ and ZrO) as OC particles [38]. In this specific case the reaction chamber has been designed with a central tube and an external annulus. The inert nitrogen gas makes the particle-carrying fluid to rise along the central portion of the reactor, which in turn drives a descending direction of the fluid flow in the annulus section.

Utilizing separated chambers for the reduction and oxidation reaction, instead, allows to better optimize each of the two steps, but on the other end usually is related to higher construction costs. In addition, another interesting advantage of this second macrocategory of reactors is the fact that heating and cooling the chamber during the two steps is not necessary anymore, therefore continuous operation can be achieved. The possibilities to get creative with reactors layout while employing more than one chamber are plenty. One already considered opportunity is the one of the continuous packed bed of particles, in which the OC is present in form of particles that are transported from one chamber to the other in order to carry out the desired thermodynamic cycle. In Fig.12 an interesting concept that falls into this category can be seen, where the two chambers are clearly separated. In the picture the entering as well as the exiting gaseous streams are well highlighted.

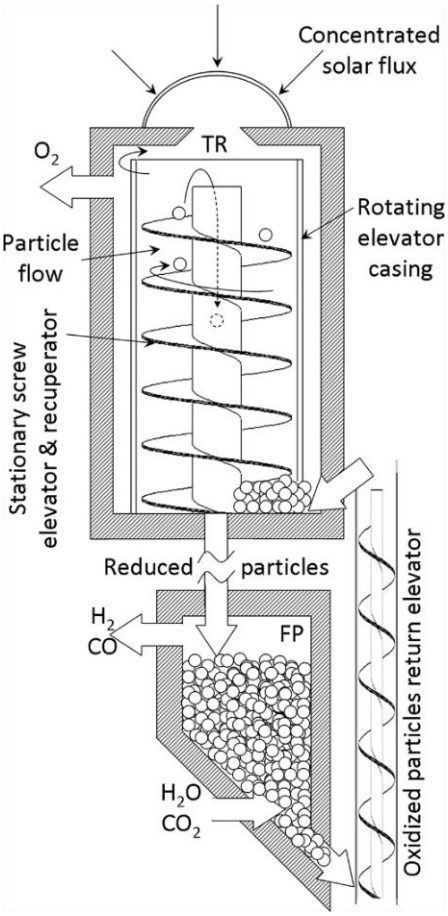

Fig.12 – Concept of moving particle bed reactor. TR stays for thermal reduction chamber while FP stays for fuel production chamber. [39]

Another potentiality of the multi-chamber approach lays in the fact that in this case, differently from the single-chamber reactors, it is much easier to employ volatile materials as OC since with a dedicated layout they can now be confined in a chamber where only one reaction is occurring and there is no risk of mixing with other compounds. A peculiar prototype in this sense has been conceived with the reduction chamber in the shape of an inverted cone, whose tilted walls are traveled by zinc oxide (ZnO) particles, while the walls themselves get heated by the concentrated solar radiation [40]. The reduction reaction occurs at this stage, with the resulting gaseous zinc (together with the released oxygen) that is entrained in a vortex flow which is artificially generated and subsequently exits this first chamber through a hole located in the cone vertex. The gaseous reduced OC can then be sent towards a second chamber in which the oxidation reaction takes place, while the residual solid zinc oxide is collected in an annular region at the bottom of the inverted cone.

Monolithic reactors are possible in this case too, for instance a rotatory cylindrical reactor has been proposed and tested with ceria and Ni,Mn-ferrite ($Ni_{0.5}Mn_{0.5}Fe_2O_4$) [41]. The idea is basically about coating the external surface of a cylinder with the reacting material and then rotating it with its axis oriented horizontally. In this way, with a proper design, the upper portion of the reactor is always hit by the heat flux delivered by a beam-down concentrating system driving the reduction reaction, while the bottom half (which does not receive any concentrated radiation) drives the oxidation reaction instead. The two halves of the cylinder do not share the same

atmosphere, rather they are sealed, so that two reaction chambers are effectively created. The constant rotatory movement then moves the reduced portion of the OC towards the dark side and the oxidated portion towards the enlightened side.

Even if it is true that the design of the most suitable thermochemical reactor for a specific application can in principle be entirely carried out from the theoretical point of view with tools like solar flux simulators and computational fluid dynamics, it is of course extremely relevant to practically demonstrate the feasibility of the investigated concepts. [42] In this section various layouts have been proposed, but very few of them have been tested to more than a lab prototype scale. The example of a 100 kW scale pilot plant for hydrogen production that was built on a full size solar tower facility in Spain during the year 2008 is therefore remarkable [43]. The employed receiver was made of several monolithic absorbers with a honeycomb structure made of highly resistant silicon carbide which was coated with iron-zinc mixed oxides. The reactor was of the mono-chamber typology, but there were two of them, so that the heliostats were alternatively pointed towards one or the other one, and while in one chamber the reduction reaction was occurring, in the other one the oxidation reaction was being performed. A water steam mass flow of about 3,5 kg/h in inert nitrogen was provided to the reactor while cycling between 800°C and 1200°C, and the pilot showed a productivity of 500 g of hydrogen in a single day, with potential to improve, proving the technical feasibility of similar solutions on a large scale.

Another interesting result, even though at a smaller scale, is the practical demonstration concerning the technical feasibility of jet fuel production via thermochemical cycles, in other words, the production of “solar kerosene” [44]. In a reactor similar to the one in Fig.11 containing ceria under the form of a monolithic reticulated porous ceramic, around 300 consecutive cycles were performed between 1450°C-1600°C for the reduction step and 700°C-1200°C for the oxidation step. The involved reaction was co-splitting of H_2O and CO_2, with the resulting product being a syngas composed by 33,7% hydrogen, 30,5% carbon dioxide and 19,2% carbon monoxide, aside from some other molecules. Such carbon rich gas was then compressed and transformed into a mixture of naphtha, gasoil and kerosene via Fischer-Tropsch processing. Despite the very little amount produced (the input solar power was below 5 kW, with an overall solar-to-fuel efficiency of 1,72%) and the economic viability of the process being still far, the predicted potential efficiencies for this process largely outperform the alternative path involving PV and electrolysis. In addition, the life cycle assessment of solar kerosene presents significant improvements, at least in terms of GWP, when compared for example to the production of biofuels.

3. Experimental activity

3.1. Experimental setup

The test bench that was utilized for the collection of the experimental data that will be presented in the following sections was part of the CO_2 Circle Lab facilities which are placed within the Environment Park, a technology park located in the city of Turin. It basically consisted of a thermogravimetric analyzer (TGA), connected to some laboratory lines feeding the most commonly used gases (like for instance air or CO_2), together with some 150 liters cylinders containing more specific gases, like the argon which was employed as inert sweeping gas throughout most of the experiments. The test bench equipment was completed by the tubes necessary to connect the TGA with the supply lines, an extractor fan towering above the entire structure, just in case some dangerous leakages could take place and a computer where to record and save the data measured by the TGA itself.

The specific TGA machine is the "NETZSCH STA 2500 Regulus", consisting of a vertical pipe in which a very accurate two-arms thermobalance which structure is displayed in Fig.13 is contained. Each of the two arms ends in a small plate where two S-type thermocouples constantly measure the sample's temperature. On one side an empty crucible must be placed for reference,

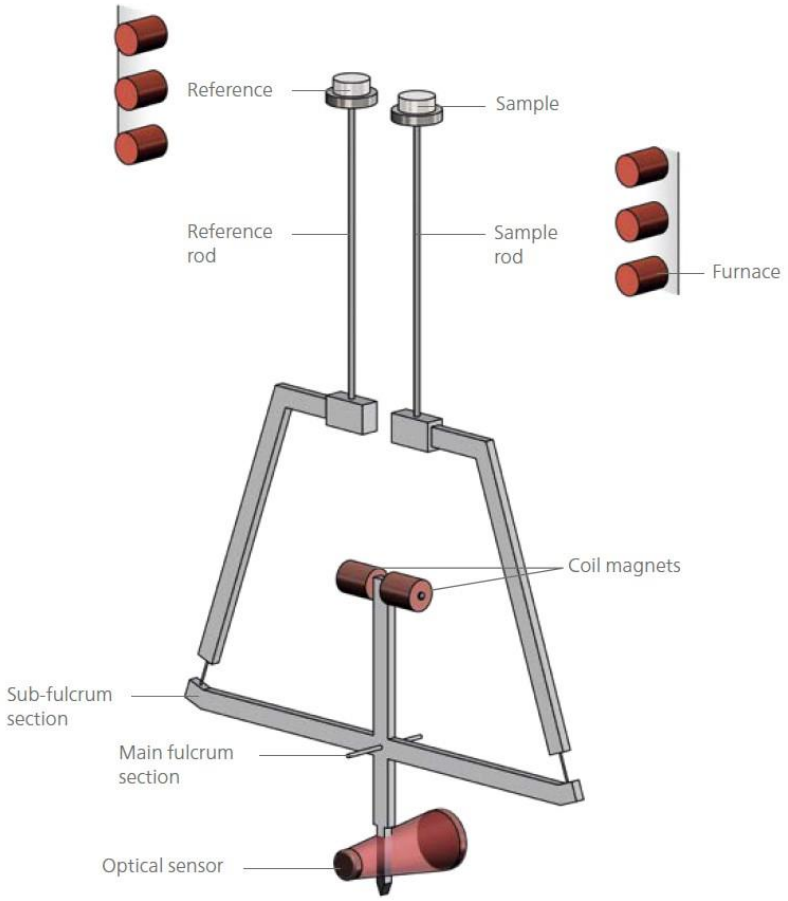

Fig.13 – Basic schematics of the internal measuring mechanism belonging to the TGA machine that was used for the experimental activity. [45]

while on the other side the crucible containing the sample can be positioned. Notice that only the rods with their plates are accessible to the operator, who is easily capable of removing and positioning the crucibles by carefully operating with a tweezer. The microbalance is equipped with a compensating system based on coil magnets which is designed to compensate undesired buoyancy and convection effects, therefore avoiding the necessity of performing blank tests of the experiments. Also, its working principle is based on the oscillations detected by the optical sensor that is located at the bottom.

Within the reaction chamber a controlled volumetric flow rate flows from the bottom towards the top portion of the machine, from where it. The possible atmospheres that can be sent through the machine are various, from inert gases to oxidizing agents (like of course CO_2, which will be used in the experiments) to vacuum conditions. At this level the TGA can be coupled with other pieces of equipment, for instance the evolved flue gases could be sent to a mass spectrometer for the precise evaluation of the various chemical species that are present in the exiting flow, before being collected by the extractor fan located above the test bench. Aside from the flow rate, the other parameter that can be controlled with extreme accuracy is the temperature inside the reacting chamber. Temperature ramps as well as isothermal runs can interchangeably be performed by the TGA, and the homogeneity of the conditions internally to the vertical pipe is guaranteed by properly positioned furnaces. The most relevant features of the TGA are thereby presented in Tab.1:

Technical specification	**Related value [45]**
Maximum temperature [°C]	1600
Available heating rates [°C/min]	0,001 ~ 100
Temperature precision (repeatability) [°C]	0,3
Maximum weight load [mg]	1000
Maximum weighing range during one run [mg]	± 250
Thermogravimetric resolution [µg]	0,03
Maximum degree of vacuum [Pa]	10^{-2}

Tab.1 – Key features of the NETZSCH STA 2500 Regulus.

The “NETZSCH STA 2500 Regulus” comes with a dedicated software, called “Proteus”. One of the most important features of this system consists in the simultaneous collection and analysis of two relevant signals, in particular mass changes and caloric effects. Calorimetry was not relevant for this specific work though, in fact the only data that were retrieved from each experiment were the mass percentage variation with respect to the initial value (the parameter on which the whole upcoming analysis is based), the temperature of the sample in the crucible and the volumetric flow rates of the inlet gases composing the atmosphere inside the reaction chamber. The data, which were provided by the Proteus software and then saved in Excel sheets, were taken

with one second time intervals throughout the entirety of each test. The results of the performed experiments will be presented and discussed in the following subsections, after some specific description of the utilized perovskite.

3.2. $La_{0.6}Sr_{0.4}Mn_{0.6}Cr_{0.4}O_3$

The material that will be employed in the experimental activity is a lanthanum manganese perovskite doped with strontium in the A sites and with chromium in the B sites. The specific sample that was employed in the measurement was conveniently under the form of a black fine powder, so that some of it could be put with ease inside the TGA crucibles, which were small cylinders with 5,2 mm base and 2,6 mm height. The $La_{0.6}Sr_{0.4}Mn_{0.6}Cr_{0.4}O_3$ perovskite (LSMCr from now on) was characterized via X-ray diffraction (XRD) spectroscopy and the results are shown in Appendix A. It is relevant to notice the fact that the obtained XRD patterns are in good accordance with the ones provided by studies on similar materials, that is, still strontium-chromium doped lanthanum manganite, but doped to different extents [46]. It can therefore be safely stated that the microstructure of the employed material is the same that has been found in those works, particularly a rhombohedral structure of the R–3c space, meaning that the ideal cubic structure is distorted as shown in Fig.14. In general terms, chromium substitution in the B-site of perovskites is a topic that has already been touched in this work, for instance in Fig.9 it is possible to see a comparison between the performances of diversely doped materials, but in literature chromium does often not stand out as a particularly interesting option when compared to other B-site dopants. [47] What has been instead more often proven is the fact that Cr doping is beneficial from the point of view of the material's stability, improving long term cyclability as well as the behaviour at high temperatures [48], because it is in general quite difficult to make the oxidation state of chromium vary during oxidation and (especially) reduction reactions.

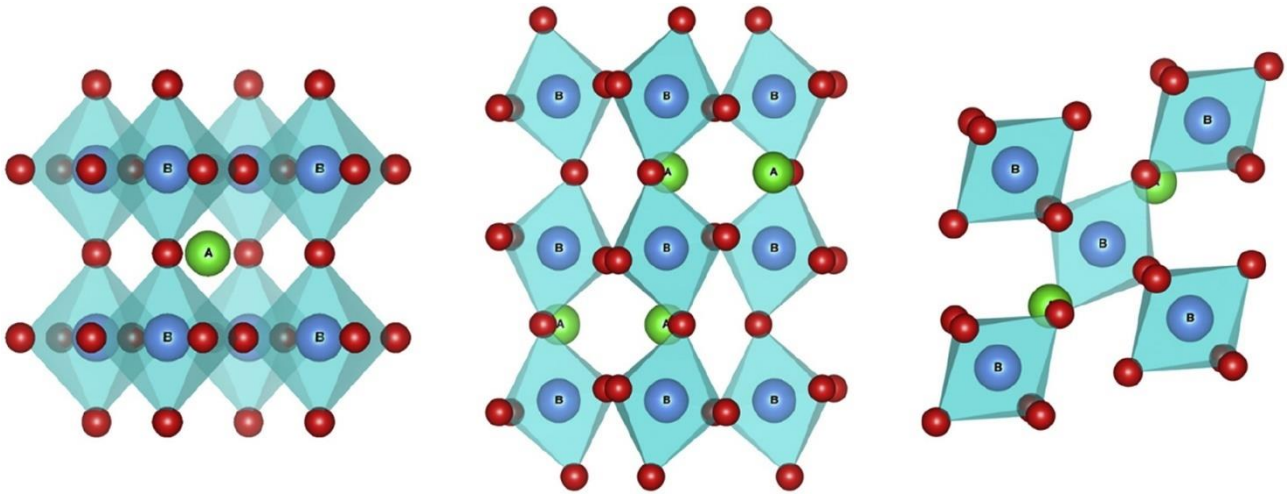

Fig.14 – Basic representation of a cubic structure (left), an orthorhombic structure (middle) and a rhombohedral structure (right). Red spheres are oxygen atoms. [49]

It has been reported that, speaking in terms of thermodynamics, the performances of most perovskites are worse with respect to simpler metal oxides like ceria. This fact can be attributed to the heat capacity, which is typically higher in perovskites, as well as partially to the low variation

of Gibbs free energy during the oxygen vacancies formation process (this hinders the development of the oxidation reaction, while being favorable for the reduction reaction instead). Analyses in a wide range of Cr doping extent and oxidation temperatures (from 800°C to 1500°C) have been carried out [50], showing for example that higher content of chromium in the B-site is related to lower equilibrium values of oxygen nonstoichiometry at constant temperature and oxygen partial pressure. Another interesting finding is for instance the fact that the perovskite's heat capacity, aside from presenting an increasing trend with the temperature, decreases when increasing the doping extent, therefore Cr doping leads to overall better thermodynamics. Concerning the overall variation of Gibbs free energy throughout one complete reduction-oxidation cycle, chromium doping not only reduces the $\Delta G°$ for the oxidative step, it actually reduces it more at high temperatures. This means that there is a high thermodynamic driving force for the oxidation reaction even at high temperatures, which enables the possibility to investigate isothermal cycles in future analysis.

As already mentioned, too high values of Cr doping lead to largely reduced oxygen nonstoichiometry, which is an undesired effect if the goal is to obtain good values of fuel productivity. This effect is mitigated at high temperatures, once again indicating the potentialities for isothermal or near-isothermal cycling for this class of materials. Following this approach, more high-temperature experiments on the involved material are present in the literature. [51] A key result that has been presented here is that, despite the better oxygen extent which characterizes perovskites without Cr doping, the overall fuel productivity is best for moderate chromium doping extents as shown in Fig.15. This fact is possible because the reaction rates of the doped material are largely improved. In investigating the LSMCr perovskite's kinetics, in fact, a three-times increase in the peak rate of the oxidation reaction is found for high chromium contents: remarkably such rates even exceed the typical rates displayed by ceria, which is normally known to have much better kinetics with respect to perovskites. As far as the oxidation temperatures are concerned, as it often happens, the reaction kinetics is directly proportional to higher temperatures. In other

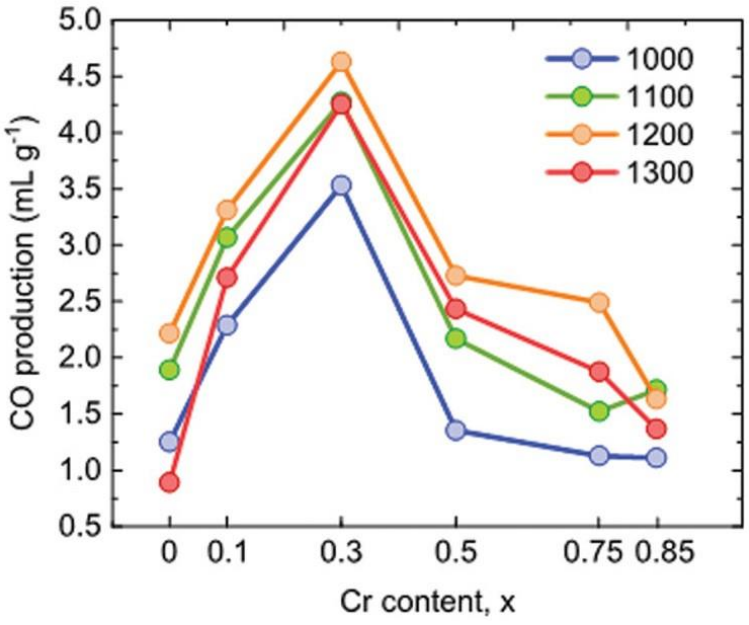

Fig.15 – Carbon monoxide yields for $La_{0.6}Sr_{0.4}Mn_{1-x}Cr_xO_3$ (T_{red}=1400°C). [51]

studies, focused again on the effects of chromium dopant on the oxygen and fuel evolutions during thermochemical cycles, coherent results were obtained. [52] Again, the temperature at which the oxidation step is performed appears to strongly impact not only the final fuel yield, but also the reaction rate of the involved reaction, while the effect on reduction is limited. Interesting evidence has been found of the beneficial effect of Cr substitution, especially when only small amounts of it are inserted in the material's structure. This recurring theme suggests the necessity of a compromise between a large presence of Cr (for improved thermodynamics and kinetics) against a smaller presence of Cr (to avoid too low values of oxygen nonstoichiometry).

The most relevant aspects about thermodynamics and kinetics involving LSMCr perovskites for their potential utilization in chemical looping processes have been discussed. Tthat being said it is still interesting to briefly mention other peculiar features or applications for this typology of perovskites. A couple of decades ago such materials were already being studied for their potential applications in the field of solid-state fuel cells [53] and still nowadays there is some ongoing research on the topic, particularly within the skyrocketing field of nanotechnologies, thanks to the highly appealing thermal stability and to their intrinsic capability of enhancing oxidation reactions [54]. Moreover, some lanthanum manganites have the capability of drastically changing their electrical resistance as a response to a magnetic field. This property, called colossal magnetoresistance, can prove to be useful in the construction of sensors, and is strongly improved by chromium doping [55]. Notably, varying the extent of Cr substitution in the perovskite's lattice is also useful since it allows to adjust the Curie temperature of the material (the temperature over which the material loses its permanent magnetism). LSMCr also presents magnetocaloric properties, that is, applying a magnetic field to it makes the material heat up. Such capability can be used to achieve magnetic refrigeration, in fact, letting the material radiate its heat while magnetized and subsequently removing the magnetism makes it possible to reach temperatures below the original one. [46]

3.3. Preliminary experiments

The preliminary experiments that will be described in this section have been carried out with the goal of selecting the proper reduction temperature, sample mass and volumetric flow rate, as well as interesting ranges of oxidation temperature and CO_2 concentration for the following set of experiments. Crucibles of two different sizes (45 µl or 95 µl respectively) made of a 90%-10% platinum-rhodium alloy were used, thanks to their capability to withstand temperatures up to 1600°C as well as not to react with the sample, which amounted to a few milligrams of LSMCr perovskite. The gas flow rate was initially kept constant at 200 Nml/min and the purge gas normally used was pure Ar, except from the oxidation phases, in which a controlled amount of CO_2 was injected too depending on the desired concentration, while still keeping 200 Nml/min as the overall flow rate. Bearing in mind the considerations of the past subsection, some additional studies on a variegate range of lanthanum manganese perovskites, useful in the preliminary selection of key thermodynamic conditions to be employed tentatively in the first experiments, are collected here in Tab.2:

Studied material	Reduction temperature	Oxidation temperature	Oxidizing agent concentration	Reference
$LaSrMn(Al/Cr)O_3$	1350°C	1000°C – 1200°C	50% H_2O in N_2	[52]
$LaSrMnO_3$	1400°C	800°C	20% H_2O in Ar	[56]
$LaSrMnO_3$	1350°C – 1500°C	800°C – 1000°C	40% CO_2 in Ar	[57]
$LaSrMnAlO_3$	1250°C	900°C	5% CO_2 in He	[58]
Various perovskites	1400°C	1050°C	50% CO_2 in Ar	[59]

Tab.2 – Preliminary review of the literature to set up the first experiments.

In the following sub-chapters, the experiments will be detailed. Results will sometimes be reported in terms of CO production yield, whose calculation is shown here below once and for all, assuming that the growth in the mass of the sample during oxidation is entirely caused by the inclusion in the perovskite's structure of oxygen atoms coming from CO_2 molecules. Given the measured mass variation in percentage ($\Delta m_{\%}$ [-]), the initial mass of the sample (m_0 [mg]) and the atomic mass of oxygen (MM_O=15,9994 [g/mol]), the yield (Y_{CO} [μmol/g]) is computed as follows:

$$Y_{CO} = \frac{\frac{\Delta m_{\%} \cdot m_0 \cdot 10^{-3}\, {}^{g}/_{mg}}{MM_O} \cdot 10^{6}\, {}^{\mu mol}/_{mol}}{m_0 \cdot 10^{-3}\, {}^{g}/_{mg}} \quad \left[{}^{\mu mol}/_{g}\right]$$

3.3.1. Experiment 0

The first experiment has been carried out to verify the sample reactivity and to have benchmark initial results. Coherently with what was found in literature, the oxidation temperature was selected to be 1200°C, with a reduction temperature of 1350°C. Temperature ramps were fixed at 20°C/min and they will be kept like this for most of the experiments, since the study focused on isothermal oxidation reactions, so the heating ranges were not thoroughly analyzed. CO_2 concentration was set at 40% (thus, 80 Nml/min of CO_2 and 120 Nml/min of Ar) during the oxidation phases. It was decided to perform 10 oxidation phases, each of them lasting 5 minutes. With the sample in this case consisting of around 8 mg of LSMCr, the obtained results in terms of mass variation are shown in Fig.16. Some relevant indications that can already be extrapolated from the presented diagram are about the initial reduction phase, which requires around 3 hours before stabilizing. Also, the mass increase during oxidation appears to be fast at the very beginning of each oxidation phase and slower afterwards. In addition, some potential anomalies like the mass growth at the very beginning of the test, or the sudden drop in mass which is present at the end of every oxidative step are present. It can already be stated here that the last two mentioned effects are present due to the flow rate variations within the machine, so they will not be considered in future runs, in fact they almost disappeared in ulterior experiments for which a blank test was performed.

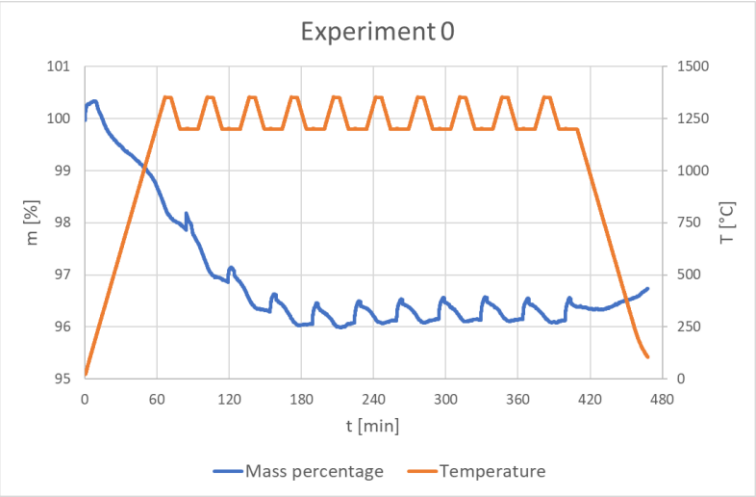

Fig.16 – First TGA experiment on LSMCr.

In Fig.17 the seven relevant oxidation phases are compared (the first three were discarded, since the initial reduction was not complete yet and the oxidation trends might have been affected by that). For this analysis, each curve has been rationalized, meaning that they have been scaled in such a way that every curve could be placed in the same range of the y axis, in order to compare their shapes one by one.

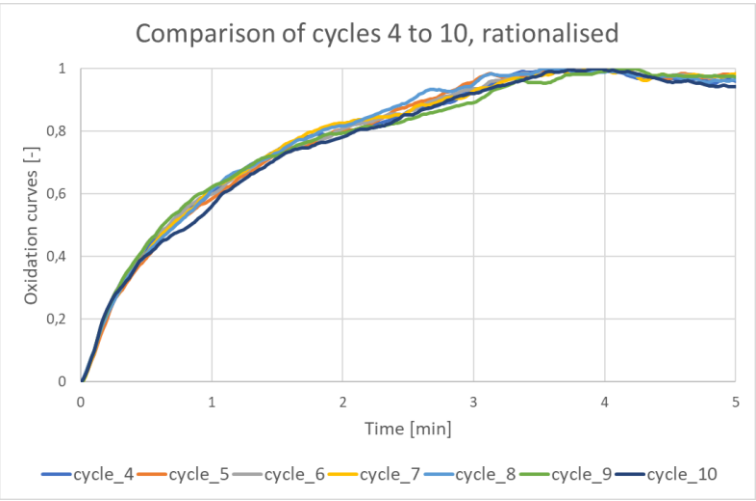

Fig.17 – Oxidation phases during the first experiment.

The curves turn out to be almost perfectly superimposed, therefore proving the capability of the material sample to withstand at least a small amount of reduction-oxidation cycles without deteriorating in a relevant way. Also, the trend is indeed faster in the very first minute, and in these specific conditions the oxidation seems to be complete (looking at the top of each curve) after around 4 minutes have passed, so the selected 5 minutes were just enough. The calculation of CO yields was not really the main objective of this experiment, especially because only 5 minutes of reduction at 1350°C were given between one cycle and the following one (most likely not sufficient to complete the reduction reaction, since it is usually slower than the oxidation one). Anyway, to provide an initial reference value, the average yield for these 7 cycles has been found to be 260.85 μmol/g.

3.3.2. CO_2 concentration range selection

In this experiment the focus was on the selection of a proper range of CO_2 concentrations for the upcoming experiments. The oxidation temperature was chosen to be 1100°C, while the concentration was varied, performing cycles with volume concentrations equal to 5%, 20%, 40%, 60% CO_2 in argon. The final value was forced by the equipment, in fact the maximum allowed flow rate of CO_2 inside the TGA machine is 121 Nml/min, and by keeping 200 Nml/min as the overall flow rate there was no option but to stop the investigation at 60% of concentration. This did not prove to be a problem though, since scaled up prototypes would most probably run at lower CO_2 concentration, and indeed 60% is already a very high concentration when compared to the available literature. The initial reduction was set to be three hours long, comprehending the initial ramp and two isothermal hours at 1350°C, to allow the material to completely reduce. The oxidation phases at high concentrations (namely 40% and 60%) were again chosen to be 5 minutes long, while the lower concentration ones were set to be 30 minutes long, with the goal of allowing the material enough time to complete the oxidation process. The isothermal reduction phases between cycles were set to 30 minutes as well. The usual plot showing the mass variations is presented in Fig.18:

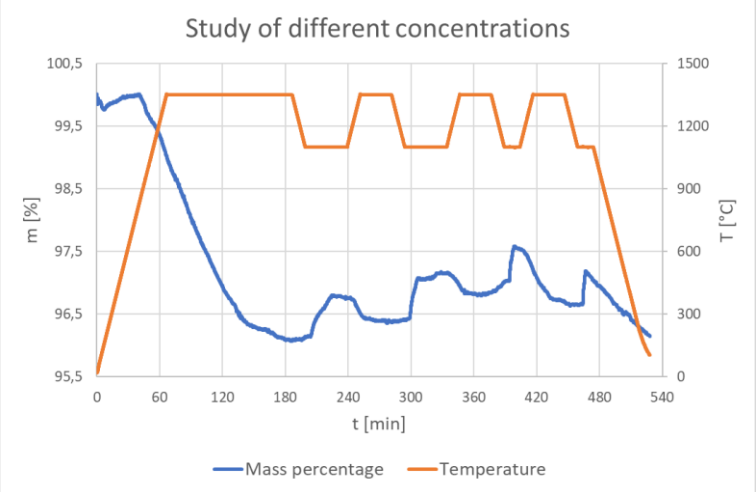

Fig.18 – Experiment with oxidation cycles at different CO_2 concentrations.

It is possible to notice that the first two cycles are characterized by a less steep increasing trend with respect to the other two. This result makes perfect sense, but there are some peculiar characteristics to be observed in this plot. Generally speaking, and this remains valid for the following experiments too, the trend characterizing the initial reduction phase takes a different shape with respect to the previous one. It was anyway decided not to focus on that since the reduction reaction is not the subject of this study. In addition, at the end of the oxidation phase with 20% CO_2 (that is, after around 320 minutes from the beginning of the experiment) the sample, after remaining at a stable value of mass for a while, experiences a quite unexpected increase which even keeps going for a couple of minutes after the CO_2 supply is shut down. It was therefore decided to not consider the final portion of that oxidation phase, which is the reason for it only being 20 minutes long in Fig.19. The comparison of the various curves is this time performed by simply giving them a common starting point, without rationalization, since their time extent is different from one to another. In the diagram the oxidation curve related to the 60%

concentration (that is, the fourth cycle) has been cut after only 3 minutes, since after reaching its peak in that small amount of time it showed an unexpected decreasing trend. The most interesting parameter to be considered in this case is the steepness of the curves in the first minutes of oxidation, which gives indications about the reaction rate and of course is directly related to the duration of the entire oxidative phase. It appears clearly that higher CO_2 concentration leads to faster oxidation, with the curves reaching similar apexes in terms of magnitude, but in different times. It is in fact required to respectively wait for around 20 minutes, 8 minutes, 5 minutes, and 3 minutes in order to reach the complete oxidation of the sample.

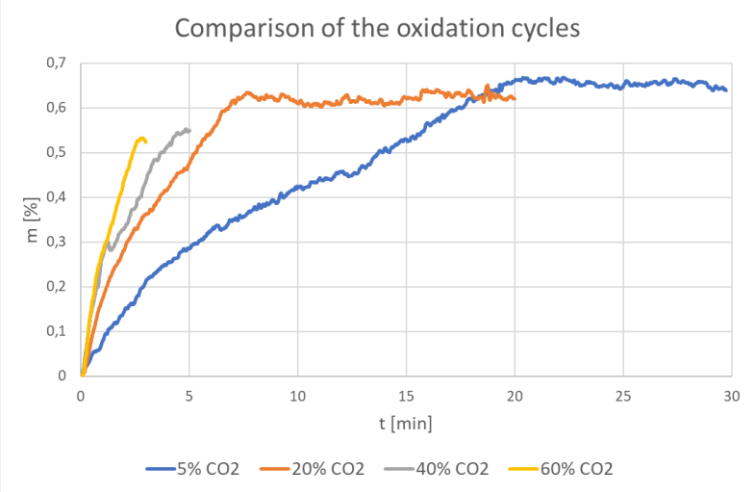

Fig.19 – The CO_2 concentration strongly affects the slopes of the oxidation cycles.

From a practical point of view, but also from the perspective of choosing the conditions in which the material shows its best performances, faster oxidation trends should be preferred. It could be a bad idea though to select 60% as the reference concentration for the future tests, since it is very close to the maximum capabilities of the experimental apparatus (as mentioned, 121 Nml/min is the maximum supply of CO_2, and a concentration of 60% means to work at 120 Nml/min of CO_2). Also, it was not possible to find in literature similar examples with such a high concentration of the oxidizing agent. Moreover, it is true that employing a 40% CO_2 concentration requires longer times, but in the very first minute the performances are basically the same for both the third and the fourth cycle (the curves are superimposed), so in the definitive tests a range of CO_2 concentration centered in the 40% value will be used.

3.3.3. Example of a definitive test

Moving on with the experimental section, it was time to go for one attempt of the actually relevant experiments, those to be used later on as the basis for the kinetic analysis of LSMCr.

Such experiments had the goal of exploring the oxidation behaviour of the material in a proper range of temperatures and CO_2 concentrations. Particular focus was going to be put on the very first minutes, characterizing the reaction rate, and on the final value of mass gained. This test (Fig.20) was designed as the first one of three, with every cycle being performed at 1100°C (in principle, the following experiments would have been carried out at 1050°C and 1150°C respectively). The first cycle was there just to be discarded, then there were two identical cycles at 30%

CO_2 concentration, followed by two identical cycles at 40% CO_2 concentration and two identical cycles at 50% CO_2 concentration. It was decided to employ a sample with larger mass (around 20 mg of LSMCr, notice the much lower mass percentage decrease in the following diagrams with respect to the previous ones) so the large crucibles were used. Moreover, in order to reach complete reduction and oxidation every time, it was decided to increase the duration of the various phases setting three hours as the initial reduction, as well as 90 minutes of reduction and 30 minutes of oxidation per cycle.

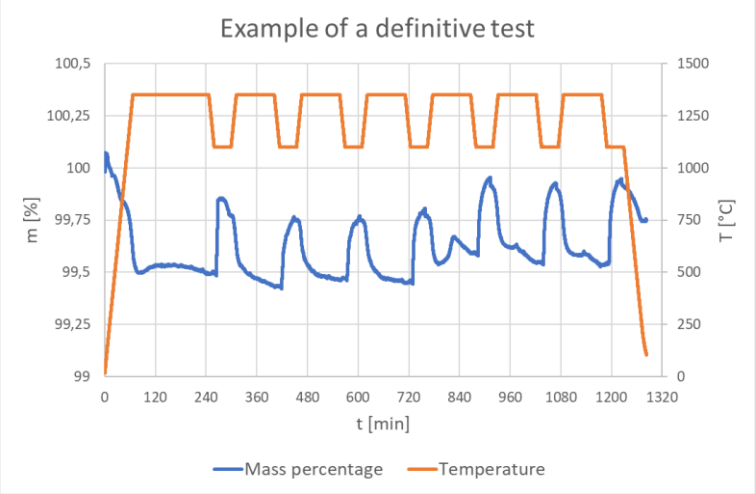

Fig.20 – Longer experiment to explore the entire range of CO_2 concentration (30% to 50%), while keeping the same oxidation temperature.

The results prove the usefulness of the initial cycle which immediately catches the eye for being completely out of scale with respect to the others. This has been a recurring pattern of the studied material: the first cycle with the perovskite being still fresh presented different behaviour with respect to the cycled material, and evidence of similar behaviours have been found in literature too [60]. Moving on, the oxidation profiles are reasonably distributed, with the trends being less steep in the 30% CO_2 case and so on, even though some oscillations are present, and the oxidation did not reach its final stable state, since at the end of the 30 minutes the trends are still increasing as it is possible to see in Fig.21.

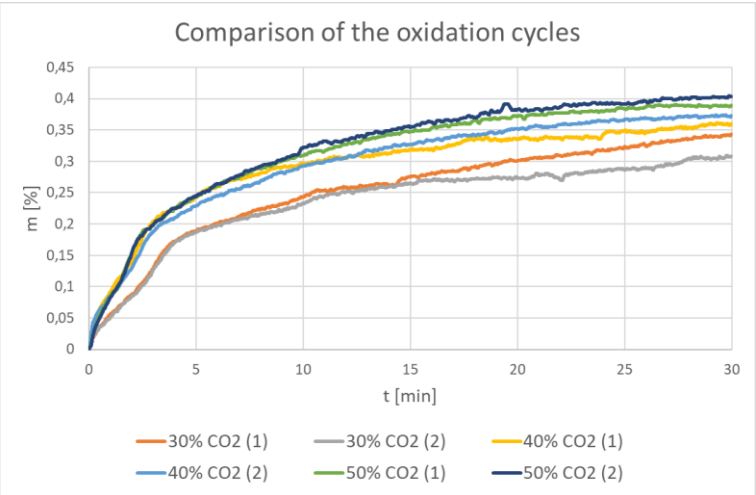

Fig.21 – Oxidation trends at 1100°C, the couples of cycles featuring the same CO_2 concentration are similar one to each other.

Despite the fact that it appears like complete oxidation has not been reached, it is still interesting to postprocess a bit the data related to the oxidation profiles, especially since they seemingly show an initial increase which is not homogeneous. In order to study this behaviour more deeply it is useful to rationalize the data going from the mass percentage gain to the extent of reaction (α), which is 0 when the reaction begins and 1 when the reaction is complete (here the 30 minutes mark is chosen as the point in which the reaction concludes, even though, as mentioned, the reaction is likely not over yet). Notice how, in such a plot (Fig.22) where the magnitude of the mass gain is not relevant anymore, the trends are very similar in shape from one cycle to the other.

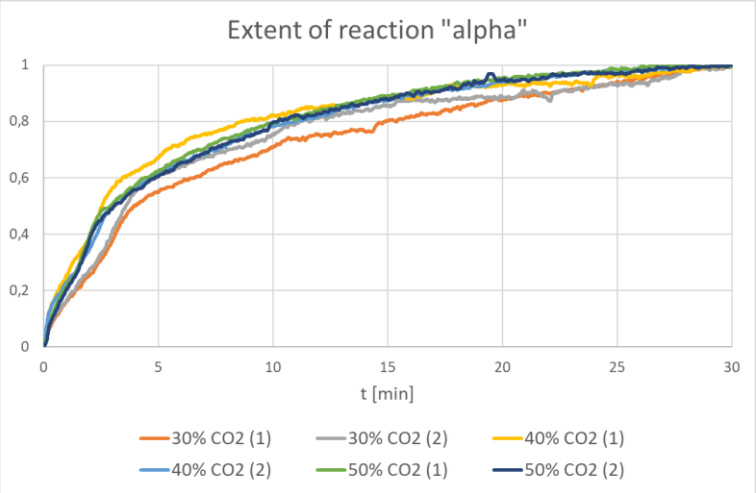

Fig.22 – The trends are still slightly increasing after 30 minutes.

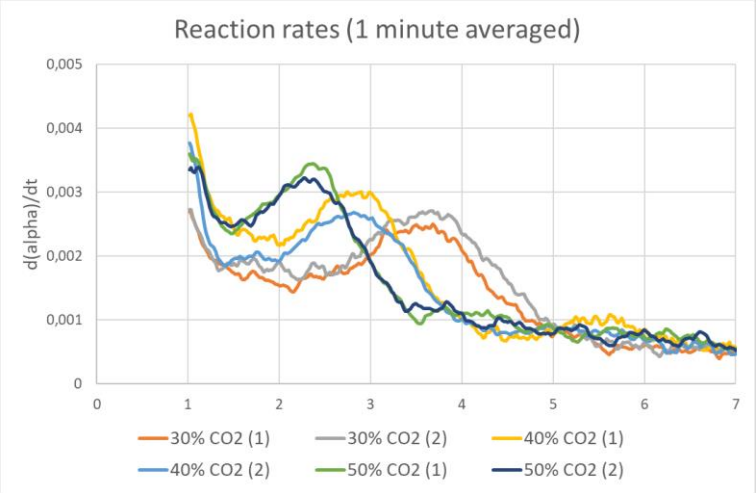

Fig.23 – The reaction seems to accelerate after 2-3 minutes from the start.

After doing so, it is possible to calculate the derivative of the extent of reaction, obtaining an indication of the reaction rate. In particular, the derivative can simply be expressed as the subtraction between two consecutive values of α divided by the time interval between them (but in every experiment data has always been collected with time intervals of 1 second, therefore it was not necessary to divide for it). From the oxidation profiles it is safe to expect a high rate in the first minutes, with a decreasing trend while the reaction goes on. For this reason only the very first minutes of oxidation are shown in Fig.23. In the displayed plot the results in terms of

reaction rate are averaged over a minute in order to make them easier to read (second by second results are hard to interpretate because of the inevitable oscillations in the recorded oxidation profiles) and provide some interesting insights. First of all there are relevant differences between the cycles (the identical couples have similar trends though), but more importantly a peculiar double-peak effect is highlighted.

3.3.4. Potential carbonates formation

This time the experiment (Fig.24) was designed in order to reach the end of the oxidative process during every cycle, therefore it was decided to oxidize the material for 90 minutes, and the experiment was carried out at the lower of the three preliminarily selected temperatures (that is, 1050°C) just to be sure that such long oxidation phases would be enough for every condition. Aside from that, the temperature program followed the same approach as the previous one: a cycle to be discarded followed by three couples of identical cycles at different CO_2 concentrations.

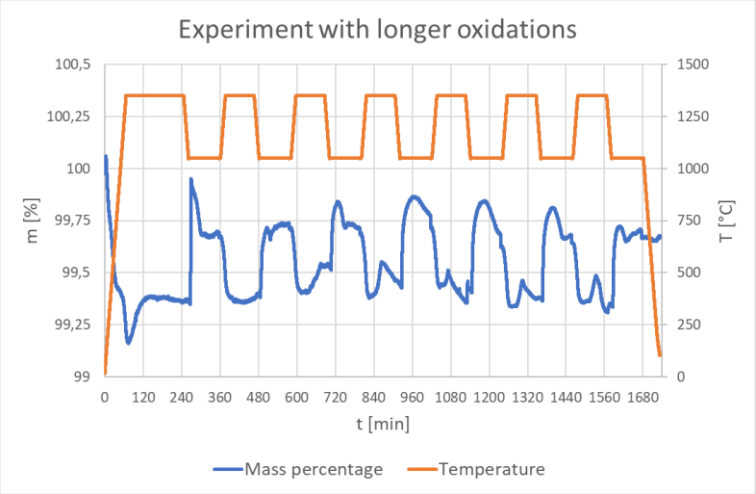

Fig.24 – Long experiment performed at 1050°C and 30% to 50% CO_2 concentration.

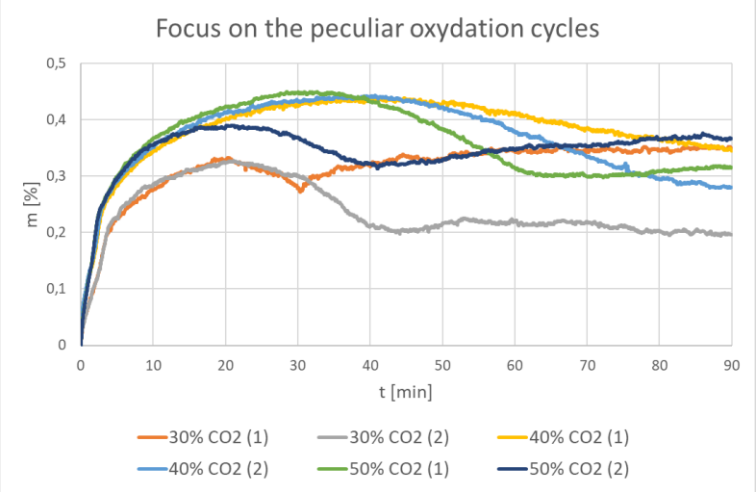

Fig.25 – Resulting trends during 90 minutes long oxidation cycles.

The obtained profiles though presented some unexpected trends, as displayed in Fig.25. Instead of having an increasing tendency followed by a plateau, they are characterized by different

behaviors, including relevant mass losses which are hard to explain from a physical point of view. Indeed, the oxidation phase involves the absorption of oxygen in the material's lattice and thus should only lead to increasing or stable trends. Not to mention the fact that throughout the oxidation the TGA conditions are kept constant, so the sudden variations in the trends that can for instance be observed in the plot describing the first cycle cannot be explained as well. Overall, the results of this experiment indicate that either the material is not stable in these conditions, or that external factors have a way too big influence on the measurement.

One possible interpretation of the resulting trends with the mass increasing for a long time and then decreasing could be based on the idea of an undesired compound being formed and then degraded in the middle of the reaction. There is in fact evidence in literature about the possible formation of carbonates for perovskites doped with strontium atoms when employing perovskites in a CO_2 rich environment. [61] The formation of carbonate compounds (e.g. $SrCO_3$) is a problem for the reaction kinetics, and it is reported to be strongly dependent on the amount of strontium at the surface of the material. For this reason, doping the surface with aluminum is a typical approach to hinder their formation, while also oxidizing at higher temperatures should help in solving this issue. Therefore, trying to understand if the studied perovskite was actually prone to carbonates formation, a further experiment (Fig.26) was modelled on the basis of a test present in the literature.

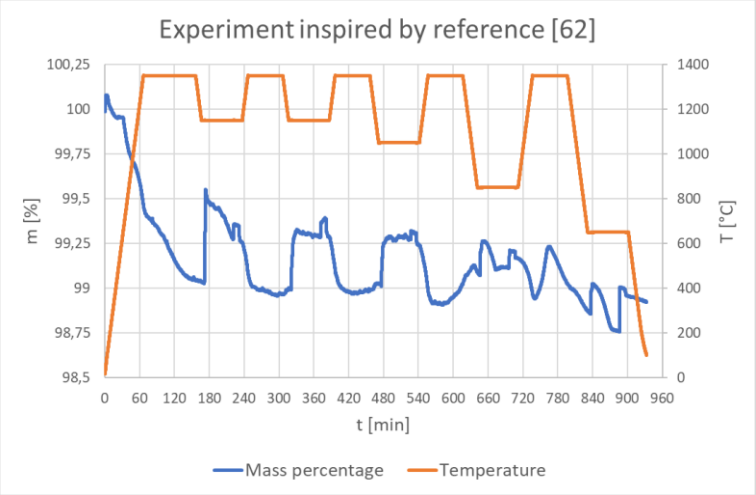

Fig.26 – Carbonates formation test based on literature. [62]

The idea is simply to perform the redox cycles at various oxidation temperatures (1150°C, 1050°C, 850°C and 650°C are the proposed ones) for 50 minutes each, followed by 10 minutes of oxidation at the same temperature conditions, but in a different, much more oxidizing atmosphere. The first 50 minutes were therefore conducted in a 50% argon 50% CO_2 atmosphere, while the final minutes were performed in synthetic air (thus, with a 20% oxygen concentration). The obtained results, reported more in detail in Fig.27, are definitely interesting. It is possible to see that the two cycles at lower temperature present the weird decreasing trend that was witnessed in the previous experiment, but more importantly, the initial mass increase reaches higher levels than the one reached at the end of the cycle in the more oxidizing atmosphere. This can only be explained with the formation of some unexpected compounds (possibly strontium carbonates, as mentioned) in the early stages of the cycles. In fact, it is not possible that the material gets

more oxidized by CO_2 with respect to oxygen. The cycles at higher temperatures instead show a reasonably flat profile, followed by a mass increase when the oxidation in air begins, indicating the fact that possible formation of other compounds is at least much smaller, if not absent, in such conditions.

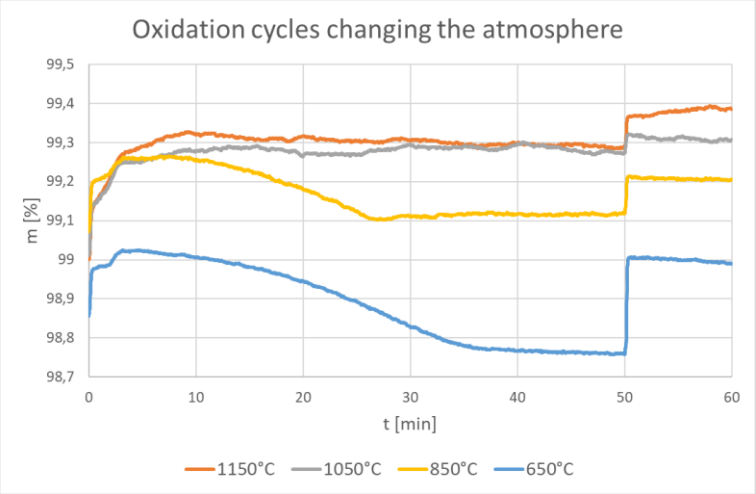

Fig.27 – Complete reoxidation with air in the last 10 minutes.

Focusing again on the potential formation of a carbonate phase, it was decided to take advantage of another literature reference [63] and to design an experiment similar to the one presented there. The goal in this case was to obtain some insights about at which temperature the carbonates might decompose, or simply not form at all, with reasonable accuracy. Such a test (Fig.28) was held at 50% CO_2 concentration following (after the usual initial cycle to be discarded) an oxidation phase characterized by a slow temperature gradient starting from 400°C all the way up to 1350°C. This will be the only non-isothermal oxidation phase discussed in this work.

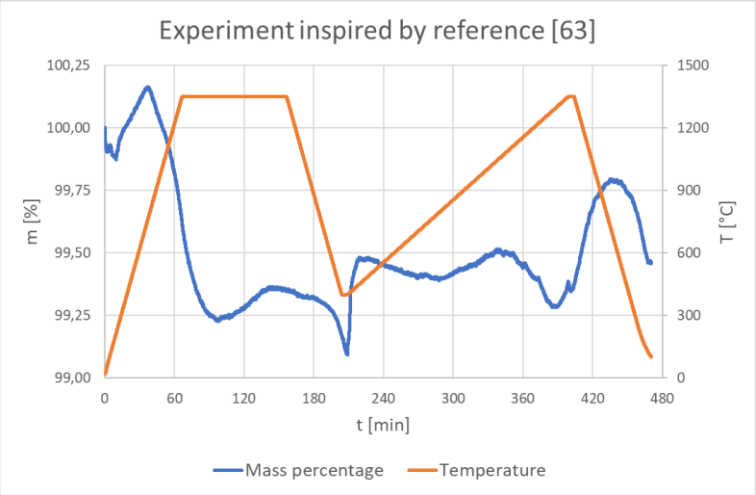

Fig.28 – Additional experiment based on literature to obtain further information about the behaviour of LSMCr at different temperatures. [63]

The results are not extremely clear, but focusing on the oxidation phase only (Fig.29) it is possible to see a mass drop at around 1100°C, which could indeed be caused by the decomposition of previously formed carbonates.

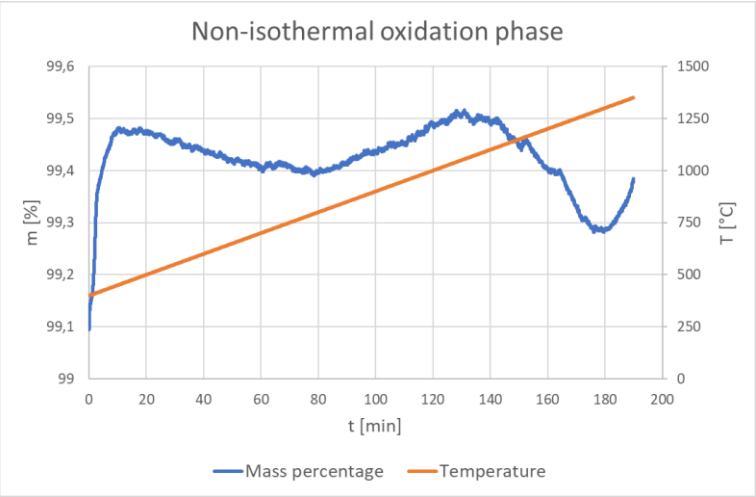

Fig.29 – Oxidation phase at constant heating rate equal to 5 °C/min, differently from the usually employed one of 20 °C/min.

3.3.5. Temperature range selection

Given the indications of the last two experiments the focus was put on oxidation phases at high temperatures, to check whether the material showed more stability. It was therefore decided to run a 90 minutes long oxidation phase at 50% CO_2 concentration at various temperatures to verify and study the material's behaviour, starting from 1200°C. In this subsection the LSMCr mass inserted in the crucibles is still around 20 mg.

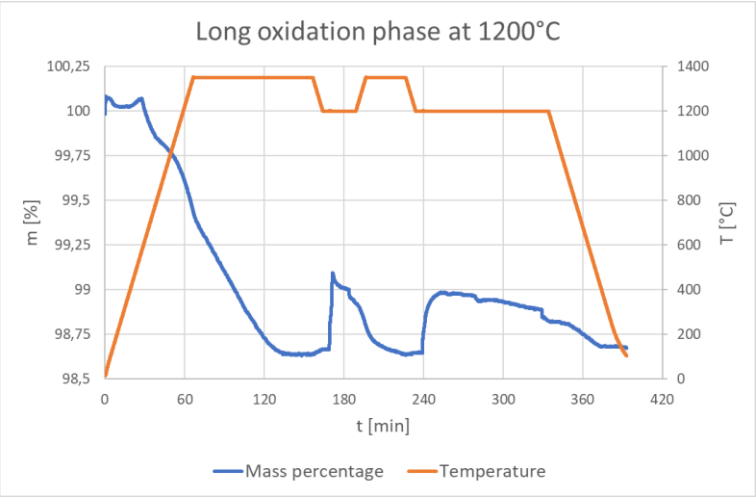

Fig.30 – Further investigation of the material's behaviour, higher temperatures look promising.

The obtained profile (Fig.30) shows again the unexpected mass decrease in the long run (noticeable slightly before the 300 minutes mark), but the effect is much less relevant than the one observed in the previous experiment at 1050°C. More importantly from the kinetic point of view, after few minutes the oxidation seemed to be complete, so a focus on the first 15 minutes was carried out with the already discussed methodology (Fig.31). The increasing mass variation trend is a quite clean one, and once again it is possible to notice the double contribution on the reaction rate (again, that curve represents the derivative of the extent of reaction alpha, averaged

on one minute) even though it is noticeably less relevant with respect to the one that was present in subsection 3.3.3.

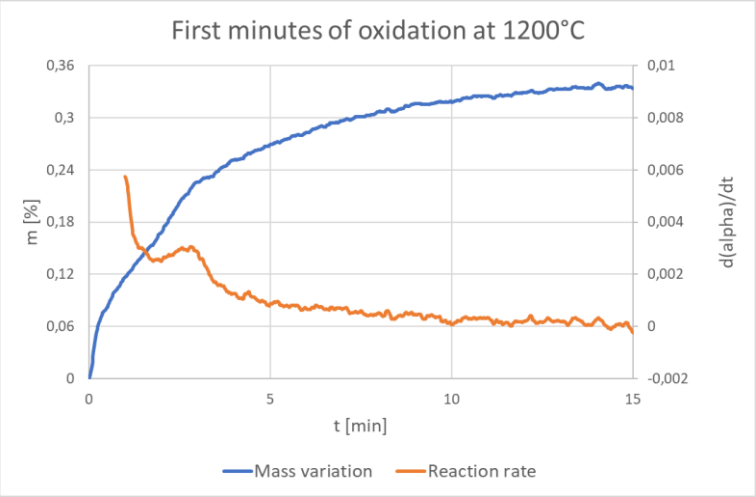

Fig.31 – Focus on the first minutes of the oxidation phase.

Overall, data similar to these ones are definitely reasonable and do not present too many ripples, looking promising from a kinetic analysis perspective. The presence of a "double step" reaction rate profile could make the calculations more complex, but it is still to determine if the "secondary" effect is due to kinetic reasons or not. As a hypothesis, the fact that it considerably reduced at higher temperature could in fact indicate that its presence is due to some residual carbonate formation. Following the same approach, another 90 minutes, 50% CO_2 oxidation cycle was run at even higher temperature, particularly at 1350°C, as shown here in Fig.32.

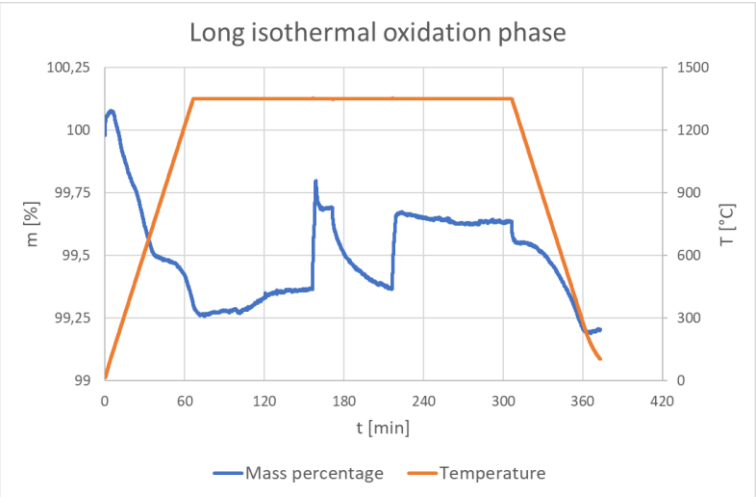

Fig.32 – Testing the isothermal operation at 1350°C of LSMCr.

This means that in this specific case the reduction-oxidation loop was an isothermal one, so the only responsible for the reaction switch (from reduction to oxidation and vice versa) will be the variation of the atmosphere, from pure argon to the 50/50 mixture of CO_2 and argon. Generally speaking, performing isothermal cycles at such high temperature in a future mid to large scale prototype would mean to employ a lot of energy to keep the temperature high, but on the other hand it would strongly improve the overall cycling efficiency due to the absence of transition phases. The concept of isothermal thermochemical cycles has already been discussed, and

chromium doped perovskites were specifically found to adapt particularly well to such conditions, as reported in subsection 3.2, so the idea to run isothermal cycles is definitely not unreasonable (nor it is new, there already are plenty of studies in literature about isothermal chemical looping processes [34]). That being said, the oxidation phase displays a nice and flat trend throughout all the 90 minutes, once again proving the better stability of LSMCr at high temperatures. Noticeably, it appears like the complete oxidation is already reached after around 4 minutes, making it once again interesting to study only the first portion of the experiment (Fig.33). The reaction rate is clearly higher at the beginning with respect to the previous case, which makes sense given the higher temperature, and again the "double step" behaviour is less prominent, though it remains visible. This makes it difficult to attribute the potential "secondary reaction step" to carbonate formation, since at such high temperatures carbonates should not be formed, so it might actually be that the material is characterized by complex reaction kinetics.

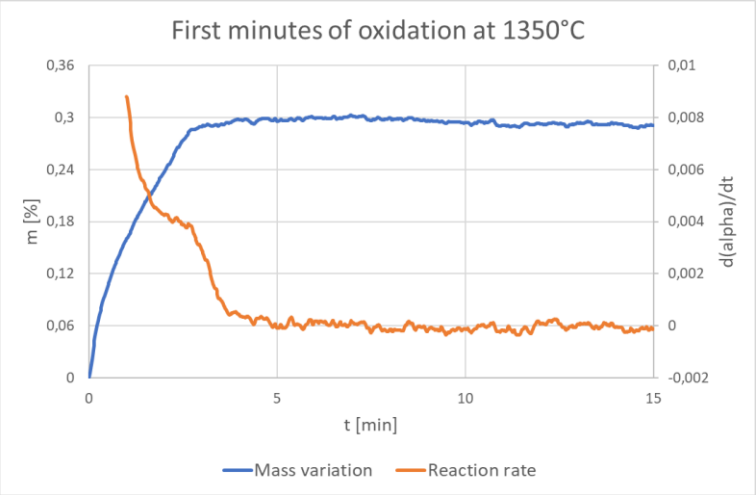

Fig.33 – Moving at relatively high temperatures the reaction rate trend starts losing its "secondary" peak.

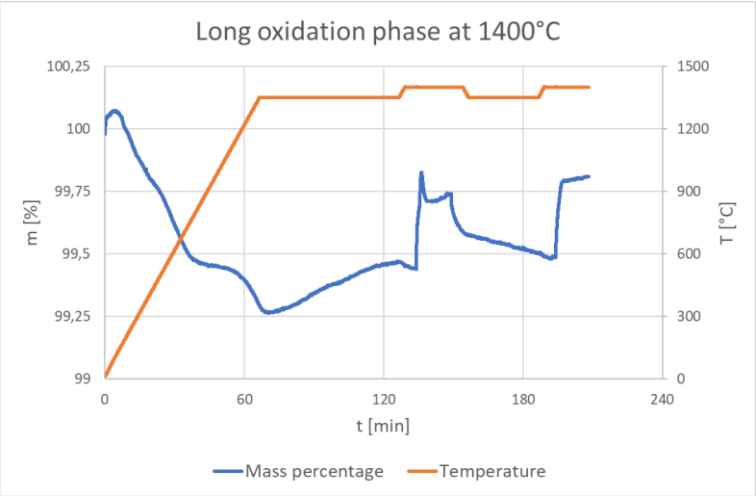

Fig.34 – Oxidation temperature is here even higher than the reduction temperature.

For a deeper understanding of the material's behaviour, it was even decided to run an oxidation cycle at 1400°C (Fig.34). Notice that in this case it was decided to keep the reduction temperature at the usual 1350°C, to be as coherent as possible with the other two experiments of this section, but in a practical application oxidating at 1400°C would for sure be met with reducing al 1400°C

too, for efficiency related reasons. Again, the oxidation profile looks flat as in the previous case, with the reaction being even faster (reaching a seemingly fully oxidized state even before 3 minutes). As expected, the reaction rate trend appears to be quite close to a single step one, even though it is still possible to observe a slight indication of the "secondary step" (Fig.35).

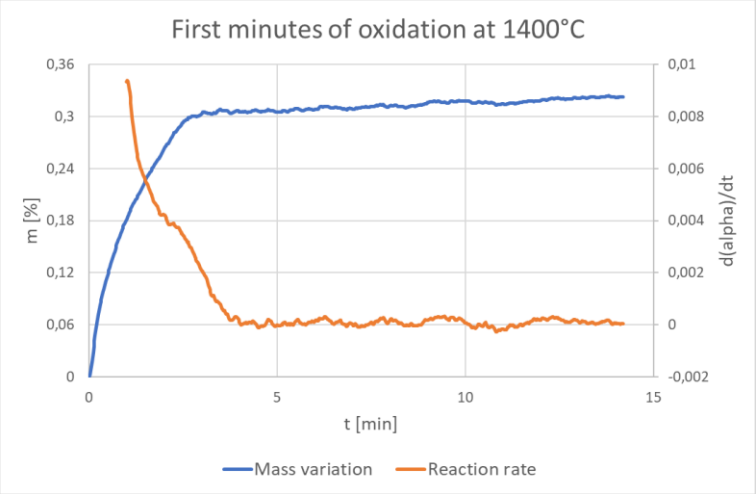

Fig.35 – The reaction rate is simply decreasing at high temperatures.

3.3.6. Sample mass and flow rate selection

In order to optimize every potentially impacting parameter it was then decided to perform a test with the specific goal of setting a reasonable flow rate for the experiments, which was always kept at 200 Nml/min until this point. The experiment (Fig.36) was designed to be as comprehensive as possible, featuring five different mass flow rates (from 160 Nml/min to 240 Nml/min), each of them exploring a triplet of oxidation profiles, respectively characterized by 30%, 40% and 50% CO_2 concentration in the gas flow. The oxidation temperature was here set to be 1100°C, in fact this experiment was carried out before the ones about the temperature range selection. Because of the large number of cycles that had to be performed it was decided to keep them quite short, with reduction phases 30 minutes long and oxidation phases 5 minutes long. As far as the

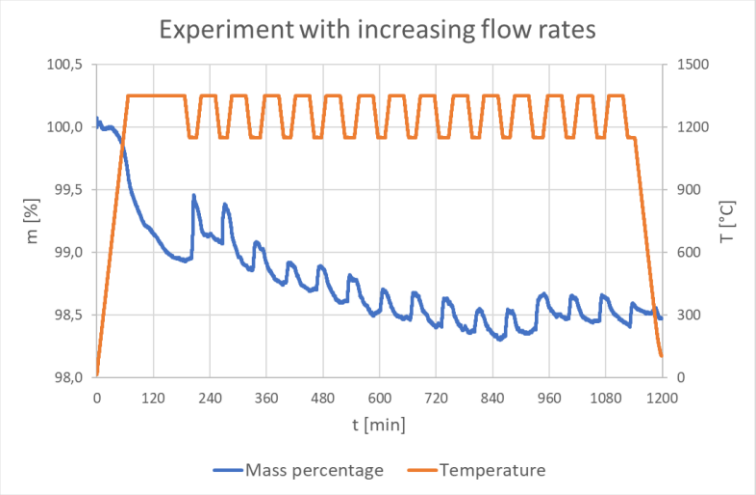

Fig.36 – This experiment featured three short oxidation cycles for each of the investigated volumetric flow rate values.

sample masses are concerned, this test was first run with around 8 mg of LSMCr, but the results were not satisfactory, so it was decided to perform it again with around 20 mg of LSMCr, obtaining less oscillatory and more reasonable results. The various oxidation phases were investigated in terms of CO yield. The first fact to notice is that the resulting carbon monoxide yields are much lower with respect to the one reported for Experiment 0, at around 120 μmol/g. This makes sense since employing higher masses makes it probable for the CO_2 flow not to reach the bulk material in 5 minutes of oxidation only, and the unit of measurement for the CO yield is micromoles of fuel per gram of perovskite, therefore if some material does not react the final yield values will be lower. Overall, the results are close to the expectations, except from the very last cycle that will be considered an anomaly (Fig.37). In particular, there is a clear relation between CO_2 concentration and CO yield at fixed mass flow.

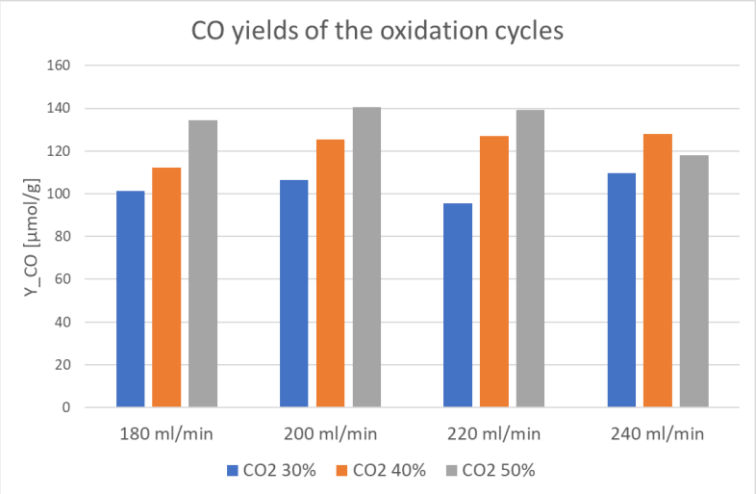

Fig.37 – Dependency of the CO yields from the flow rate, cycles at 160 Nml/min have been discarded as it is usually done with the initial one.

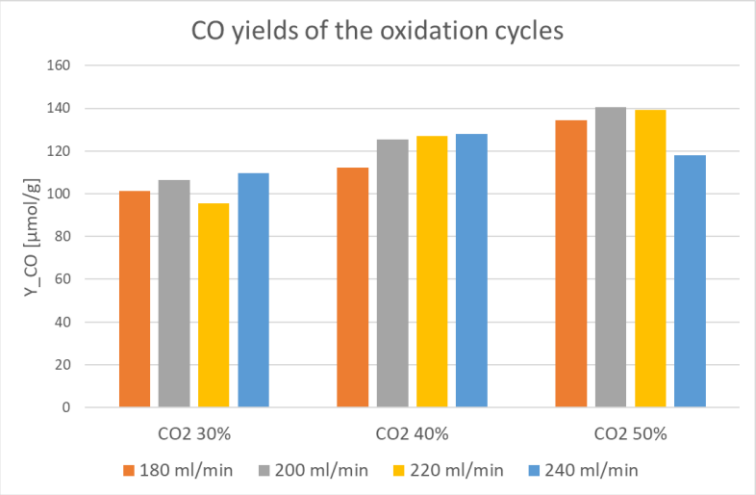

Fig.38 – The CO_2 concentration does not affect the performances too much.

Oxidation cycles at the same CO_2 concentration present a slowly growing yet similar final yield with respect to the growing mass flow rates. From Fig.38, where the same results are simply rearranged in another way, it appears that increasing the flow above 200 Nml/min has only a very small impact on the final results. This is positive, since it means that remaining above that mark makes the flow rate not to affect the data in a relevant way. That being said, a slow rising

trend from 200 Nml/min towards 240 Nml/min seems to still be present, indicating that a mass flow rate equal to 240 Nml/min would be the most suitable. It was unfortunately impossible to explore higher mass flow rates because of the inherent technological limits of the employed experimental setup (specifically, of the TGA).

The optimization of the volumetric flow rate is of course closely related to the optimization of the mass of LSMCr to be put in the crucible. The final goal is in fact to perform the experiments in a situation in which neither the flow rate nor the sample mass have an influence on the kinetics of the investigated reaction. In other words, the reaction must not be limited by a low flow rate of CO_2 not supplying enough molecules of the oxidizing agent to the material, nor by a large sample mass introducing some mass transport phenomena from the surface to the bulk of the sample. [64] Both these mechanisms are examples of external factors which modify the reaction kinetics, potentially making the kinetic study not relevant since the goal is of course to study the actual reaction, not a slowed down version of it. For this reason, to conclude this preliminary section it was decided to check the oxidation behaviour of a much smaller sample. Indeed, the choice of using around 20 mg was done with the goal of obtaining smooth enough plots (large masses mean smaller oscillations in the diagrams of mass percentage) but running at higher temperatures proved to solve many stability issues. The experiment (Fig.39) was designed to be performed with just a layer of LSMCr powder covering the bottom of the crucible (i.e. from 2 mg to 3 mg of perovskite). It consisted of the usual initial cycle followed by one relevant cycle, at 50% CO_2 concentration and 1350°C, which were the conditions leading to the fastest kinetics between the ones that would possibly have been investigated in the following.

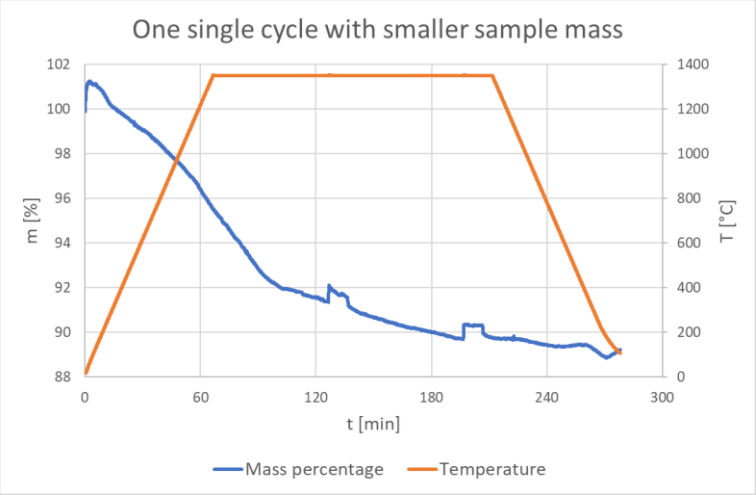

Fig.39 – Experiment with low sample mass to assess the impact on the measurements of this last parameter.

The first thing to be noticed here is about the overall mass decrease during the experiment. Data in fact show that more than 10% of the sample mass has been lost during the reduction phases, which is a completely unreasonable value if it is to be ascribed to reduction phenomena only, the material is surely not capable of desorbing oxygen for 10% of its weight. Such a behaviour can be explained with external factors, for example it is possible that the initial tare of the instrument was made in an inaccurate way. Also, the material might have contained some humidity that evaporated once the temperature started rising. That being said, the profile turned out to be

reasonably clean, therefore it would have been possible to employ similar sample masses in the following experiments. Looking at the following comparative plot (Fig.40), it clearly appears that the utilization of large masses introduces some important delay in the material's kinetics, most probably due to the diffusion time of the CO_2 flux towards the bulk of the sample (in other words, due to mass transfer phenomena). Using such small masses on the contrary guarantees that the entirety of the sample will be in contact with the CO_2 flux, avoiding diffusion-related limitations on the kinetics. It is true that the displayed curves are characterized by different temperatures as well, but temperature alone cannot explain such differences in the observed trends.

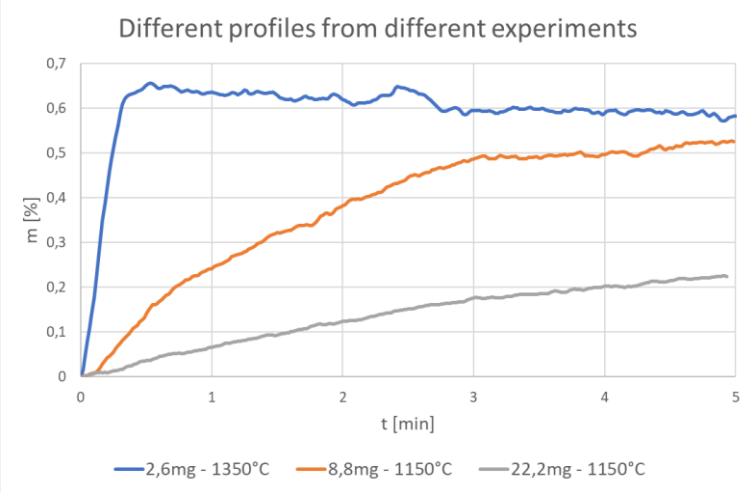

Fig.40 – Results from different experiments are compared here.

In conclusion, the main result of this subsection is the fact that the sample mass has a much bigger influence on the material's kinetics when compared to the volumetric flow rate, and indeed strong effects of sample mass on reaction kinetics have been reported in literature [65]. It was therefore decided to run the final set of experiments with small masses (in the range 2-3 mg) of LSMCr, just a thin layer of powder covering the bottom of the crucible. The flow rate was instead simply set at the usual 200 Nml/min value: raising it to 240 Nml/min had a limited influence with the 20 mg sample already, so it is reasonable to assume that with such smaller masses the flow rate effect would be irrelevant. Nevertheless, too low flow rates could mean that impurities or undesired residual oxygen would not be correctly carried away from the crucible area, so the mass flow rate was still selected to be sufficiently high.

3.4. Definitive experiments

The natural following of all the described tests was another set of experiments performed in more specifically targeted conditions. First of all, it was decided to design the experiments by keeping the CO_2 concentration constant while varying the oxidation temperature of the cycles. This choice was made with the goal of saving some time, since it was decided to investigate a range of 4 different temperatures and only 3 different concentrations. Also, the idea was to better appreciate the variations in the reaction rates in the first seconds of every oxidation phase in the same run (variations due to concentration are mostly relevant in terms of final mass gain, which will be clear anyway by comparing different experiments). Three experiments were performed,

at 30%, 40% and 50% CO_2 concentration respectively, and each one of them involved four relevant reduction-oxidation cycles for each of the selected temperatures (namely 1200°C, 1250°C, 1300°C and 1350°C). The reduction phases at 1350°C were still kept quite long in order to be sure of reaching the complete reduction of the material, while the oxidation phases were designed to be a bit shorter, due to the small sample masses employed. There was still an additional cycle to be discarded at the beginning of each experiment, as well as an additional hour in which the temperature was kept isothermally at 200°C, just in case some humidity was present in the sample. Again, the employed masses were small (close to 2,7 mg in all cases), with 200 Nml/min as overall volumetric flow rate. The postprocessing of the data related to the first minutes of the oxidation cycles was then performed as already explained in subsection 3.3.3.

The first experiment was performed at 30% CO_2 concentration, but only the results of the experiment at 40% are presented here, together with a comparison between the three, while the extended results for the other two definitive tests can be found in Appendix B. The resulting trend for the entire test (Fig.41) presents some strange points, for example after the initial cycle the material reduces considerably more than after the initial reduction phase, perhaps due to some rearrangements in the material's structure during this cycle. This is not a problem anyway, the experiments were designed with this additional cycle exactly to let the sample stabilize, the fresh material showed a different behaviour from the already cycled one from the very beginning of this experimental study. In addition, after around 13 hours, right during the last oxidation step, there is an unexpected rise in the sample mass, most probably due to some external factor.

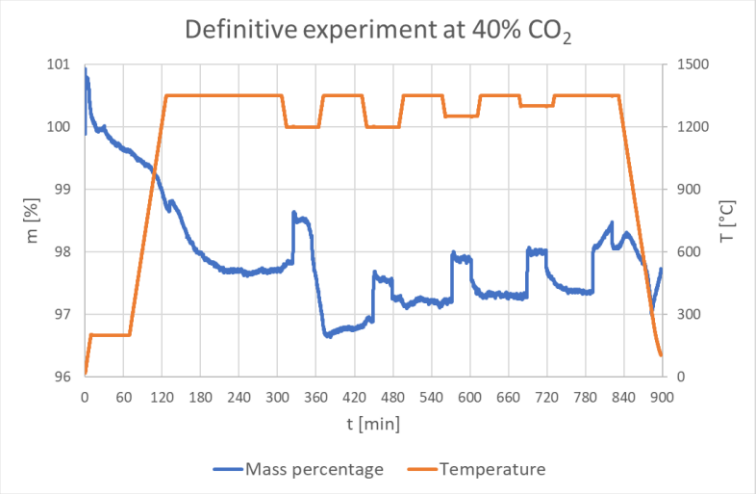

Fig.41 – Comprehensive experiment conducted at constant CO2 concentration while varying the oxidation temperature from 1200°C to 1350°C.

Employing small sample masses in fact makes such external oscillations more visible when looking at the entire test, but it must be pointed out though that such phenomena do not affect the interesting portions of the experiment, that is, the oxidation cycles. The first few minutes are the most relevant, in Fig.42 the first 10 minutes are displayed, showing that after 3 minutes the oxidation can indeed be considered practically over. The final results show reasonable trends for the oxidation cycles, with the one at higher temperature being the fastest one in reaching a stable level as proved by the plot displaying the reaction rates (Fig.43). Coherently with the previous plot, the trends in this specific diagram reach zero after less than two minutes already.

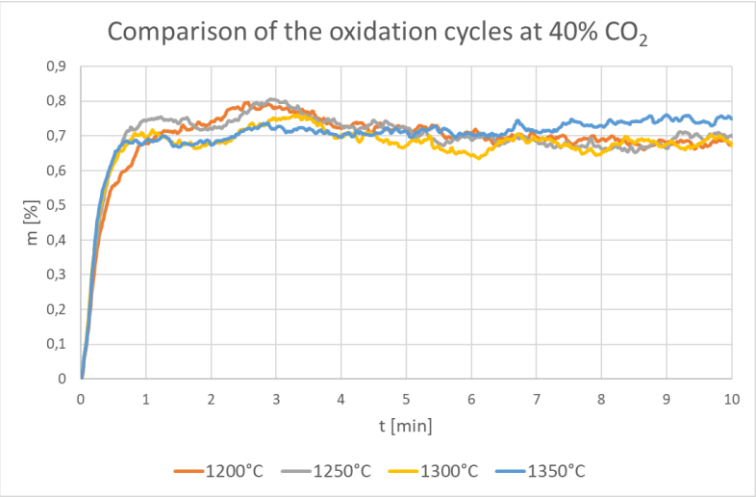

Fig.42 – The first few minutes are the interesting ones, later on the trends flatten out.

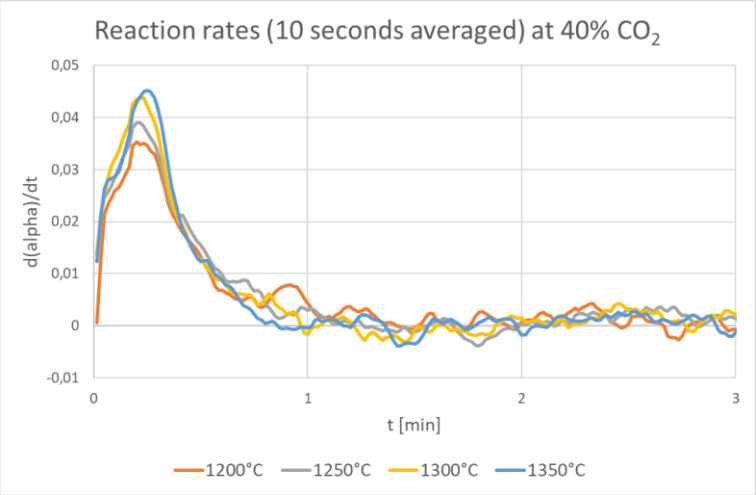

Fig.43 – The reaction rates have a maximum after few seconds and then tend to zero.

The information contained in the plot describing the reaction rates is surely important and it will be extensively utilized in the following sections of this work. Nevertheless, it is useful to display basically the same data in a more concrete way. In Fig.44 the sample mass variation (measured in mg) in one second is the starting point for the calculation of the CO production rates. The idea is similar to the one already applied to the calculation of the fuel yields for an entire cycle which was described in subsection 3.3. Given the measured mass variation in percentage ($m_{\%}$ [-]) at two consecutive time steps, the initial mass of the sample (m_0 [mg]) and the molar mass of the employed perovskite (MM_{LSMCr}=220,15 [g/mol]), the production rates are calculated second by second as:

$$r_{CO} = \frac{\frac{(m_{\%_t} - m_{\%_{t-1}}) \cdot m_0}{MM_{LSMCr}} \cdot V_{mol}}{m_0} \cdot 60\,{}^{s}/_{min} \cdot 10^{-6}\,{}^{mol}/_{\mu mol} \cdot 10^{3}\,{}^{ml}/_{l} \quad \left[{}^{ml}/_{min \cdot g}\right]$$

The obtained results in terms of peak rates present an understandable dependency with the oxidation temperature of the involved cycle, in fact higher temperature is related to higher peak rates. More importantly though, they are in good accordance with production rates of similar strontium and chromium doped lanthanum manganese perovskites [51].

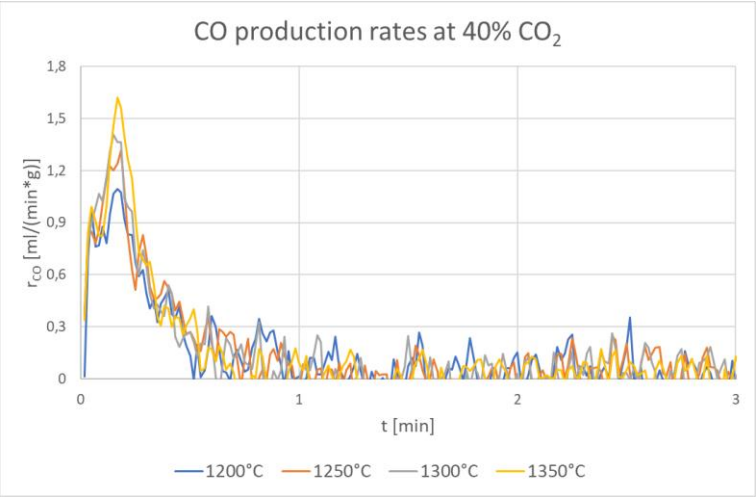

Fig.44 – Most of the evolved CO is produced during the first instants of the oxidation cycles.

Moving on, the experiments with oxidation phases at 30% and 50% of CO_2 are in line with the one performed at 40% of CO_2. By comparing the results of the three experiments in terms of extent of reaction α in the first minutes of reaction (Fig.45) it is possible to notice, for instance, that higher CO_2 concentration is directly related to higher overall mass gain. In other words, higher partial pressure of the reacting gas in the TGA leads to a higher reactivity of the material and more oxygen is captured in the crystalline lattice, a behaviour that is coherent with the already presented literature about LSMCr [50]. In terms of carbon monoxide productivity, cycles at 30% CO_2 concentration yielded 341,62 µmol/g on average, while cycles at 40% CO_2 concentration performed better with 487,87 µmol/g on average and cycles at 50% CO_2 concentration presented the best CO productivity, yielding 544,51 µmol/g on average. These values might seem way too high when compared for example to the ones displayed in Fig.9 and the fact that they were acqui-

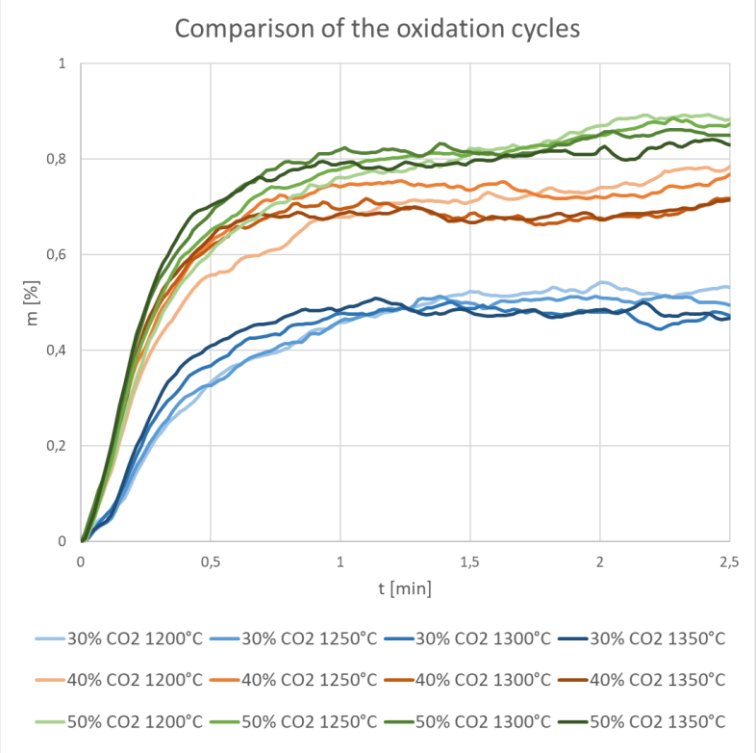

Fig.45 – Definitive results in terms of mass gained.

red as average of only four cycles with extremely small sample masses means that they have to be carefully assessed. Nevertheless, the cycles were performed at high temperatures and concentrations of the oxidizing agent with respect to other works, and moreover, it is not the first time that similar fuel yields are reported as a result of thermochemical redox cycles performed with lanthanum manganese perovskites [31]. On the other side, differently from the plotted extents of reaction, the reaction rate peaks seem to be similar in terms of magnitude between the three experiments (Fig.46), which indicates that the reaction kinetics is the same in all cases, and in turn means that the chosen mass flow rate does not affect the final data. There is a difference though, in the experiment at 30% of CO_2 the peak rate is reached a few seconds later with respect to the other two (generally speaking, experiments at 40% and 50% of CO_2 look much more similar, while the one at 30% of CO_2 presents some visible differences).

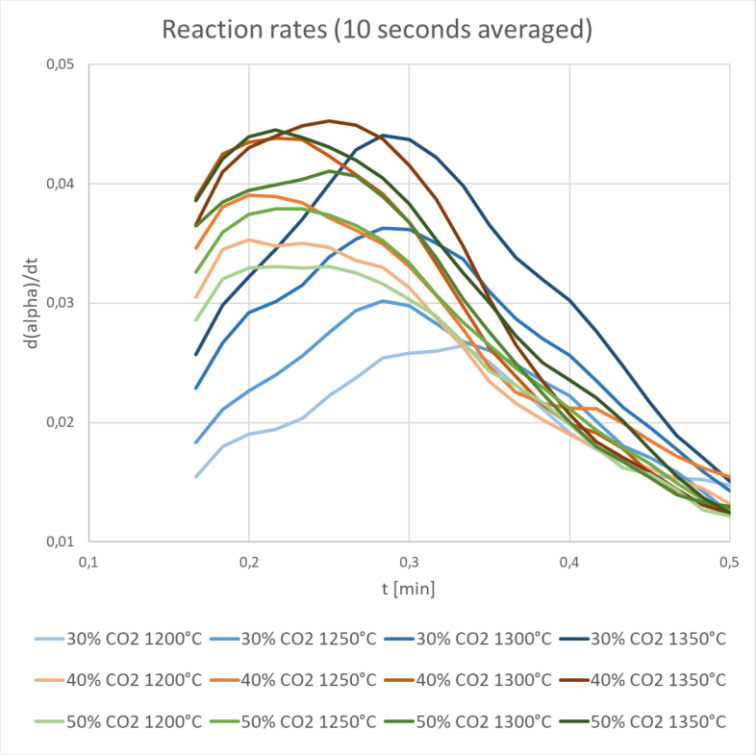

Fig.46 – Definitive results in terms of reaction rates.

4. Analysis of the oxidation kinetics

4.1. Theoretical framework

As far as reaction kinetics is concerned, the key parameter that must be studied is the reaction rate of a given chemical reaction. The reaction rate is in fact the measure of how fast the involved reaction is progressing in the given conditions, useful also to predict the potential future development of the process investigated. The literature in this field is starting to pile up in recent years, also based on a series of useful recommendations that are present and will be used as guidelines for this section of the present work [66]. If the quantity α is considered as the progress of a certain property during a particular process, its rate can be expressed with the time derivative of α, and in a simplified yet robust approach it can be considered to be the result of three different contributions:

$$\frac{d\alpha}{dt} = k(T) \cdot f(\alpha) \cdot h(p)$$

Trying to characterize each of the components of this formula, the effect of the pressure (p) can also be expressed as function of the concentration of the involved gases, and it usually takes a power-law form, where the exponent (m) is called the "reaction order". It is here relevant to report the fact that in many cases the contribution of pressure is neglected during kinetics studies. The contribution of temperature (T) is instead condensed in the so-called rate constant, and it is generally advised to parametrize it with the Arrhenius equation.

$$h(p) = p^m$$

$$k(T) = A \cdot \exp\left(-\frac{E_a}{R \cdot T}\right)$$

The characterizing parameters are the pre-exponential factor (A) and the activation energy (E_a). This quantity is usually not the activation energy of a single process or of the rate-determining step alone, but rather the combination of every single process composing the studied reaction, and it should therefore be considered as an apparent activation energy.

The discussion about the dependency from the extent of reaction α is more complex. This quantity represents the fraction of the overall change in a physical property, with respect to the entire variation of that property at the end of the reaction. For instance, if the selected property is the mass of the sample, as it will be the case for this specific work, α(t) is calculated as the ratio between the mass variation from the beginning of the reaction to the required time instant over the complete mass variation which is achieved at the end of the process. Such quantity can be described by proper reaction models (f(α)), which can be broadly classified in three typologies, as shown in Fig.47. Accelerating models are characterized by a continuously growing reaction rate, while decelerating models behave at the opposite and sigmoidal models present their peak rate at some point in the middle of the reaction. When performing the kinetic analysis, if the available data are difficult to interpretate, or if they are not well known, it is paramount to take advantage of methodologies capable of treating all the three presented model typologies.

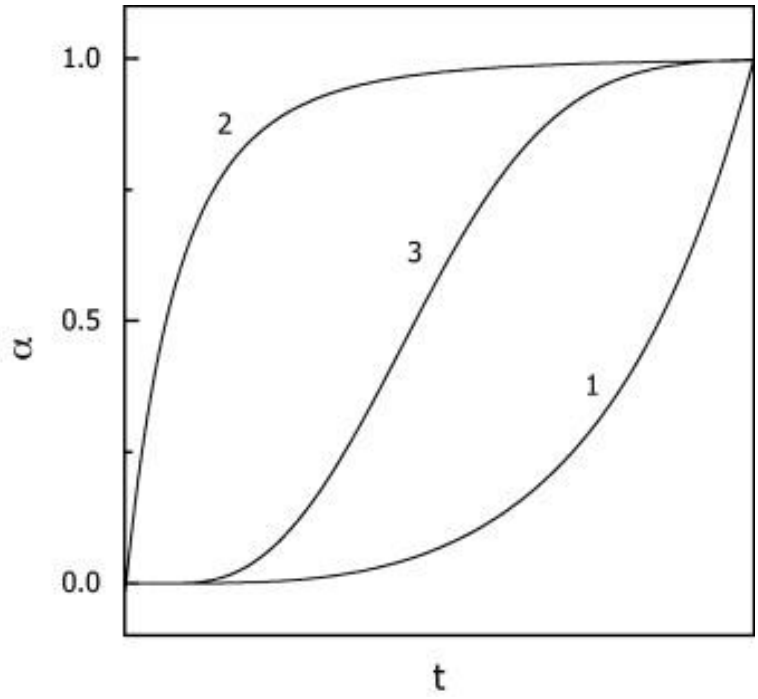

Fig.47 – In general a chemical reaction will follow either an accelerating (1), a decelerating (2) or a sigmoidal (3) behaviour. [64]

With specific reference to solid-state reactions, plenty of reaction models have been proposed and some of the most commonly employed are summarized in the table that is displayed in Fig.48. They are usually classified in four categories, depending on the kind of mechanistic effect that they better describe: [67]

- Reaction order-based models are the simplest in their phenomenological description of the solid-state reaction that is occurring: the process is considered to be homogeneous in the entire solid phase. The only aspects that affect the reaction are the concentration of the various species and the fraction of remaining reactant, which can be raised to different powers diversifying this class of models.
- Geometrical contracting models are a bit more complex. The reaction in this cases advances starting from the surface and shrinks towards the core of the solid phase (or, on the contrary, grows from the core towards the surface). The progress of the interface between reacted and unreacted material can either follow a 2D or 3D path, primarily depending on the initial shape of the grain that is reacting (cylindrical-like particles will follow the bidimensional model, spherical-like structures as well as cubic ones will follow the tridimensional model).
- Diffusion models are more complex conceptually, decisively moving away from homogeneous kinetics. It is in fact common in solid-state reactions that the needed reactants are not readily available at a certain reacting interface, placed in the bulk of the material: they might need to diffuse across a portion of it. In such cases, the rate of the occurring reaction decreases as much as the presence of layers of already reacted products increases, basically in such situation the reactants are located in separated portions of the material's lattice. Different diffusive mechanisms are considered as well, leading to multiple models.

- Nucleation and grain growth models ultimately describe the most complex mechanism of reaction between the described ones. In short, crystals of reactants can have fluctuating values of characteristic energy due to impurities or imperfections in the lattice like cracks, point defects, the presence of a dopant atom and more. In sites where the activation energy for the specific reaction is minimized, the product phase starts forming (nucleation) and from that point it continues in its process (grain or nuclei growth). The starting point of the nucleation process, as well as the speed of grain growth once nucleation takes place, can be function of different structural and kinetic parameters.

It is easy to verify this by simply plotting the characteristic expression of each model, but generally speaking power law models are of the accelerating typology, while Avrami-Erofeev models are sigmoidal. Diffusion, reaction order and geometrical contraction models instead show a decelerating trend.

model	differential form $f(\alpha) = 1/k\ d\alpha/dt$	integral form $g(\alpha) = kt$
	nucleation models	
power law (P2)	$2\alpha^{1/2}$	$\alpha^{1/2}$
power law (P3)	$3\alpha^{2/3}$	$\alpha^{1/3}$
power law (P4)	$4\alpha^{3/4}$	$\alpha^{1/4}$
Avrami−Erofeyev (A2)	$2(1-\alpha)[-\ln(1-\alpha)]^{1/2}$	$[-\ln(1-\alpha)]^{1/2}$
Avrami−Erofeyev (A3)	$3(1-\alpha)[-\ln(1-\alpha)]^{2/3}$	$[-\ln(1-\alpha)]^{1/3}$
Avrami−Erofeyev (A4)	$4(1-\alpha)[-\ln(1-\alpha)]^{3/4}$	$[-\ln(1-\alpha)]^{1/4}$
Prout−Tompkins (B1)	$\alpha(1-\alpha)$	$\ln[\alpha/(1-\alpha)] + c^a$
	geometrical contraction models	
contracting area (R2)	$2(1-\alpha)^{1/2}$	$1-(1-\alpha)^{1/2}$
contracting volume (R3)	$3(1-\alpha)^{2/3}$	$1-(1-\alpha)^{1/3}$
	diffusion models	
1-D diffusion (D1)	$1/(2\alpha)$	α^2
2-D diffusion (D2)	$-[1/\ln(1-\alpha)]$	$((1-\alpha)\ln(1-\alpha)) + \alpha$
3-D diffusion−Jander (D3)	$[3(1-\alpha)^{2/3}]/[2(1-(1-\alpha)^{1/3})]$	$(1-(1-\alpha)^{1/3})^2$
Ginstling−Brounshtein (D4)	$3/[2((1-\alpha)^{-1/3}-1)]$	$1-(2/3)\alpha-(1-\alpha)^{2/3}$
	reaction-order models	
zero-order (F0/R1)	1	α
first-order (F1)	$(1-\alpha)$	$-\ln(1-\alpha)$
second-order (F2)	$(1-\alpha)^2$	$[1/(1-\alpha)]-1$
third-order (F3)	$(1-\alpha)^3$	$(1/2)[(1-\alpha)^{-2}-1]$

Fig.48 – Table containing some of the models that are used to describe solid-state reactions. This table does not claim To be comprehensive, but at least a couple of models for each of the main categories are present. [67]

When dealing with kinetic computations it is possible to follow various approaches. The most straightforward one is to investigate the behaviour of the apparent activation energy of the studied reaction as function of the extent of reaction. More in-depth analysis involves instead the complete characterization of the equation for the reaction rate, individuating the values for the pre-exponential factor (A), the reaction order (m), and more importantly the reaction model involved (f(α)). If the first approach is considered enough, then the correct decision is to rely on an isoconversional method. Such procedures are based on the principle that, if the contribution of pressure is neglected as it often happens, at constant extent of conversion (α), the reaction rate only depends on the temperature. This assumption is made possible by using the general equation of the reaction rate, calculating the logarithm at both sides, and then taking the derivative:

$$\left|\frac{d\left(\ln\left(\frac{d\alpha}{dt}\right)\right)}{dt}\right|_{\alpha} = \left|\frac{d(\ln(k(T)))}{dt}\right|_{\alpha} + \left|\frac{d(\ln(f(\alpha)))}{dt}\right|_{\alpha}$$

When isoconversional values are considered the last term of the presented equation is equal to zero, which indeed means that the typology of reaction model does not impact the study anymore, and with proper methodologies (one of them will be described in subsection 4.2.1) investigation of the apparent activation energy is made possible. It is in fact important to remember that in the presented formula the activation energy is present, hidden inside the expression of the rate constant k(T). A more thorough investigation of the reaction kinetics, eventually retrieving the values of each of the parameters contained in the generic equation for the reaction rate, can be carried out with model fitting procedures instead. The idea is to select one of the available reaction models and then minimizing the differences between the experimental data and the ones calculated through the model itself. The paramount step in these procedures is the identification of the proper model, a choice that can be based on the type of reaction being studied, the indication of a potential multi-step reaction, the behaviour of the apparent activation energy with respect to α, the acceleratory/decelerator/sigmoidal nature of the experimental data and their comparison with the typical profile shapes of the various models. [66] In concluding this theoretical introduction it is important to remember that the validation of the obtained results, especially when model fitting is performed, is as relevant as the fitting procedure itself. This is typically done by testing the model's prowess in predicting experimental kinetic curves.

Some conclusive remarks are presented here, to provide better context. This specific work deals with the kinetic analysis of a powder reacting with a gaseous flow. This interaction can be treated as a porous media in which a gas is flowing, and possible kinetic bottlenecks in such reactions can typically be diffusion through the material's pores, redox reactions at the material's surface or chemical diffusion into grains of the solid towards the bulk. [68] When gases are the involved fluids, the diffusion through the material pores is normally not a problem. The reactivity at the surface can instead be investigated by performing a sudden variation of the oxygen pressure, leading to mass relaxation or conductivity relaxation studies. The latter works because the creation of oxygen vacancies or on the contrary the incorporation of oxygen atoms in the lattice (thus the creation of "electron holes") can vary the conductivity of the material. Chemical diffusion inside the solid can be investigated by monitoring the structure of the material, and too low oxidation temperatures have a detrimental effect on this transport phenomenon. Interestingly, even when performing a detailed kinetic study, the usage of conductivity relaxation data or chemical diffusivity data (indirect methods) can be chosen in place of gas evolution or mass variation data (direct methods) for the calculation of the kinetic parameters. [49] More specifically, it has been reported that, concerning strontium-doped lanthanum manganese perovskites at temperatures relevant for thermochemical cycles, bulk diffusion is unlikely to be the rate-limiting step: surface reaction is in fact the most probable responsible. [56]

4.2. Kinetic study

Now, with the available oxidation profiles, a kinetic study will be conducted, mainly based on the extent of reaction profiles describing the mass increase and on the reaction rates which have been presented in Fig.45 and Fig.46. The aim of this study is to describe in detail the chemical processes involved in terms of activation energy (also as function of the extent of reaction α in

case it will not be constant) and reaction mechanisms which can for example follow diffusion, nucleation or other forms, while keeping in mind the dependency on the two main variable parameters, namely temperature and pressure. It is hereby worth it to mention that data has been retrieved following as much as possible the available recommendations for this kind of studies, which are basically to make sure that the sample and experimental conditions are chosen in a way that their effect on the obtained kinetic data is minimized. [64] Some indications of this general approach in this work can be found for example in subsection 3.3.6 or in the fact that a wide enough range with more than three different temperatures has been selected. It is worth it here to acknowledge the limitations of a real reactor. Its capability to present homogeneous atmosphere conditions, as clean as possible temperature profiles, efficient absorption of radiated heat and many more features to make the process as ideal as possible have an impact on the kinetics too. Another important clarification that must be done before starting the analysis is about the fact that, for sake of simplicity, in the following procedures the kinetics of the studied phenomena will always be treated as described by a single-step formulation, despite some trends (which were highlighted for instance in subsection 3.3.5) suggesting that in the specific case a more complex kinetic model could be appropriate.

4.2.1. Isoconversional method

The first step of the kinetic analysis consisted in the application of an isoconversional method. This study was conducted on the basis of another work that was found in the literature, nevertheless some variations were made in order to better adapt the analysis to the available experimental data. [69] Starting from the oxidation profiles for LSMCr in the temperature range from 1200°C to 1350°C, and for the three studied values of CO_2 concentration in argon (30%, 40% and 50%), the goal of this analysis was to obtain a value for the activation energy of the material, as well as to study its behaviour while the reaction progressed, that is, its dependency from the extent of reaction. The starting point for the proposed investigation was once again the general equation for the reaction rate:

$$\frac{d\alpha}{dt} = Aexp\left(-\frac{E_a}{RT}\right) \cdot f(\alpha) \cdot c^m$$

Notice how this time the concentration of the oxidizing agent is employed instead of its partial pressure. Both options are viable as already mentioned, but in this formulation it is fundamental to notice that the values of the concentration at the inlet are valid in normal conditions. Once the gases are heated up in the reaction chamber of the TGA though, the following equation (simply based on the ideal gas law) must be employed to calculate the corrected values of CO_2 concentration, starting from the values of CO_2 partial pressure which are instead constant:

$$c_{CO_2} = \frac{n_{CO_2}}{V} = \frac{pp_{CO_2}}{RT} \quad \left[{mol}/{m^3}\right]$$

Since the effect of the concentration was not neglected in this formulation it was this time necessary to perform a preliminary step before beginning the isoconversional procedure, which consisted in an estimation of the reaction order (i.e. of the exponent m, the only parameter that tunes the CO_2 concentration's effect on the reaction kinetics in this simplified approach). The

estimation was performed by extracting the logarithm of both terms of the general equation for the rate of reaction, and then by applying the basic properties of logarithms the reaction order can be represented as the slope of a properly designed plot:

$$\ln\left(\left|\frac{d\alpha}{dt}\right|_{max}\right) = m \cdot \ln(c_{CO_2}) + \ln\left(Aexp\left(-\frac{E_a}{RT}\right) \cdot f(\alpha)\right)$$

In particular, in the reference work the values of the reaction order (m) were obtained by plotting the values of CO_2 concentration on the x-axis and the values of the initial slope of the mass change on the y-axis. This was done first of all because the mass variation is proportional to the extent of reaction variation for time instants that tend to zero, and secondly because the data that were used there actually present a decelerating profile for α, therefore the initial slope is also the point in which the rates are maximum. In this work the experimental data are quite different, so trying to comply as much as possible to the reference it was decided to plot the maximum value of reaction rate on the y axis (Fig.49), the only difference being that here that value is not located at the initial time instant, rather at some seconds after the beginning of the oxidation phase.

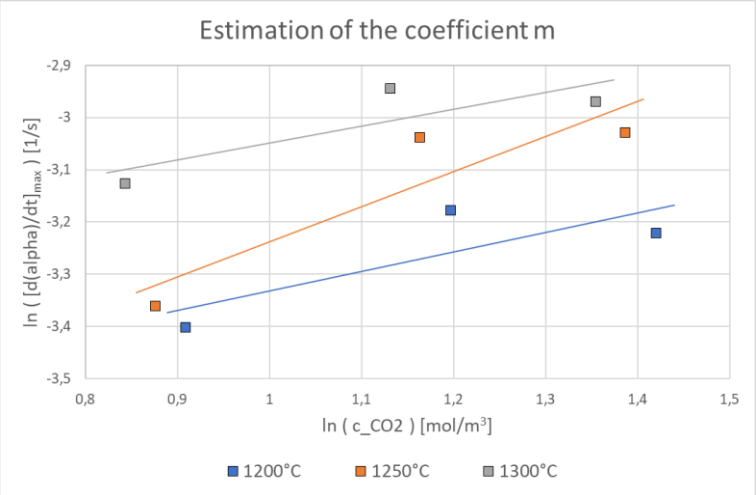

Fig.49 – The slope of the straight lines gives the desired coefficient. Only three trends are present, the one at 1350°C has been discarded.

The obtained results had three comparable slopes, while the curve referring to the values at 1350°C presented an unexpected decreasing trend. It was not possible to explain such a behaviour with certainty, what might happen is that at such high temperatures the reaction could be limited by some other phenomenon. The fact that at different temperatures the rate limiting factor for a reaction can be different is well known and reported in literature [69]. Only the three reasonable trends were therefore considered in the estimation of the reaction order m, which turned out to be equal to 0,456±0,154. It was then time to move to the actual isoconversional procedure, which was applied by first of all shifting the contribution due to CO_2 concentration to the left side of the general equation for the reaction rate. The logarithm of both members was then calculated and, by recalling the Arrhenius expression for the rate constant k(T), the following formulation was reached:

$$\ln\left(c^{-m} \cdot \left|\frac{d\alpha}{dt}\right|_{\alpha}\right) = -\frac{E_a}{RT} + \ln(A \cdot |f(\alpha)|_{\alpha})$$

A plot of the entire left member of the equation on the y-axis against 1/(RT) on the x-axis was supposed to provide the desired value of the apparent activation energy, but with opposite sign. All of this was of course to be performed at constant values of the conversion extent (α), but the oscillatory nature of the experimental results made it difficult to precisely evaluate the values of the reaction rate (the derivative of α) at standardized values of the extent of reaction. For this reason, in Fig.50 a simple, discretized version of alpha is presented, only composed of 19 points, and obtained by simply evaluating the time instants at which the extent of reaction reached relevant values, with a discretization step of 0,05.

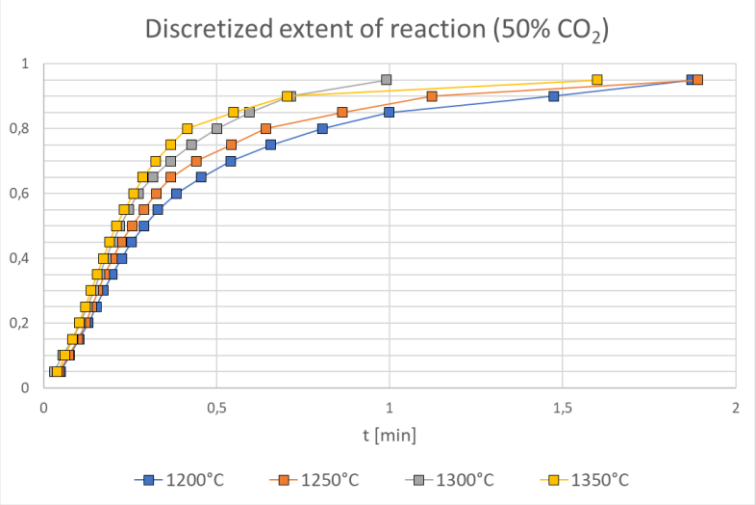

Fig.50 – Extent of reaction α evaluated at isoconversional values, at equally spaced steps of α=0,05.

This form of α was then utilized to calculate the desired values of the time derivative of alpha at standard values: a numerical scheme using second order accurate central differences was employed, while in the extreme points one-side differences were instead used. With the newly calculated values for the reaction rate, it was finally time to construct the abovementioned plot, which is shown in Fig.51 for the case at 50% of CO_2. The one thousand multiplicative coefficient that is found on the x-axis is there to allow for better visualization of the data. Notice that, with the goal of making it easier to read the diagram, only alpha values with 0,1 discretization step are displayed in the plot, and moreover the extreme values (α =0,1 and α =0,9) are neglected. This approach is suggested in literature [70], but it can also be briefly explained as follows: in the first case for α =0,1 not enough time passed from the beginning of the experiment to obtain reasonable accuracy, while in the second case it was almost impossible to select a value for the time relative to α=0,9 since the experimental profiles in this range are characterized by a drastically oscillatory behaviour. It was finally possible to obtain a value for the activation energy, but first two more diagrams similar to Fig.51 were generated for CO_2 concentrations at 30% and 40% too, so that the values of the apparent activation energy could be compared. Cycles at CO_2 concentration equal to 30% presented an apparent activation energy equal to 53,1±14,8 kJ/mol, while cycles at 40% CO_2 concentration had E_a=33,1±14,2 kJ/mol and finally cycles at 50% CO_2 concentration were characterized by E_a=35,3±13,7 kJ/mol. The three results are quite different, but still compatible within their errors, an average value of the apparent activation energy can therefore be calculated, and it results to be 40,5 kJ/mol.

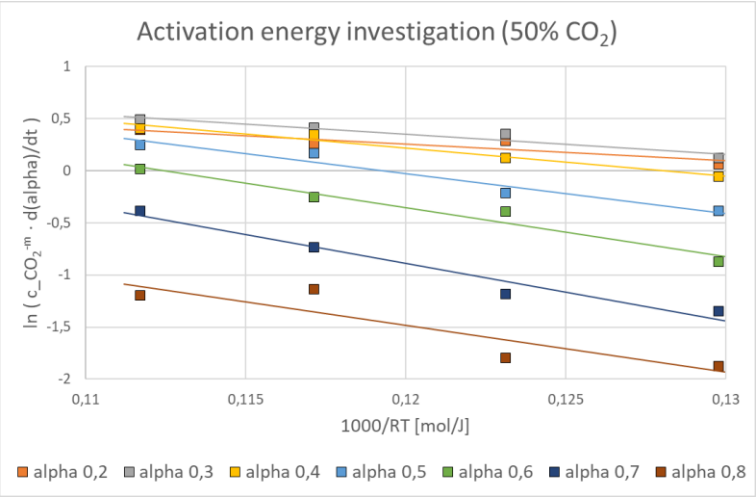

Fig.51 – The negative slope of the displayed straight lines yields E_a.

The first comment that can be done is that, even though the three values are compatible within their error ranges, a quite substantial difference is present between the first value of the activation energy and the other two. Values of activation energy in the order of magnitude of tenths of kJ/mol are reasonable, unfortunately it has not been possible to find in literature a value to be compared with these ones, once again proving the lack of studies about LSMCr. Another point that it is key to assess is the fact that the values of the standard deviations are very high, which can be explained by Fig.52: the apparent activation energy largely changes depending on the extent of reaction. It can first of all be noticed that lower partial pressure of CO_2 is generally translated in higher activation energy: this can be an actually real effect, but it could also indicate that a lower flow rate of the oxidizing agent introduces some sort of kinetic limitation. The fact that the kinetics is favoured (by low activation energy) at low values of α means that once the reaction takes place it will easily go on for a while, but then reaching the final oxidized state needs more effort, basically as oxygen incorporation proceeds the oxidation reaction is increasingly unfavoured, a trend that is actually not new in literature [24].

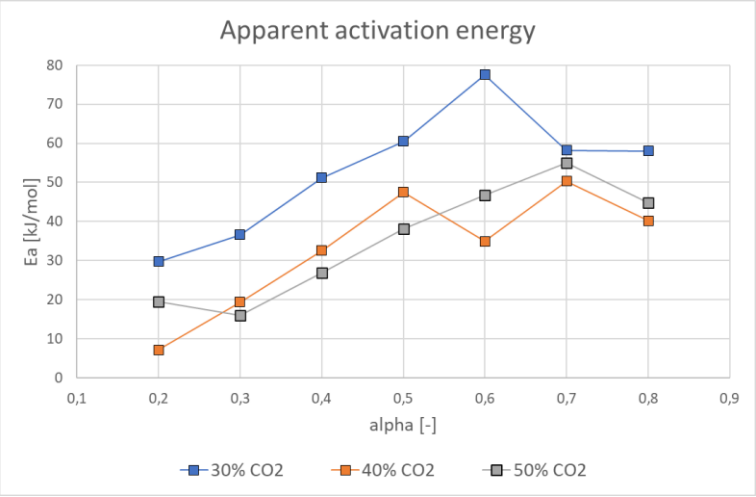

Fig.52 – The activation energy strongly depends on the extent of reaction.

Such a behaviour could suggest that the kinetics of the process is composed of more than one relevant step, otherwise the activation energy would have been approximately constant

throughout the entire range of α that has been investigated. The topic of multi-step kinetics is a quite vast and complex one, and it will not be deepened within this work, but support literature on this matter is nonetheless available. [70] Interestingly enough, there already is some evidence in literature about the fact that lanthanum manganese perovskites might be characterized by multi-step kinetics [71].

4.2.2. Model fitting method

The model fitting procedure was developed based on some literature reference too. [72] During preliminary tests with model fitting, the utilization of raw data for the extent of reaction (α) and the reaction rate (dα/dt) proved to be complex, because of the oscillatory nature of the data retrieved from TGA-based experimentation. For this reason, it was decided to smoothen the trends by employing the experimental data averaged over a time span of 10 seconds. Recalling some useful information, the goal of this study is of course to identify which kind of solid-state reaction is occurring during the oxidation of LSMCr, and to describe it as conveniently as possible with a numeric model. In order to do so, it is first and foremost important to select a proper model for the fitting of the data. It was possible to identify which class of models was the most promising by addressing the experimental profiles of the data. In particular, the plots for α in time (Fig.45), present a trend that, at first glance, could seem to either be decelerating or sigmoidal. Focusing on the first seconds, the sigmoidal trend looks like the most probable option, since the curves start with relatively low slopes, then slightly accelerate and eventually decelerate again before a long final phase in which the mass gain is extremely slow. Much more clearly, when looking at the reaction rate trends (Fig.46), it is evident how the peak rates are not plotted at the first second of the reaction, rather after around 15 seconds, proving in this way the sigmoidal hypothesis. It was therefore decided to concentrate the following study on models that well describe sigmoidal trends, that is, Avrami-Erofeev models. A list of the most relevant models of this typology that have been found in the available literature [72] is presented in the following table (Tab.3).

Model	Differential form f(α)	Integral form g(α)
AE0.5	$^1/_2\,(1-\alpha)(-\ln(1-\alpha))^{-1}$	$(-\ln(1-\alpha))^2$
AE1	$(1-\alpha)$	$-\ln(1-\alpha)$
AE1.5	$^3/_2\,(1-\alpha)(-\ln(1-\alpha))^{1/3}$	$(-\ln(1-\alpha))^{2/3}$
AE2	$2(1-\alpha)(-\ln(1-\alpha))^{1/2}$	$(-\ln(1-\alpha))^{1/2}$
AE3	$3(1-\alpha)(-\ln(1-\alpha))^{2/3}$	$(-\ln(1-\alpha))^{1/3}$
AE4	$4(1-\alpha)(-\ln(1-\alpha))^{3/4}$	$(-\ln(1-\alpha))^{1/4}$
AEn	$n(1-\alpha)(-\ln(1-\alpha))^{(n-1)/n}$	$(-\ln(1-\alpha))^{1/n}$

Tab.3 – List of the most common Avrami-Erofeev models in literature. [72]

The last of the presented models, i.e. the n-order Avrami-Erofeev model (AEn) is characterized by an additional parameter, which can be easily calculated on the basis of the experimental data of the specific oxidation cycle that is being studied. It is first of all necessary to locate the value of the extent of reaction in correspondence of the maximum peak rate (α_{max}), and at this point the parameter "n" can be evaluated with the following formula, obtaining a different value for each of the involved oxidation cycles:

$$n = \frac{1}{1 + \ln(1 - \alpha_{max})}$$

Once the interesting models have been selected, before starting with the analysis it is worth it to briefly explain how the numerical curves, obtained thanks to the various models, will be fitted to the experimental data, and in which way a model will be considered better or worse than another. The approach in this sense has been very simple: the relevant parameter that has been chosen is the minimum value of the residual sum of squares (RSS), also known as the squared estimate of errors. As straightforward as the name tells, this parameter consists of the sum of the squares of all the residuals, which are the deviation of the numerical data from the experimental data, and a small value of it indicates that a numerical prediction is well capable of fitting experimental data. As suggested by the reference work that has been followed for this analysis [72], the calculation of the residual sum of squares has been done for two quantities: the extent of reaction as function of time, and the reaction rate as function of the extent of reaction. Taking the first example, the residual sum of squares can be expressed as:

$$RSS = \sum_{t=1}^{t_{end}} \left(\alpha_{exp,t} - \alpha_{num,t}\right)^2$$

The starting point for the model fitting procedure was, as usual, the general equation for the rate of reaction, comprising the three relevant contributions. This time though, the focus was put on the reaction model, that is, on the dependency of the reaction rate on the extent of reaction (represented by f(α)) so the usual equation has been appropriately rearranged to put this term in particular evidence:

$$\frac{d\alpha}{dt} = k(T) \cdot f(\alpha) \cdot h(p)$$

$$\frac{d\alpha}{f(\alpha)} = \big(k(T) \cdot h(p)\big)dt = K \cdot dt$$

At this point it is possible to introduce the integral expressions of the various reaction models g(α), which have already been displayed in Tab.3, and can be expressed as follows:

$$g(\alpha) = \int_0^{\alpha} \frac{1}{f(\alpha)} d\alpha = K \cdot t$$

This last equation states that the complex g(α) functions related to the various models can ultimately be approximated by a theoretical straight line where the only parameter is K. The model fitting procedure in fact involves the evaluation of the various $g(\alpha_{exp})$ with the experimental values of the extent of reaction as the argument, with the aim of fitting the resulting curves to a straight line. By doing so the values of K for each oxidation cycle and each of the involved models will be obtained, so that the straight trends $g(\alpha_{num})$=Kt can be calculated. At this point it is

sufficient to invert the formulations of g(α) contained in Tab.3 and the desired values of numerical extent of reaction in time will eventually be obtained. It is then straightforward to compute the numerical reaction rates by calculating the time derivatives of the numerical α with the usual methodology of subtracting two consecutive values of α and dividing by the time interval (which is once again 1 second for all cases). With the numerical data, the RSS will finally be computed, and the most precise model will be selected.

The results of the explained procedure are be presented here, but before an additional step was required. In particular, it was clear from the beginning that the various trends of the integral reaction models with the experimental α as the argument (Fig.52) would have been complicated to fit with a straight line, at least over their entire domain. For this reason, as it is common to do, it was decided to plot their trends as function of α with the goal of selecting only a certain range of the extent of reaction over which to perform the fitting to find the parameter K. Looking at the plots in Fig.53, it was arbitrarily decided to only consider $\alpha<0,85$ in order to fit curves that were at least resembling a straight line. However, while only partial data has been used for the evaluation of the parameter K, the kinetic study will still be carried out on the complete dataset, also including $\alpha>0,85$.

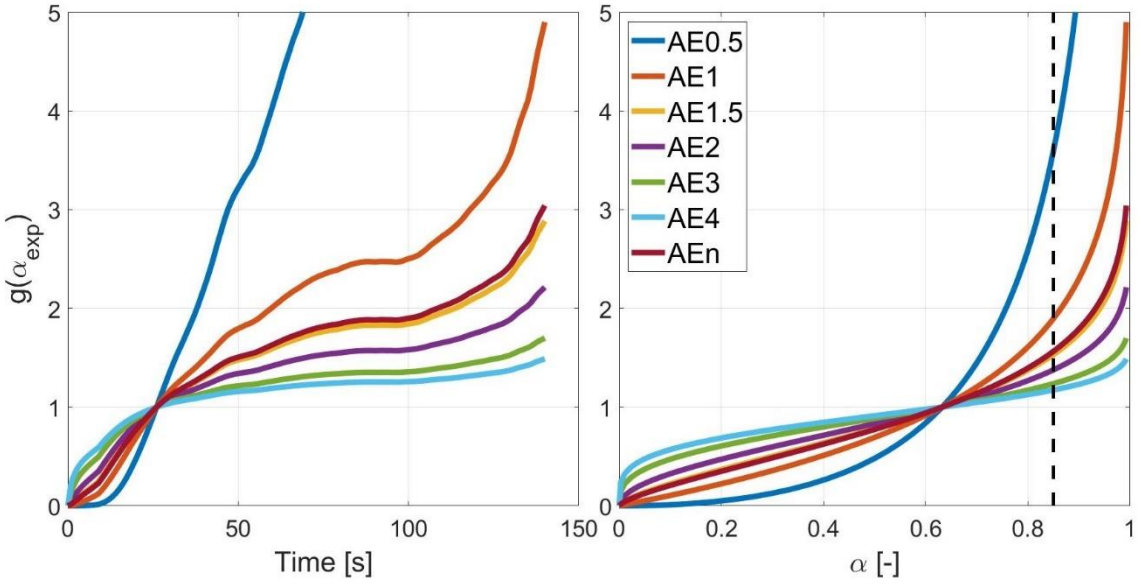

Fig.53 – Integral functions with the experimental α as the argument plotted as function of time (left) and of α itself (right). The dashed vertical line represents the α=0,85 threshold.

The fitting of the first portion of $g(\alpha_{exp})$ curves to straight lines was then easily performed. It was also decided to take advantage of this step to preliminarily exclude some reaction models, so that the following passages could be done only on the most promising ones. In particular, since the mentioned fitting procedure between the $g(\alpha_{exp})$ and the straight lines was carried out in an Excel sheet, it was possible to exploit the fact that Excel can easily show the R^2 of a series of points with respect to a trendline. In statistics, R^2 is called coefficient of determination, and it represents the bond between the data that must be fit and the fitting model that is used: the closer R^2 is to 1, the better the correlation. In Tab.4 the results for every oxidation cycle in terms of the resulting R^2 for each of the Avrami-Erofeev models are presented. On the basis of such results, only AE1, AE1.5, AE2 and AEn models were further investigated in the following.

\	30% 1200°C	30% 1250°C	30% 1300°C	30% 1350°C	40% 1200°C	40% 1250°C	40% 1300°C	40% 1350°C	50% 1200°C	50% 1250°C	50% 1300°C	50% 1350°C
AE0.5												
AE1												
AE1.5												
AE2												
AE3												
AE4												
AEn												

Tab.4 – A preliminary selection of the most promising Avrami-Erofeev models was made on the basis of the R^2 calculated between the theoretical line and the $g(\alpha_{exp})$. In this table a red cell is related to $R^2<0,97$ representing a quite bad fit, a yellow cell is related to $0,97<R^2<0,99$ and a green cell is related to $R^2>0,99$ representing a very good fit.

The described procedure was then followed with respect to the only four models that were just selected, and the results for one arbitrarily selected oxidation cycle are shown in Fig.54. As mentioned, the reference work that was followed to conduct this analysis [72] suggested to investigate the trends of extent of reaction (α) as function of time and reaction rate (dα/dt) as function of the extent of reaction. The results are quite satisfying in the first case, even though inevitably the final portion of the curves could not be precisely modelled, while in the second diagram the theoretical trends are quite far from the experimental data. This can once again be explained with the concluding portion of the oxidation reaction trends, presenting a slow and irregular increase that was not even considered when fitting for the K parameter (the fitting was in fact stopped at $\alpha<0,85$). Moreover, the oscillatory behaviour of the curves for high values of α leads to a strange concentration of points in the bottom right corner of the right plot, which in itself drives the numerical model-related trends too low and away from an accurate representation of the first portion of the oxidative process, which is the most relevant one.

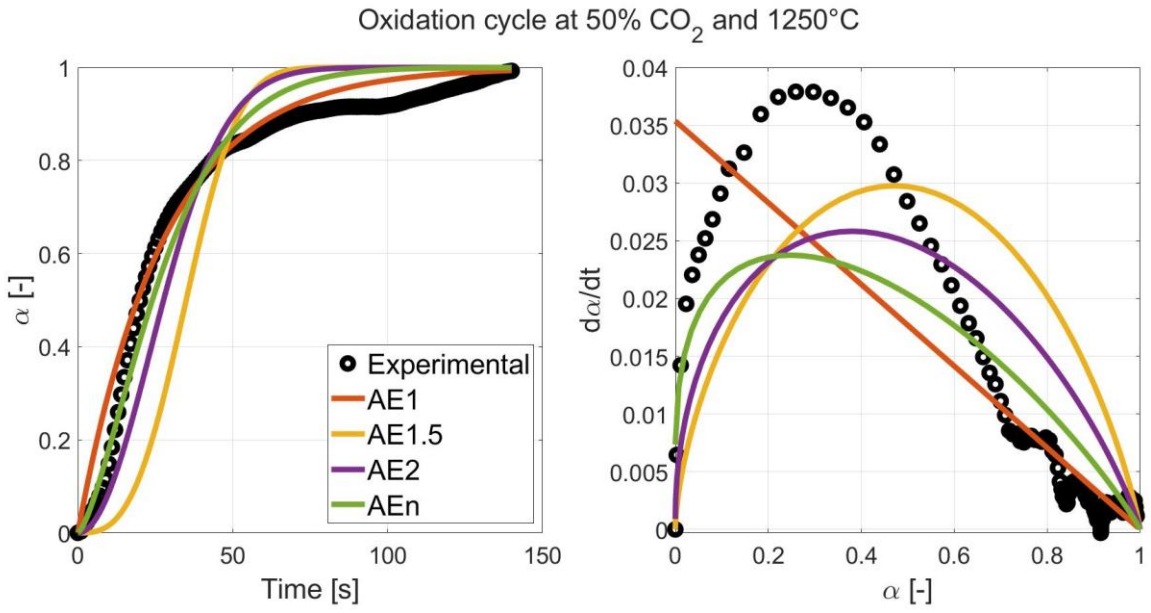

Fig.54 – Here the results of the model fitting procedure can be visually appreciated. This typology of diagram was obtained for each studied oxidation cycle, the complete set of results is available in Appendix C.

That being said, the results in terms of root sum of squares were investigated, in order to finally individuate which model was the best fitting one to the experimental data. In Tab.5 the model showing the lowest value of RSS for each studied cycle is reported, for each of the two suggested dependencies. The results clearly state that the most suitable model for the description of the TGA collected data is an Avrami-Erofeev model of order n. This result is not obvious of course, but is not surprising either: presenting one additional parameter with respect to the other studied models, the n-order Avrami-Erofeev model is capable of better tuning itself on the specific features of the data that need to be approximated.

\	30% 1200°C	30% 1250°C	30% 1300°C	30% 1350°C	40% 1200°C	40% 1250°C	40% 1300°C	40% 1350°C	50% 1200°C	50% 1250°C	50% 1300°C	50% 1350°C
α, t	AE1	AE1	AEn	AEn	AE1	AEn	AEn	AEn	AE1	AEn	AEn	AEn
$\frac{d\alpha}{dt}, \alpha$	AE1	AEn	AEn	AE2	AEn	AEn	AEn	AEn	AEn	AEn	AEn	AEn

Tab.5 – For each oxidation cycle the model presenting the lowest RSS for both the investigated diagrams is reported here. The Avrami-Erofeev model of order n results to be the best in most of the evaluated conditions.

As a conclusive remark, it is worth it to once again remember the fact that the initial fitting to find the parameter K was arbitrarily only performed for $\alpha<0,85$. This choice hinders the model's capabilities of accurately describing what happens for high values of the extent of reaction, therefore in the final part of the reaction itself. This choice was considered to be substantially forced by the typology of the available data: fitting the entire range with a straight line was not considered to be optimal, given the trends of the $g(\alpha_{exp})$ functions displayed in Fig.53. Moreover, it is important to remember what was obtained in subsection 4.2.1, i.e. a strong dependency of the apparent activation energy on the parameter α, suggesting that a multi-step kinetics description could have been the correct option in this case. The choice of performing a single-step model fitting was done just to avoid the complexities of multi-step modelling. Nevertheless, performing single step modelling on a selected range of α when the reaction is believed to present multi-step kinetics is an effective approach, that has also been discussed in literature. [49] Plenty of studies, in fact, present their results in terms of reaction models only valid in a certain range of α, and indeed in this specific case the AEn model appears to superimpose quite well to the experimental data, at least in the initial stages of the oxidation reaction.

5. Conclusions

In this work the behaviour of an innovative perovskite with composition $La_{0.6}Sr_{0.4}Mn_{0.6}Cr_{0.4}O_3$ was studied for CO_2 splitting in two-step thermochemical redox cycles. Thermogravimetric analysis experiments highlighted the material's capability to reduce under high temperatures (T_{red}=1350°C) and subsequently oxidize in presence of CO_2, returning back to its initial state and correspondingly leading to the production of CO. Proper experimental conditions have been discussed, with tailored experiments aimed at assessing suitable sample masses and volumetric flow rates (such to overcome mass transfer limitations), as well as the most relevant ranges of CO_2 concentration and oxidation temperature to be explored. LSMCr samples displayed good cyclability and reasonably shaped oxidation trends, hence more comprehensive experiments have been carried out. The investigated conditions involved 30% to 50% CO_2 concentrations in the feed and 1200°C to 1350°C oxidation temperatures, thereby testing isothermal operation too, coherently with the available literature on this class of perovskites. The retrieved data were then used to conduct a kinetic analysis of the oxidation reaction. First an isoconversional method allowed to estimate the apparent activation energy, which resulted to increase along the reaction process. This outcome suggests that LSMCr oxidation would likely need to be treated as a multi-step kinetic process, however, for sake of simplicity, only a single-step model fitting procedure was subsequently applied. Considering the characteristics of the TGA experimental data, Avrami-Erofeev models (which are typically related to nucleation and grain growth reaction mechanisms) were expected to better describe the involved process for values of the extent of reaction below 0,85. Models belonging to this class were fitted to the experimental data, in terms of extent of reaction (α) as function of time as well as reaction rate ($d\alpha/dt$) as function of the extent of reaction itself, accordingly with the methodologies reported in literature. Amongst all of them, the n-order Avrami-Erofeev model (AEn), presenting the lower RSS between numerical predictions and experimental data, was considered the one that better describes the oxidation kinetics of LSMCr, at least in the α<0,85 range.

Future expansion of this work would be advisable with the goal to obtain a more comprehensive knowledge on the LSMCr thermodynamic and kinetic performances. The first suggestion that could be discussed concerns the experimental setup. In this work the estimation of CO productivity was based on the sample mass variation, considering all the gained mass as oxygen atoms stripped from CO_2 molecules and reabsorbed into the lattice of the perovskite. A much more precise evaluation of the evolved CO, as well as a much less oscillatory dataset, could be obtained by coupling the TGA with a mass spectrometer. In addition, the implementation of water splitting would be a further point of interest, but it was not possible to investigate it due to instrumental limitations. A properly designed reactor to be employed in place of the TGA could allow for such improvement, while also relaxing the limitations in terms of maximum mass flow rate that were mentioned in this work. From the point of view of the kinetic analysis, the investigation of different reaction models (i.e. model typologies other than Avrami-Erofeev ones) is not expected to provide better results with respect to the ones used. A potential improvement could nevertheless be to carry out the model fitting procedure to a deeper extent, trying to obtain benchmark values for the kinetic parameters that describe solid-state kinetics (namely the reaction order m and the pre-exponential factor A, as well as the activation energy E_a, which could

be compared with the values obtained from the isoconversional method). The most relevant further development in this sense would however be to perform a multi-step kinetic study, as it was highlighted that the oxidation reaction for LSMCr possibly consists in a multi-step process. Most of these described improvements are already under investigation, while in a more long-term perspective the validation of the kinetic results in a scaled-up reactor for syngas production through thermochemical cycles would be the ultimate goal.

Appendix A

The LSMCr sample was tested with X-ray diffraction spectroscopy and the results are presented in the following figure. On the y axis the intensity of the peaks is plotted, which can be expressed in arbitrary units and therefore no ticks are present, while the x axis describes the diffraction angle theta in degrees. This technique is widely used in material's characterization since it provides useful information on the crystalline structure, and it does so in a non-invasive way. The obtained results here can be compared with ease to the ones obtained by studies about similar perovskites [46] [51] [52]. This similarity confirms the fact that the studied materials share the same crystalline structure, that is, a rhombohedral structure of the R–3c space.

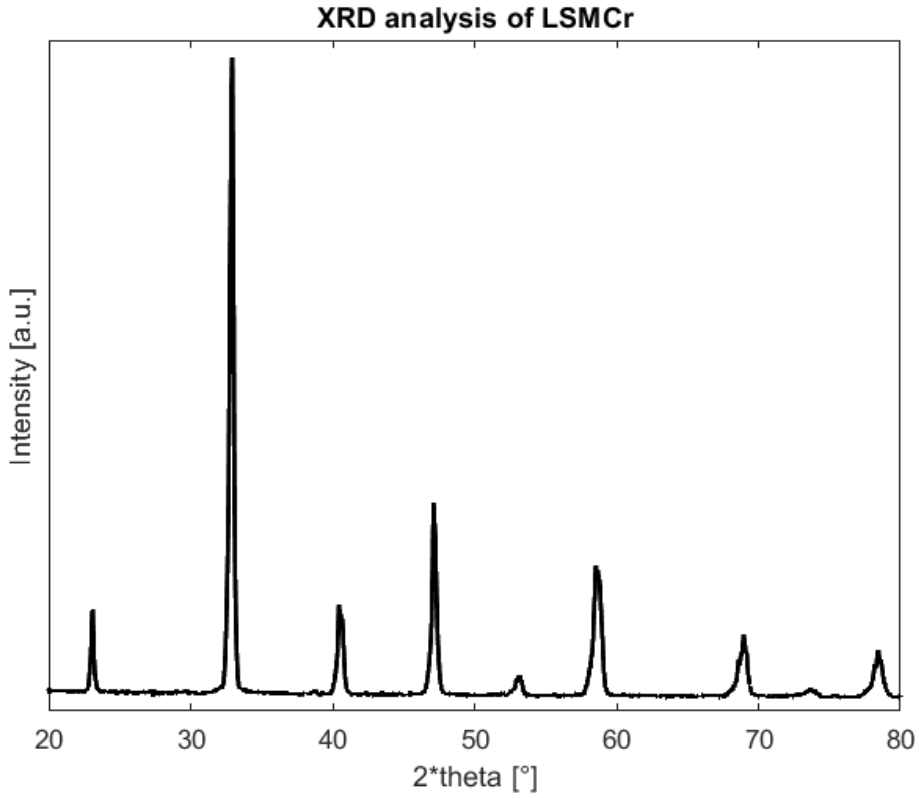

Appendix B

The complete results of the definitive experiments for CO_2 concentration equal to 30% (the first four diagrams) and 50% (the other four) are reported. They were not presented in the main body because of their substantial similarity with the case at 40%, which was arbitrarily chosen as the reference one.

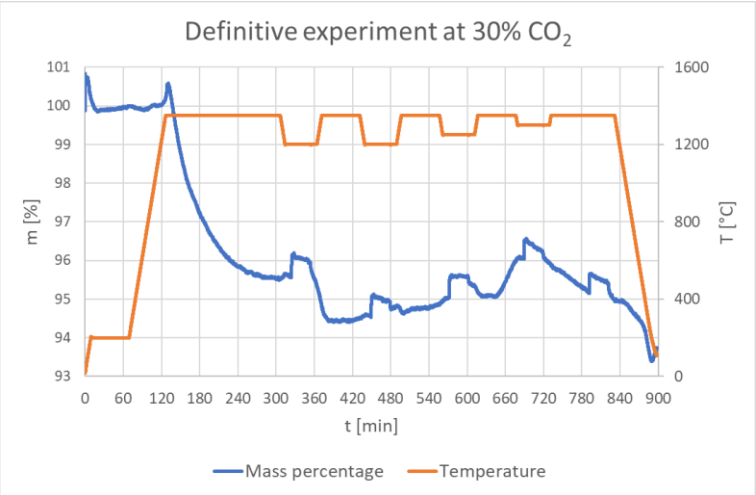

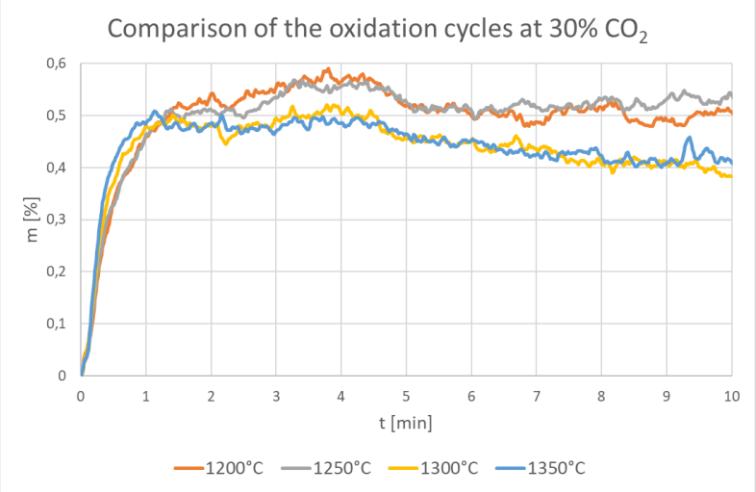

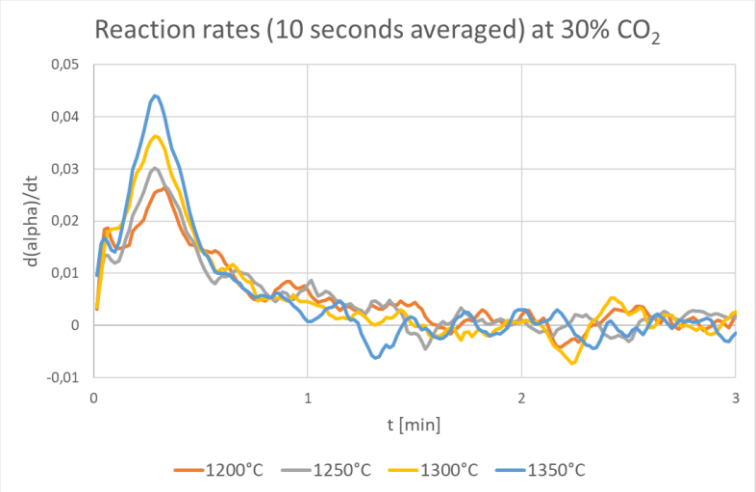

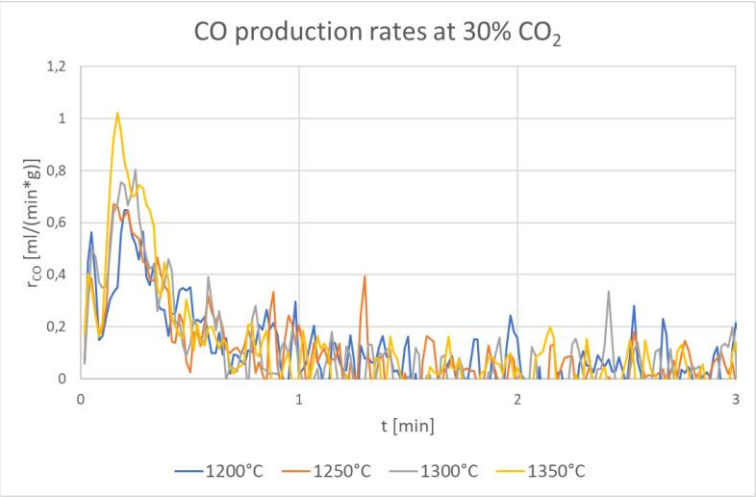
CO production rates at 30% CO2
1,2
1
0,8
0,6
0,4
0,2
0
rCO [ml/(min*g)]
0
1
2
3
t [min]
1200°C
1250°C
1300°C
1350°C

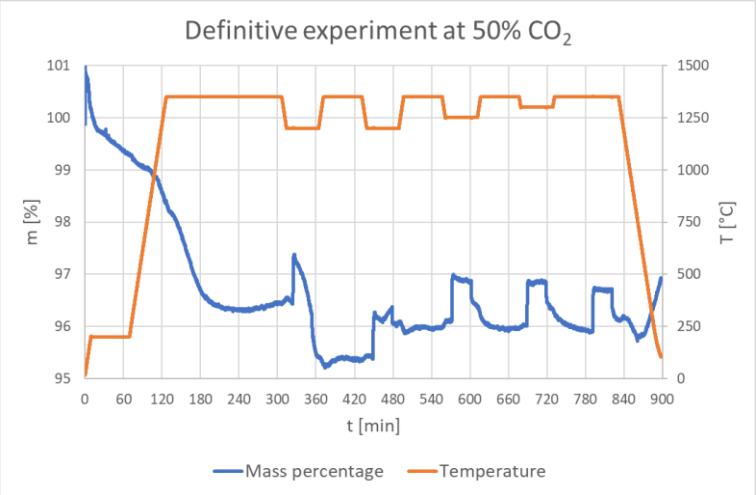
Definitive experiment at 50% CO2
101
100
99
98
97
96
95
m [%]
1500
1250
1000
750
500
250
0
T [°C]
0 60 120 180 240 300 360 420 480 540 600 660 720 780 840 900
t [min]
Mass percentage
Temperature

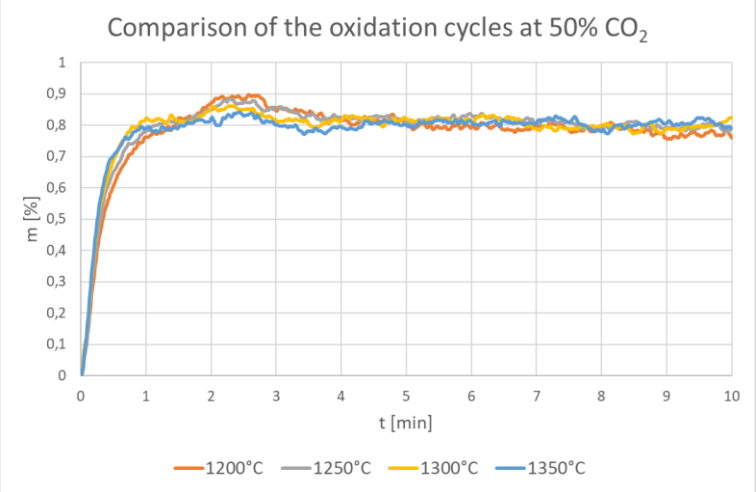
Comparison of the oxidation cycles at 50% CO2
1
0,9
0,8
0,7
0,6
0,5
0,4
0,3
0,2
0,1
0
m [%]
0 1 2 3 4 5 6 7 8 9 10
t [min]
1200°C
1250°C
1300°C
1350°C

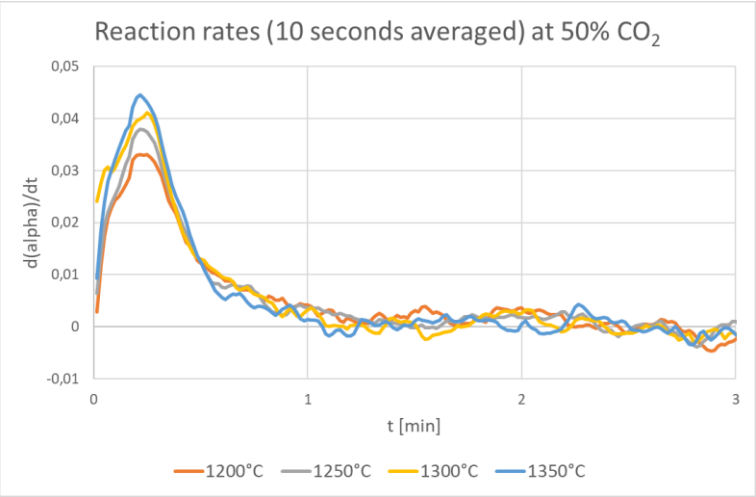
Reaction rates (10 seconds averaged) at 50% CO_2
d(alpha)/dt
0,05
0,04
0,03
0,02
0,01
0
-0,01
0
1
2
3
t [min]
1200°C
1250°C
1300°C
1350°C

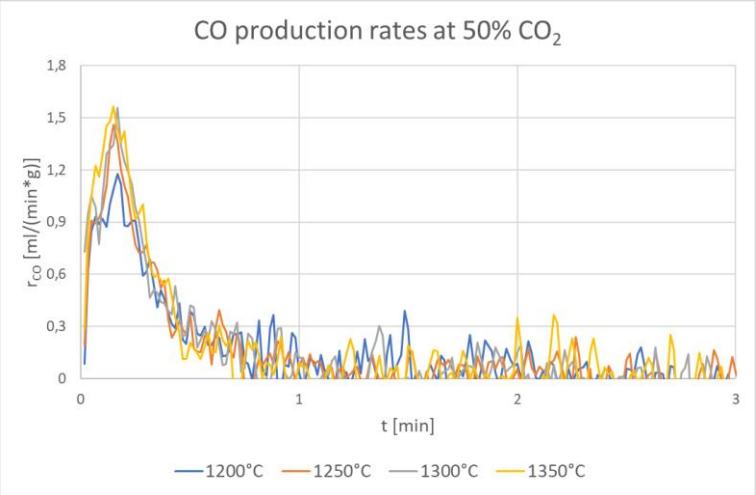
CO production rates at 50% CO_2
r_{CO} [ml/(min*g)]
1,8
1,5
1,2
0,9
0,6
0,3
0
0
1
2
3
t [min]
1200°C
1250°C
1300°C
1350°C

Appendix C

The graphs that were obtained for each cycle by following the model fitting procedure are displayed here for comparison purposes. It must be pointed out that the oscillatory nature of the dataset makes it possible for the involved cycles to have very different time durations one to the other, depending on the time instant in which the various samples reach its higher mass. It is clearly visible how, considering the plots of α as function of time, the first portion of the numerical curves are much closer to the experimental data. On the contrary, for the plots on the right, the fit is better in the second portion of the curves, but this effect is just a consequence of the multitude of points that are clustered in the bottom right of each diagram, not of a particularly accurate fitting when α approaches 1.

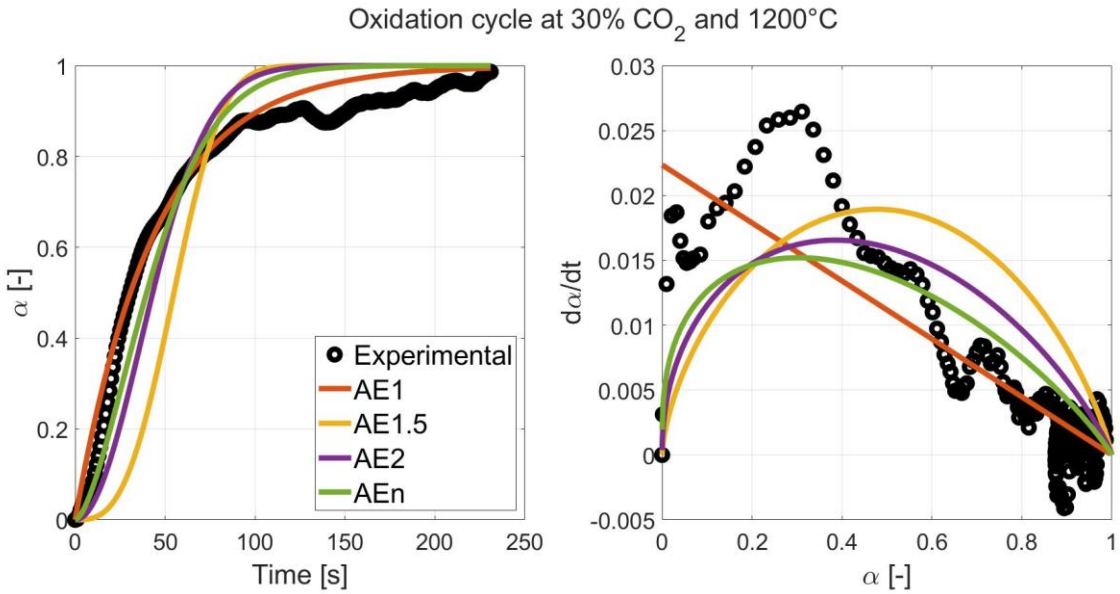

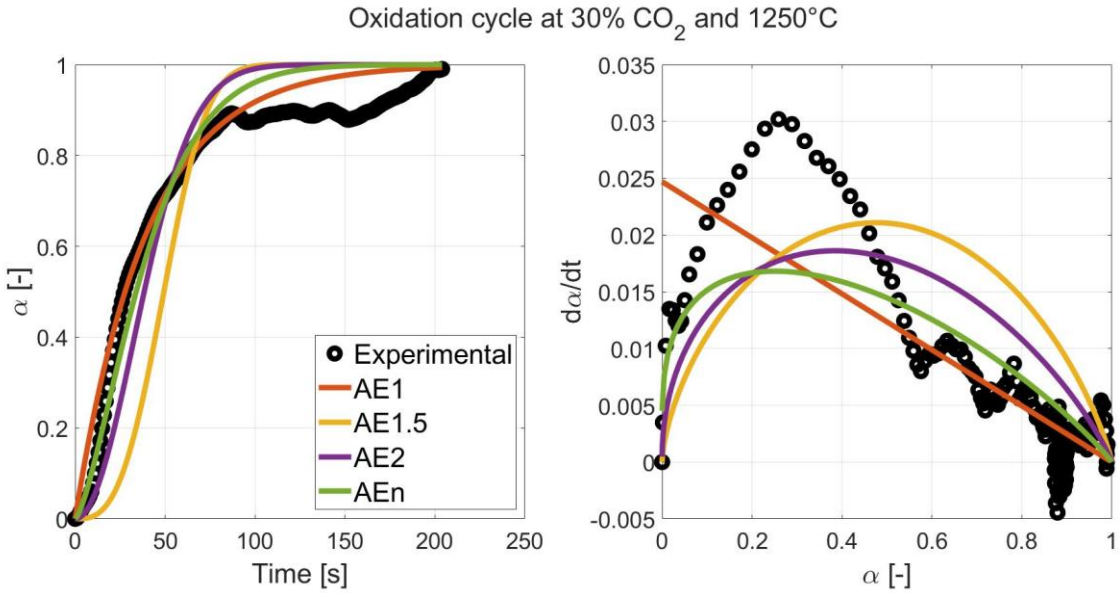

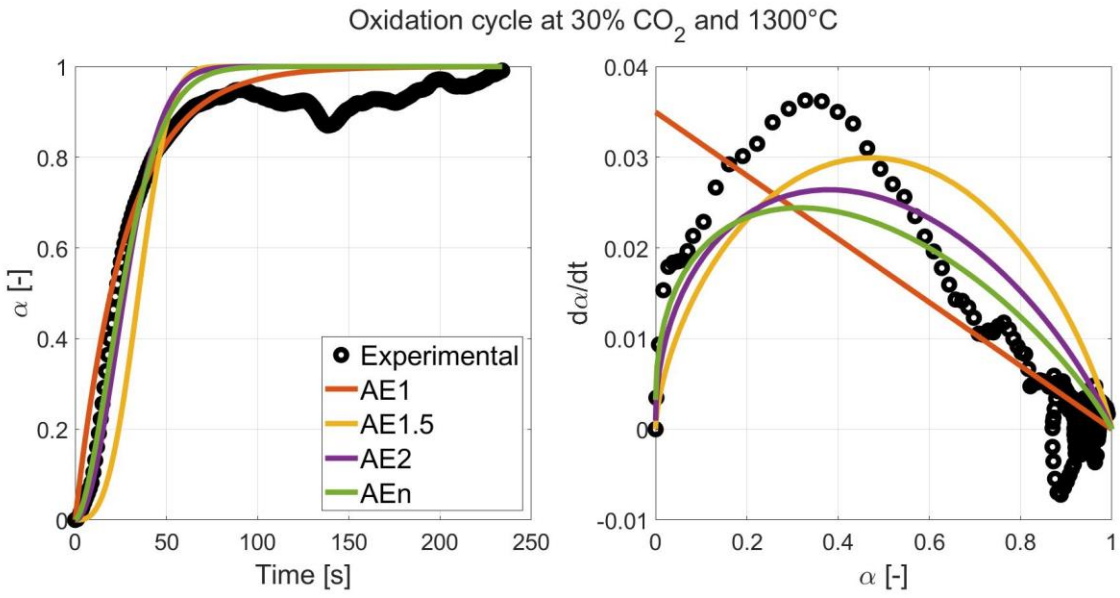
Oxidation cycle at 30% CO_2 and 1300°C
α [-]
Time [s]
Experimental
AE1
AE1.5
AE2
AEn
dα/dt
α [-]

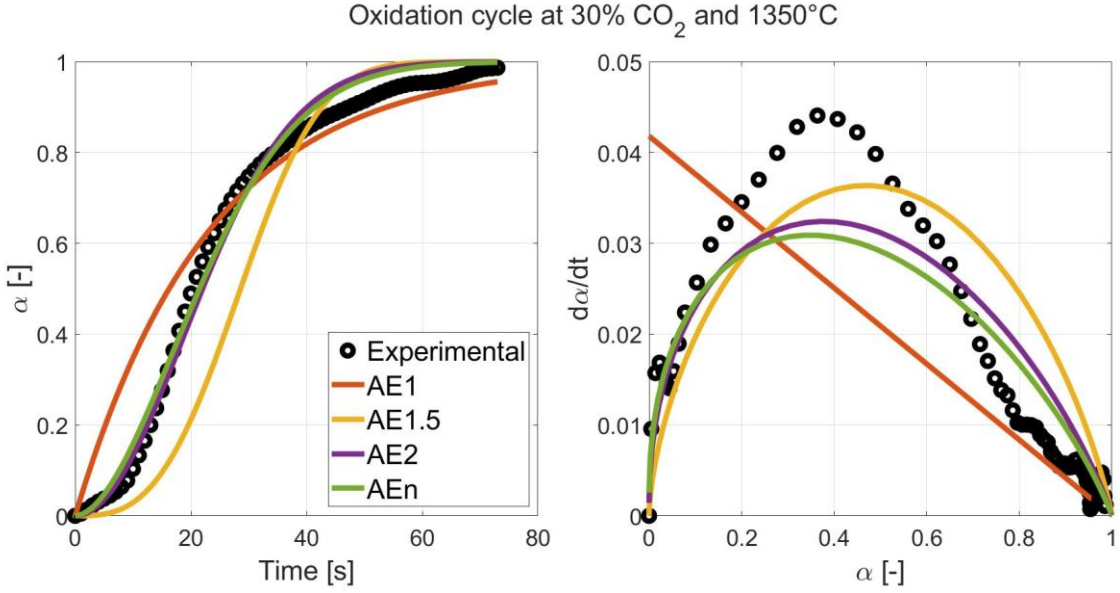
Oxidation cycle at 30% CO_2 and 1350°C
α [-]
Time [s]
Experimental
AE1
AE1.5
AE2
AEn
dα/dt
α [-]

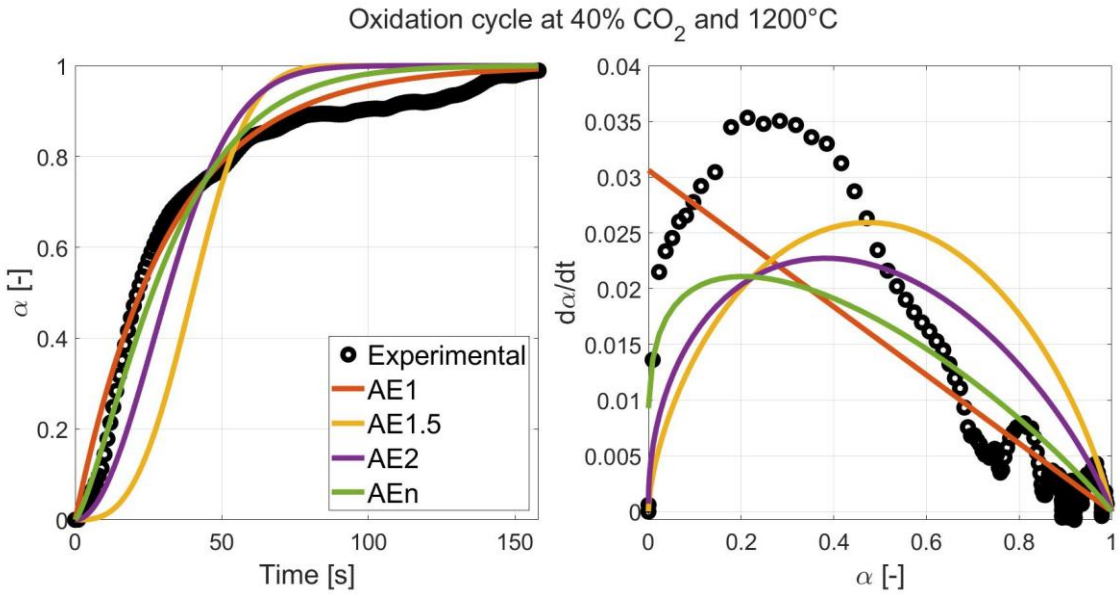
Oxidation cycle at 40% CO_2 and 1200°C
α [-]
Time [s]
Experimental
AE1
AE1.5
AE2
AEn
dα/dt
α [-]

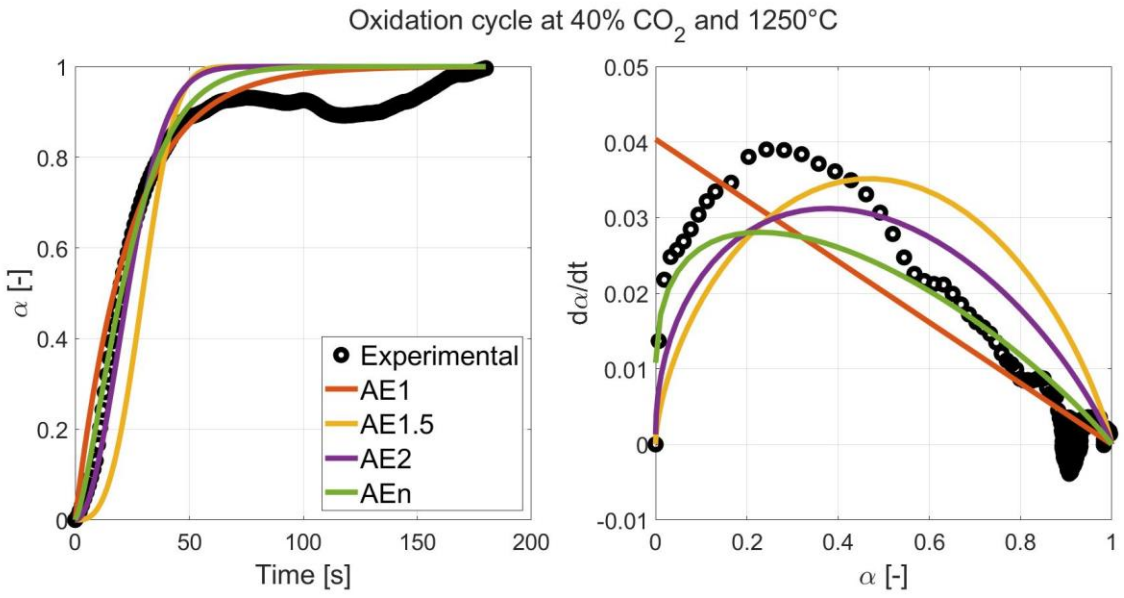
Oxidation cycle at 40% CO_2 and 1250°C
α [-]
Time [s]
dα/dt
α [-]
Experimental
AE1
AE1.5
AE2
AEn

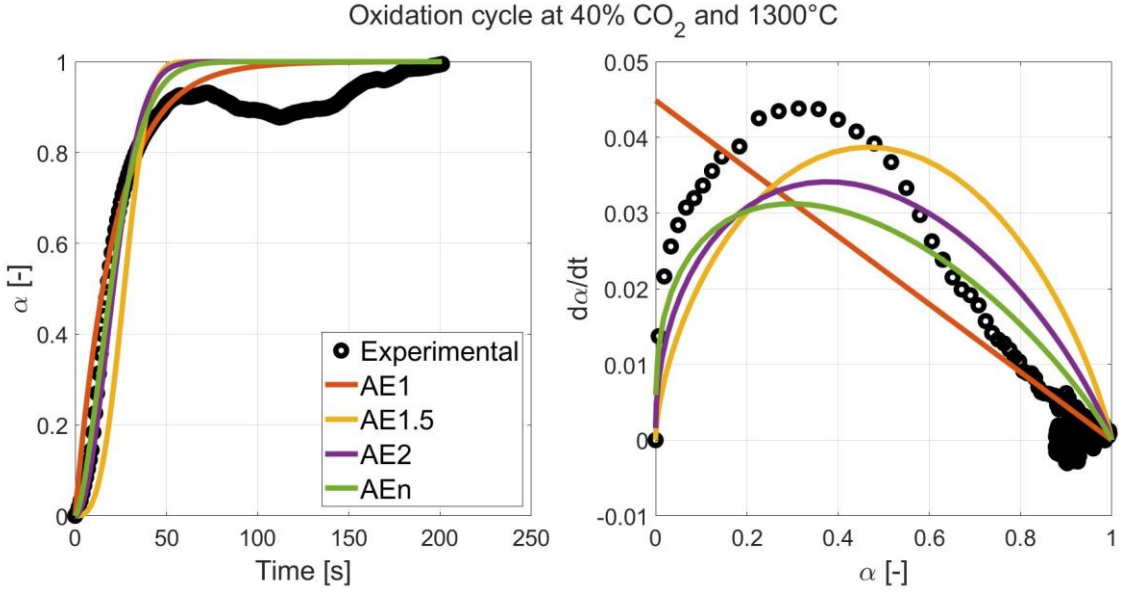
Oxidation cycle at 40% CO_2 and 1300°C
α [-]
Time [s]
dα/dt
α [-]
Experimental
AE1
AE1.5
AE2
AEn

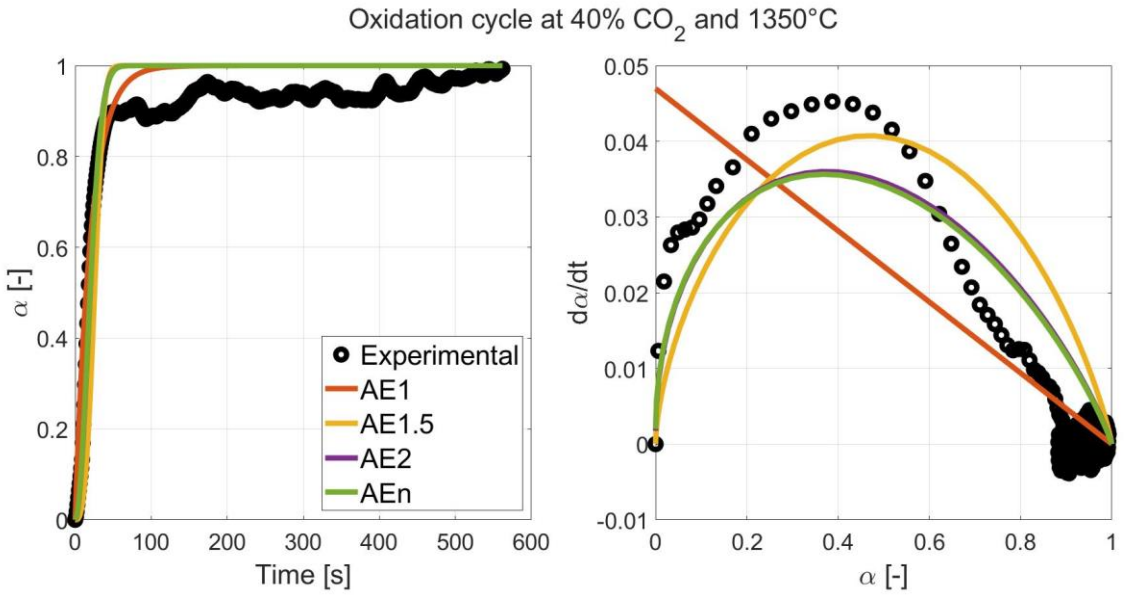
Oxidation cycle at 40% CO_2 and 1350°C
α [-]
Time [s]
dα/dt
α [-]
Experimental
AE1
AE1.5
AE2
AEn

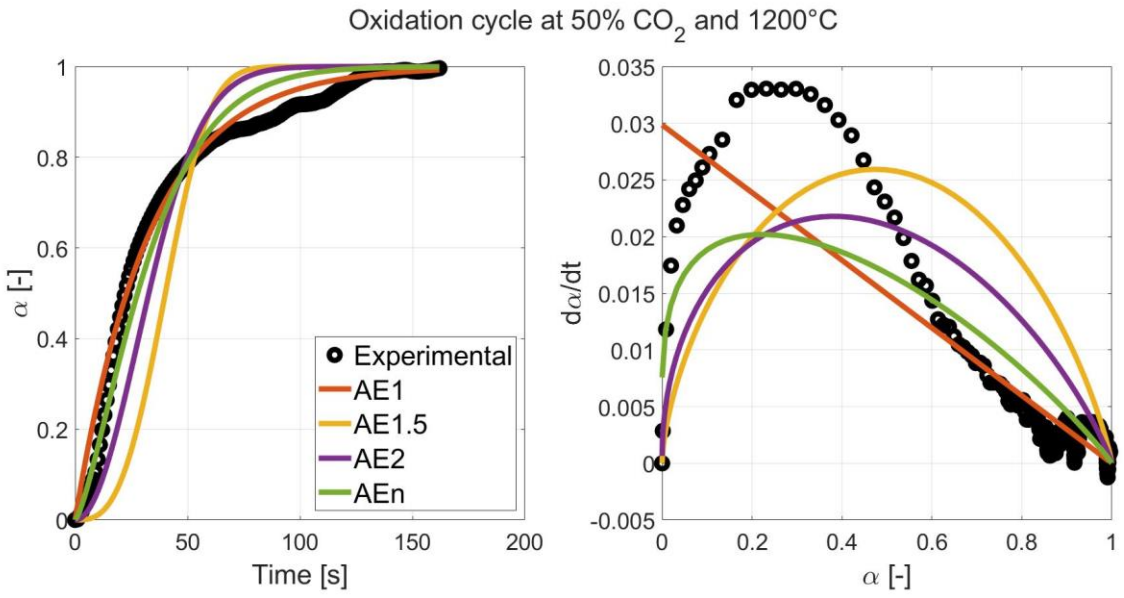
Oxidation cycle at 50% CO_2 and 1200°C
α [-]
Time [s]
Experimental
AE1
AE1.5
AE2
AEn
dα/dt
α [-]

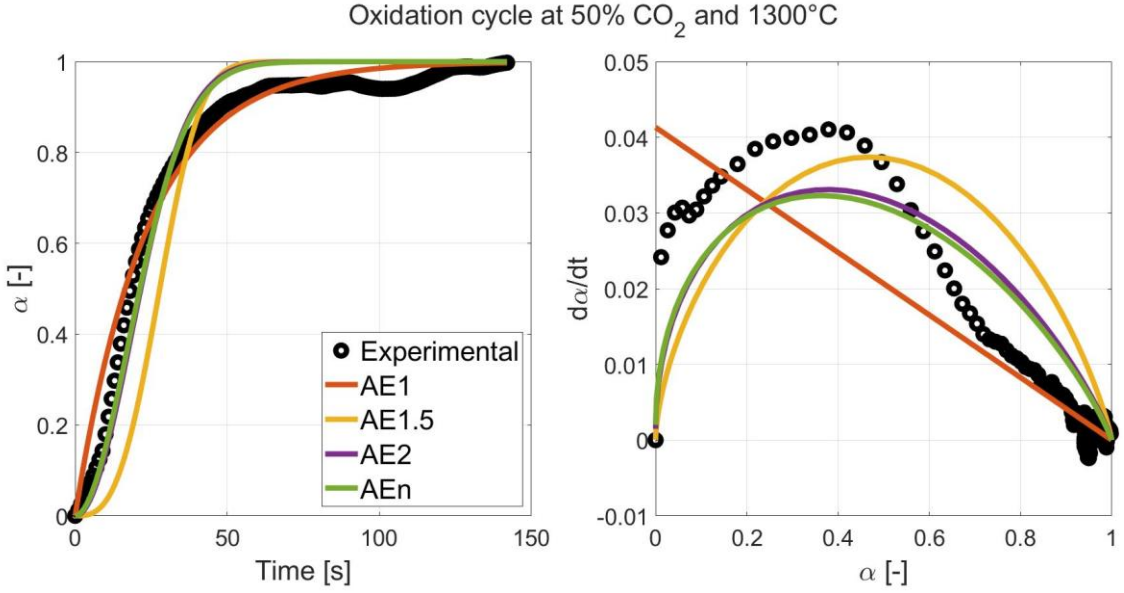
Oxidation cycle at 50% CO_2 and 1300°C
α [-]
Time [s]
Experimental
AE1
AE1.5
AE2
AEn
dα/dt
α [-]

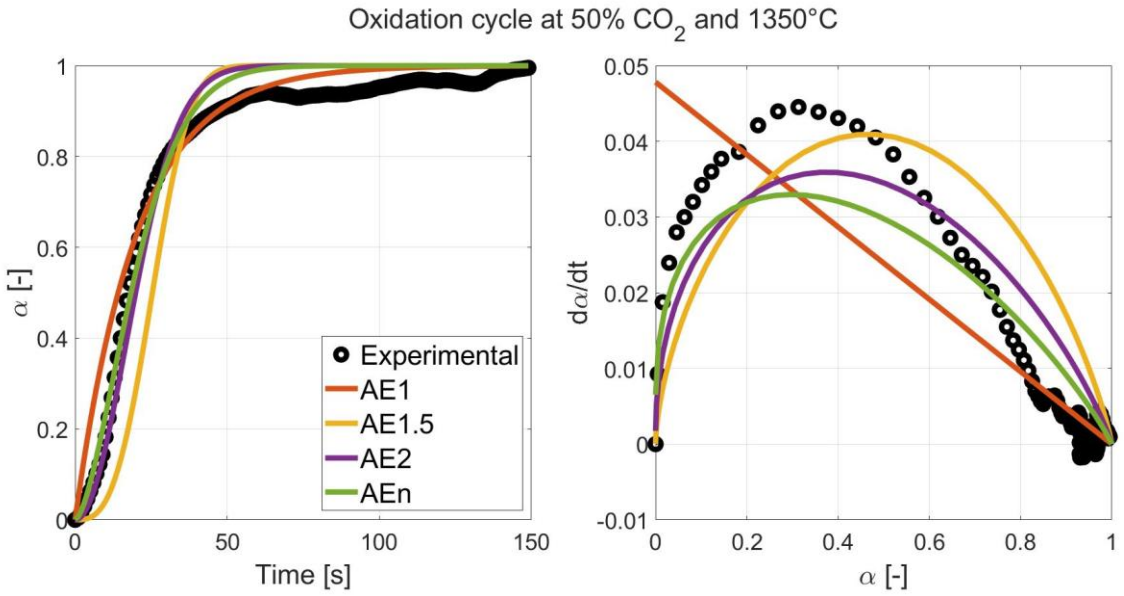
Oxidation cycle at 50% CO_2 and 1350°C
α [-]
Time [s]
Experimental
AE1
AE1.5
AE2
AEn
dα/dt
α [-]

References

[1] Petit, J. R., et al. «Climate and Atmospheric History of the Past 420,000 Years from the Vostok Ice Core, Antarctica». Nature, vol. 399, fasc. 6735, 1999, pp. 429–36. https://doi.org/10.1038/20859.

[2] "Climate Change: Atmospheric Carbon Dioxide | NOAA Climate.gov." Accessed March 3, 2023. http://www.climate.gov/news-features/understanding-climate/climate-change-atmospheric-carbon-dioxide.

[3] "IPCC Sixth Assessment Report – Working Group 1: The Physical Sciences Basis" Accessed March 3, 2023. https://www.ipcc.ch/report/ar6/wg1/chapter/technical-summary/.

[4] Bui, Mai, et al. «Carbon Capture and Storage (CCS): The Way Forward». Energy & Environmental Science, vol. 11, fasc. 5, 2018, pp. 1062–176. https://doi.org/10.1039/C7EE02342A.

[5] "Consolidated text: Directive 2003/87/EC of the European Parliament and of the Council of 13 October 2003 establishing a system for greenhouse gas emission allowance trading within the Union and amending Council Directive 96/61/EC" Accessed March 3, 2023. https://eur-lex.europa.eu/legal-content/EN/TXT/?uri=CELEX%3A02003L0087-20230121.

[6] "Delivering the European Green Deal" Accessed March 3, 2023. https://commission.europa.eu/strategy-and-policy/priorities-2019-2024/european-green-deal/delivering-european-green-deal_en.

[7] Prasad, S., et al. «Biofuels Production: A Sustainable Solution to Combat Climate Change». The Indian Journal of Agricultural Sciences, vol. 84, fasc. 12, 2014, pp. 3–12. https://epubs.icar.org.in/index.php/IJAgS/article/view/45210.

[8] Ausfelder, Florian, e Kurt Wagemann. «Power-to-Fuels: E-Fuels as an Important Option for a Climate-Friendly Mobility of the Future». Chemie Ingenieur Technik, vol. 92, fasc. 1–2, 2020, pp. 21–30. https://doi.org/10.1002/cite.201900180.

[9] Christoforidis, Konstantinos C., e Paolo Fornasiero. «Photocatalytic Hydrogen Production: A Rift into the Future Energy Supply». ChemCatChem, vol. 9, fasc. 9, 2017, pp. 1523–44. https://doi.org/10.1002/cctc.201601659.

[10] Nair, Mahesh M., e Stéphane Abanades. «Tailoring Hybrid Nonstoichiometric Ceria Redox Cycle for Combined Solar Methane Reforming and Thermochemical Conversion of H 2 O/CO 2». Energy & Fuels, vol. 30, fasc. 7, 2016, pp. 6050–58. https://doi.org/10.1021/acs.energyfuels.6b01063.

[11] Carrillo, Richard J., e Jonathan R. Scheffe. «Advances and Trends in Redox Materials for Solar Thermochemical Fuel Production». Solar Energy, vol. 156, 2017, pp. 3–20. https://doi.org/10.1016/j.solener.2017.05.032.

[12] Bahzad, Husain, et al. «Iron-Based Chemical-Looping Technology for Decarbonising Iron and Steel Production». International Journal of Greenhouse Gas Control, vol. 91, 2019, p. 102766. https://doi.org/10.1016/j.ijggc.2019.06.017.

[13] Funk, J. E., e R. M. Reinstrom. «Energy Requirements in Production of Hydrogen from Water». Industrial & Engineering Chemistry Process Design and Development, vol. 5, fasc. 3, 1966, pp. 336–42. https://doi.org/10.1021/i260019a025.

[14] Li, Sha, et al. «Thermodynamic Guiding Principles for Designing Nonstoichiometric Redox Materials for Solar Thermochemical Fuel Production: Ceria, Perovskites, and Beyond». Energy Technology, vol. 10, fasc. 1, 2022, p. 2000925. https://doi.org/10.1002/ente.202000925.

[15] Haeussler, Anita, et al. «Non-Stoichiometric Redox Active Perovskite Materials for Solar Thermochemical Fuel Production: A Review». Catalysts, vol. 8, fasc. 12, 2018, p. 611. https://doi.org/10.3390/catal8120611.

[16] Qian, Xin, et al. «Outstanding Properties and Performance of CaTi0.5Mn0.5O3–δ for Solar-Driven Thermochemical Hydrogen Production». Matter, vol. 4, fasc. 2, 2021, pp. 688–708. https://doi.org/10.1016/j.matt.2020.11.016.

[17] Abanades, Stéphane. «Redox Cycles, Active Materials, and Reactors Applied to Water and Carbon Dioxide Splitting for Solar Thermochemical Fuel Production: A Review». Energies, vol. 15, fasc. 19, 2022, p. 7061. https://doi.org/10.3390/en15197061.

[18] Miller, J. E., et al. «Advancing Oxide Materials for Thermochemical Production of Solar Fuels». Energy Procedia, vol. 49, 2014, pp. 2019–26. https://doi.org/10.1016/j.egypro.2014.03.214.

[19] Marxer, Daniel, et al. «Solar Thermochemical Splitting of CO 2 into Separate Streams of CO and O 2 with High Selectivity, Stability, Conversion, and Efficiency». Energy & Environmental Science, vol. 10, fasc. 5, 2017, pp. 1142–49. https://doi.org/10.1039/C6EE03776C.

[20] Mohd Fadzil, Nor Aqilah, et al. «Brief review of ceria and modified ceria: synthesis and application». Materials Research Express, vol. 5, fasc. 8, 2018, p. 085019. https://doi.org/10.1088/2053-1591/aad2b5.

[21] Schwarz, Karlheinz. «Materials Design of Solid Electrolytes». Proceedings of the National Academy of Sciences, vol. 103, fasc. 10, 2006, pp. 3497–3497. https://doi.org/10.1073/pnas.0600327103.

[22] Takacs, M., et al. «Oxygen Nonstoichiometry and Thermodynamic Characterization of Zr Doped Ceria in the 1573–1773 K Temperature Range». Physical Chemistry Chemical Physics, vol. 17, fasc. 12, 2015, pp. 7813–22. https://doi.org/10.1039/C4CP04916K.

[23] Scheffe, Jonathan R., e Aldo Steinfeld. «Thermodynamic Analysis of Cerium-Based Oxides for Solar Thermochemical Fuel Production». Energy & Fuels, vol. 26, fasc. 3, 2012, pp. 1928–36. https://doi.org/10.1021/ef201875v.

[24] Haeussler, Anita, et al. «Investigation of Reactive Perovskite Materials for Solar Fuel Production via Two-Step Redox Cycles: Thermochemical Activity, Thermodynamic Properties and Reduction Kinetics». Materials Chemistry and Physics, vol. 276, 2022, p. 125358. https://doi.org/10.1016/j.matchemphys.2021.125358.

[25] Abanades, Stéphane, e Gilles Flamant. «Thermochemical Hydrogen Production from a Two-Step Solar-Driven Water-Splitting Cycle Based on Cerium Oxides». Solar Energy, vol. 80, fasc. 12, 2006, pp. 1611–23. https://doi.org/10.1016/j.solener.2005.12.005.

[26] Emery, Antoine A., et al. «High-Throughput Computational Screening of Perovskites for Thermochemical Water Splitting Applications». Chemistry of Materials, vol. 28, fasc. 16, 2016, pp. 5621–34. https://doi.org/10.1021/acs.chemmater.6b01182.

[27] Nair, Mahesh M., e Stéphane Abanades. «Experimental Screening of Perovskite Oxides as Efficient Redox Materials for Solar Thermochemical CO 2 Conversion». Sustainable Energy & Fuels, vol. 2, fasc. 4, 2018, pp. 843–54. https://doi.org/10.1039/C7SE00516D.

[28] Zuev, A. Yu., e D. S. Tsvetkov. «Oxygen Nonstoichiometry, Defect Structure and Defect-Induced Expansion of Undoped Perovskite LaMnO3±δ». Solid State Ionics, vol. 181, fasc. 11–12, 2010, pp. 557–63. https://doi.org/10.1016/j.ssi.2010.02.024.

[29] Kim, YeonJu, et al. «Study of the Surface Reaction Kinetics of (La,Sr)MnO 3−δ Oxygen Carriers for Solar Thermochemical Fuel Production». Journal of Materials Chemistry A, vol. 6, fasc. 27, 2018, pp. 13082–89. https://doi.org/10.1039/C8TA01939H.

[30] Şanlı, Seyfettin Berk, e Berke Pişkin. «Effect of B-Site Al Substitution on Hydrogen Production of La0.4Sr0.6Mn1-XAlx (X=0.4, 0.5 and 0.6) Perovskite Oxides». International Journal of Hydrogen Energy, vol. 47, fasc. 45, 2022, pp. 19411–21. https://doi.org/10.1016/j.ijhydene.2021.12.047.

[31] Dey, Sunita, et al. «Beneficial Effects of Substituting Trivalent Ions in the B-Site of La 0.5 Sr 0.5 Mn 1−x A x O 3 (A = Al, Ga, Sc) on the Thermochemical Generation of CO and H 2 from CO 2 and H 2 O». Dalton Transactions, vol. 45, fasc. 6, 2016, pp. 2430–35. https://doi.org/10.1039/C5DT04822B.

[32] Islam, Md Tasbirul, et al. «A Comprehensive Review of State-of-the-Art Concentrating Solar Power (CSP) Technologies: Current Status and Research Trends». Renewable and Sustainable Energy Reviews, vol. 91, 2018, pp. 987–1018. https://doi.org/10.1016/j.rser.2018.04.097.

[33] Siegel, Nathan P., et al. «Factors Affecting the Efficiency of Solar Driven Metal Oxide Thermochemical Cycles». Industrial & Engineering Chemistry Research, vol. 52, fasc. 9, 2013, pp. 3276–86. https://doi.org/10.1021/ie400193q.

[34] Carrillo, Richard J., e Jonathan R. Scheffe. «Beyond Ceria: Theoretical Investigation of Isothermal and Near-Isothermal Redox Cycling of Perovskites for Solar Thermochemical Fuel Production». Energy & Fuels, vol. 33, fasc. 12, 2019, pp. 12871–84. https://doi.org/10.1021/acs.energyfuels.9b02714.

[35] Yuan, Cansheng, et al. «A New Solar Fuels Reactor Concept Based on a Liquid Metal Heat Transfer Fluid: Reactor Design and Efficiency Estimation». Solar Energy, vol. 122, 2015, pp. 547–61. https://doi.org/10.1016/j.solener.2015.08.019.

[36] Haeussler, Anita, et al. «Solar Thermochemical Fuel Production from H2O and CO2 Splitting via Two-Step Redox Cycling of Reticulated Porous Ceria Structures Integrated in a Monolithic Cavity-Type Reactor». Energy, vol. 201, 2020, p. 117649. https://doi.org/10.1016/j.energy.2020.117649.

[37] Furler, Philipp, et al. «Thermochemical CO 2 Splitting via Redox Cycling of Ceria Reticulated Foam Structures with Dual-Scale Porosities». Phys. Chem. Chem. Phys., vol. 16, fasc. 22, 2014, pp. 10503–11. https://doi.org/10.1039/C4CP01172D.

[38] Gokon, N., et al. «Thermochemical Two-Step Water-Splitting Reactor with Internally Circulating Fluidized Bed for Thermal Reduction of Ferrite Particles». International Journal of Hydrogen Energy, vol. 33, fasc. 9, 2008, pp. 2189–99. https://doi.org/10.1016/j.ijhydene.2008.02.044.

[39] Ermanoski, Ivan, et al. «A New Reactor Concept for Efficient Solar-Thermochemical Fuel Production». Journal of Solar Energy Engineering, vol. 135, fasc. 3, 2013, p. 031002. https://doi.org/10.1115/1.4023356.

[40] Koepf, Erik, et al. «A Novel Beam-down, Gravity-Fed, Solar Thermochemical Receiver/Reactor for Direct Solid Particle Decomposition: Design, Modeling, and Experimentation». International Journal of Hydrogen Energy, vol. 37, fasc. 22, 2012, pp. 16871–87. https://doi.org/10.1016/j.ijhydene.2012.08.086.

[41] Kaneko, Hiroshi, et al. «Rotary-Type Solar Reactor for Solar Hydrogen Production with Two-Step Water Splitting Process». Energy & Fuels, vol. 21, fasc. 4, 2007, pp. 2287–93. https://doi.org/10.1021/ef060581z.

[42] Bhatta, S., et al. «Solar Photo-Thermochemical Reactor Design for Carbon Dioxide Processing». Solar Energy, vol. 142, 2017, pp. 253–66. https://doi.org/10.1016/j.solener.2016.12.031.

[43] Roeb, M., et al. «Test Operation of a 100kW Pilot Plant for Solar Hydrogen Production from Water on a Solar Tower». Solar Energy, vol. 85, fasc. 4, 2011, pp. 634–44. https://doi.org/10.1016/j.solener.2010.04.014.

[44] Marxer, Daniel, et al. «Demonstration of the Entire Production Chain to Renewable Kerosene via Solar Thermochemical Splitting of H 2 O and CO 2». Energy & Fuels, vol. 29, fasc. 5, 2015, pp. 3241–50. https://doi.org/10.1021/acs.energyfuels.5b00351.

[45] "STA 2500 Regulus – A Highly Reliable and Fully Equipped Cost-Saving Instrument Package" Accessed March 3, 2023. https://analyzing-testing.netzsch.com/en/products/simultaneous-thermogravimetry-differential-scanning-calorimetry-sta-tg-dsc/sta-2500-regulus.

[46] Dhahri, Ah., et al. «Structural Characterization, Magnetic Properties and Magnetocaloric Effects of La0.75Sr0.25Mn1–x Cr x O3 (x = 0.15, 0.20, and 0.25)». Applied Physics A, vol. 116, fasc. 4, 2014, pp. 2077–85. https://doi.org/10.1007/s00339-014-8404-5.

[47] Sawaguri, Hiroki, et al. «Two-Step Thermochemical CO2 Splitting Using Partially-Substituted Perovskite Oxides of La0.7Sr0.3Mn0.9X0.1O3 for Solar Fuel Production». Frontiers in Energy Research, vol. 10, 2022, p. 872959. https://doi.org/10.3389/fenrg.2022.872959.

[48] Tao, et al. «Methane Oxidation at Redox Stable Fuel Cell Electrode La 0.75 Sr 0.25 Cr 0.5 Mn 0.5 O 3- δ». The Journal of Physical Chemistry B, vol. 110, fasc. 43, 2006, pp. 21771–76. https://doi.org/10.1021/jp062376q.

[49] Bayon, Alicia, et al. «Experimental, Computational and Thermodynamic Studies in Perovskites Metal Oxides for Thermochemical Fuel Production: A Review». International Journal of Hydrogen Energy, vol. 45, fasc. 23, 2020, pp. 12653–79. https://doi.org/10.1016/j.ijhydene.2020.02.126.

[50] Bork, Alexander H., et al. «Thermodynamic Assessment of the Solar-to-Fuel Performance of La 0.6Sr 0.4Mn 1-YCr yO 3-σ Perovskite Solid Solution Series». SSRN Electronic Journal, 2018. https://doi.org/10.2139/ssrn.3302669.

[51] Carrillo, Alfonso J., et al. «Modifying La 0.6 Sr 0.4 MnO 3 Perovskites with Cr Incorporation for Fast Isothermal CO 2 -Splitting Kinetics in Solar-Driven Thermochemical Cycles». Advanced Energy Materials, vol. 9, fasc. 28, 2019, p. 1803886. https://doi.org/10.1002/aenm.201803886.

[52] Gokon, Nobuyuki, et al. «Thermochemical Two-Step Water Splitting Cycle Using Perovskite Oxides Based on LaSrMnO3 Redox System for Solar H2 Production». Thermochimica Acta, vol. 680, 2019, p. 178374. https://doi.org/10.1016/j.tca.2019.178374.

[53] V'Yunov, O. I., et al. «Structural Peculiarities and Properties of (La,Sr)(Mn,Me)O3 (Me=Cu,Cr)». Nigel Sammes et al. in: Fuel Cell Technologies: State and Perspectives, vol. 202, Springer-Verlag, 2005, pp. 323–28. https://doi.org/10.1007/1-4020-3498-9_37.

[54] Sirvent, Juan De Dios, et al. «Nanostructured La 0.75 Sr 0.25 Cr 0.5 Mn 0.5 O 3 –Ce 0.8 Sm 0.2 O 2 Heterointerfaces as All-Ceramic Functional Layers for Solid Oxide Fuel Cell Applications». ACS Applied Materials & Interfaces, vol. 14, fasc. 37, 2022, pp. 42178–87. https://doi.org/10.1021/acsami.2c14044.

[55] Yanchevskii, O. Z., et al. «Structural, Electrical, and Magnetic Properties of La0.7Sr0.3Mn1−y CryO3». Inorganic Materials, vol. 42, fasc. 10, 2006, pp. 1121–25. https://doi.org/10.1134/S002016850610013X.

[56] Yang, Chih-Kai, et al. «Thermodynamic and Kinetic Assessments of Strontium-Doped Lanthanum Manganite Perovskites for Two-Step Thermochemical Water Splitting». J. Mater. Chem. A, vol. 2, fasc. 33, 2014, pp. 13612–23. https://doi.org/10.1039/C4TA02694B.

[57] Scheffe, Jonathan R., et al. «Lanthanum–Strontium–Manganese Perovskites as Redox Materials for Solar Thermochemical Splitting of H 2 O and CO 2». Energy & Fuels, vol. 27, fasc. 8, 2013, pp. 4250–57. https://doi.org/10.1021/ef301923h.

[58] Sastre, Daniel, et al. «Exploring the Redox Behavior of La0.6Sr0.4Mn1−xAlxO3 Perovskites for CO2-Splitting in Thermochemical Cycles». Topics in Catalysis, vol. 60, fasc. 15–16, 2017, pp. 1108–18. https://doi.org/10.1007/s11244-017-0790-4.

[59] Demont, Antoine, e Stéphane Abanades. «Solar Thermochemical Conversion of CO 2 into Fuel via Two-Step Redox Cycling of Non-Stoichiometric Mn-Containing Perovskite Oxides». Journal of Materials Chemistry A, vol. 3, fasc. 7, 2015, pp. 3536–46. https://doi.org/10.1039/C4TA06655C.

[60] Bork, A. H., et al. «Perovskite La 0.6 Sr 0.4 Cr 1−x Co x O 3−δ Solid Solutions for Solar-Thermochemical Fuel Production: Strategies to Lower the Operation Temperature». Journal of Materials Chemistry A, vol. 3, fasc. 30, 2015, pp. 15546–57. https://doi.org/10.1039/C5TA02519B.

[61] Ezbiri, M., et al. «High Redox Capacity of Al-Doped La 1− x Sr x MnO 3− δ Perovskites for Splitting CO 2 and H 2 O at Mn-Enriched Surfaces». ChemSusChem, vol. 10, fasc. 7, 2017, pp. 1517–25. https://doi.org/10.1002/cssc.201601869.

[62] Cooper, Thomas, et al. «Lanthanum Manganite Perovskites with Ca/Sr A-Site and Al B-Site Doping as Effective Oxygen Exchange Materials for Solar Thermochemical Fuel Production». Energy Technology, vol. 3, fasc. 11, 2015, pp. 1130–42. https://doi.org/10.1002/ente.201500226.

[63] Gálvez, M. E., et al. «Physico-Chemical Changes in Ca, Sr and Al-Doped La–Mn–O Perovskites upon Thermochemical Splitting of CO 2 via Redox Cycling». Physical Chemistry Chemical Physics, vol. 17, fasc. 9, 2015, pp. 6629–34. https://doi.org/10.1039/C4CP05898D.

[64] Vyazovkin, Sergey, et al. «ICTAC Kinetics Committee Recommendations for Collecting Experimental Thermal Analysis Data for Kinetic Computations». Thermochimica Acta, vol. 590, 2014, pp. 1–23. https://doi.org/10.1016/j.tca.2014.05.036.

[65] Koga, Nobuyoshi, e Haruhiko Tanaka. «Effect of Sample Mass on the Kinetics of Thermal Decomposition of a Solid». Thermochimica Acta, vol. 209, 1992, pp. 127–34. https://doi.org/10.1016/0040-6031(92)80190-8.

[66] Vyazovkin, Sergey, et al. «ICTAC Kinetics Committee Recommendations for Performing Kinetic Computations on Thermal Analysis Data». Thermochimica Acta, vol. 520, fasc. 1–2, 2011, pp. 1–19. https://doi.org/10.1016/j.tca.2011.03.034.

[67] Khawam, Ammar, e Douglas R. Flanagan. «Solid-State Kinetic Models: Basics and Mathematical Fundamentals». The Journal of Physical Chemistry B, vol. 110, fasc. 35, 2006, pp. 17315–28. https://doi.org/10.1021/jp062746a.

[68] Kubicek, Markus, et al. «Perovskite Oxides – a Review on a Versatile Material Class for Solar-to-Fuel Conversion Processes». Journal of Materials Chemistry A, vol. 5, fasc. 24, 2017, pp. 11983–2000. https://doi.org/10.1039/C7TA00987A.

[69] Bulfin, B., et al. «Isothermal Relaxation Kinetics for the Reduction and Oxidation of SrFeO 3 Based Perovskites». Physical Chemistry Chemical Physics, vol. 22, fasc. 4, 2020, pp. 2466–74. https://doi.org/10.1039/C9CP05771D.

[70] Vyazovkin, Sergey, et al. «ICTAC Kinetics Committee Recommendations for Analysis of Multi-Step Kinetics». Thermochimica Acta, vol. 689, 2020, p. 178597. https://doi.org/10.1016/j.tca.2020.178597.

[71] Muraleedharan Nair, Mahesh, e Stéphane Abanades. «Solid-State Reoxidation Kinetics of A/B-Site Substituted LaMnO 3 During Solar Thermochemical CO 2 Conversion». Energy Technology, vol. 9, fasc. 2, 2021, p. 2000885. https://doi.org/10.1002/ente.202000885.

[72] Farooqui, A. E., et al. «Assessment of Kinetic Model for Ceria Oxidation for Chemical-Looping CO2 Dissociation». Chemical Engineering Journal, vol. 346, 2018, pp. 171–81. https://doi.org/10.1016/j.cej.2018.04.041.